

**PROCESSING OF COMPOSITE CARBON MATERIALS AND SOLID  
ELECTROLYTES FOR SUPERCAPACITOR ENERGY STORAGE**



**DISSERTATION**

Submitted to the Graduate Faculty  
In Partial Fulfillment of the Requirement for the  
Degree of **Doctor of Philosophy** In the  
Department of Materials Science and Engineering  
African University of Science and Technology, Abuja-Nigeria

By:

**KINGSLEY IKECHUKWU ORISEKEH (ID No: 70134)**

February, 2022.

**PhD Dissertation Committee:**

Prof. **Winston. O. Soboyejo** (Worcester Polytechnic Institute, 100 Institute Road, Worcester, MA 01609, USA.)

Dr. **Abdulahakeem Bello** (African University of Science and Technology, Abuja)

Dr. Vitalis Anye (African University of Science and Technology, Abuja)

Dr. **O. K. Oyewole** (Worcester Polytechnic Institute, 100 Institute Road, Worcester, MA 01609, USA.)

Dr. Kenfack Anatole (African University of Science and Technology, Abuja)

**Processing of Composite Carbon Materials and Solid Electrolytes for Supercapacitor Energy Storage**

By:

Kingsley Ikechukwu Orisekeh

A THESIS APPROVED BY THE MATERIALS SCIENCE AND ENGINEERING DEPARTMENT

RECOMMENDED: .....

**Supervisor, Professor Winston. O. Soboyejo**

.....

**Co-supervisor, Dr. Abdulhakeem Bello**

.....

Head, Dept. of Materials Science and Engineering

Approved: .....

Vice President, Academics

Date: .....

© Copyright Kingsley Ikechukwu Orisekeh, 2022

All rights reserved

## DEDICATION

With deep sense of gratitude, this dissertation is dedicated to my family, my late parents Mr. and Mrs. Frank and Beatrice Orisekeh. Also, to my dearest wife and treasure, Mrs. Ifunanya Faith Orisekeh and my beloved son Jedidiah Chukwumuanya Orisekeh as well as my siblings, Flora, Ngozi, Bright, Tessy and David and my bosom friends Dr. Kelechi Ibegbulem and Dr. Ogechukwu Onugha

## ABSTRACT

These research works presents the results of a combined theoretical, experimental and statistical study of processing of composite carbon materials and solid electrolytes for supercapacitor energy storage. The need for flexible energy storage devices has stimulated the interest in the development of nanostructures in supercapacitors for energy storage. A hydrothermal method is used to optimize the growth of  $\alpha$ -Fe<sub>2</sub>O<sub>3</sub> nanoparticles on carbon cloth (CC) and activated carbon cloth (ACC). The resulting composition, morphologies and microstructures displayed interesting features that are suitable as electrodes material for electrochemical capacitors. These are integrated as binder-free, symmetric device, which were then assembled and tested. The device assembled with the activated carbon cloth exhibited higher electrochemical performance (specific capacity of 295.56 mAhg<sup>-1</sup>, specific energy of 37 WhKg<sup>-1</sup> and specific power of 0.5 kWKg<sup>-1</sup> in a 3 M KOH electrolyte at 1 A g<sup>-1</sup>). The device also had good capacitance retention of 96.6 % after 10000 charge-discharge cycles. The implications of the results are discussed for potential applications of the  $\alpha$ -Fe<sub>2</sub>O<sub>3</sub>-ACC in supercapacitors for energy storage systems that address global energy needs. Similarly, the conventional lithium ion batteries use liquid electrolytes that are chemically unstable due to the presence of carbonates, which are highly volatile and flammable, creating a significant safety risk. Therefore, the need for the development of solid state electrolytes (SSEs) that are safe, environmentally friendly, with robust mechanical properties. In this work, the solid polymer blend is explored using a mixture of a polymer matrix of polyvinyl pyrrolidone (PVP)/polyvinyl alcohol (PVA) and lithium perchlorate salt (LiClO<sub>4</sub>). The produced films are characterized using a Scanning Electron Microscopy (SEM), X-ray Diffraction (XRD) and Fourier Transform Infra-Red (FTIR). The mechanical properties of the flexible films are also measured using nanoindentation techniques, statistical deconvolution mapping, tensile tests and fracture toughness measurements. (Young's modulus of 6.87 GPa, Hardness of 1.3 GPa, Tensile strength of 4.3 MPa and Fracture toughness of 0.81 MPa.m<sup>0.5</sup>) The implications of the results are then discussed for potential applications of robust solid polymer blends-based electrolytes.

**Keywords:**  $\alpha$ -Fe<sub>2</sub>O<sub>3</sub> Nanoparticles; Activated Carbon Cloth; Binder Free Processing; Supercapacitors; Mechanical properties; Nanoindentation techniques; Statistical deconvolution; Fracture toughness measurements.

## PREFACE

This dissertation is an original intellectual property of Kingsley Ikechukwu Orisekeh based on the work done from the period of 2017 to February 2022 for the fulfilment of Doctor of Philosophy degree in the Department of Materials Science and Engineering at the African University of Science and Technology, Abuja-Nigeria.

I was the lead investigator in this work, responsible for all major activities: experiments, data collection and writing of the original manuscripts while Prof. Winston O. Soboyejo and Dr. Abdulhakeem Bello were the supervisory authors, who were also involved in the early stages of the concept formations and manuscripts compositions.

Processing of  $\alpha$ -Fe<sub>2</sub>O<sub>3</sub> nanoparticles on activated carbon cloth as binder-free electrode material for supercapacitor energy storage as well as study on the mechanical properties of polyvinyl pyrrolidone /polyvinyl alcohol-based solid electrolytes are presented in this thesis. The resulting composition, morphologies, microstructures and mechanical properties displayed interesting features that are suitable for application in energy storage devices.

As at the time this thesis was submitted, two of its chapters (3 and 4) have been published in peer-reviewed journals: Journal of Energy Storage and Journal of Applied Polymer Sciences.

## ACKNOWLEDGEMENTS

I would like to thank the Pan African Materials Institute (PAMI), a regional Center of Excellence in Materials Science and Engineering established under the World Bank (WB) African Centers of Excellence (ACEs) program, hosted at the African University of Science and Technology, Abuja, Nigeria for their financial support. Appreciation is also extended to the Worcester Polytechnic Institute (WPI), Worcester, Massachusetts, USA for their support.

I also thank Mr. Anthony Elechi of AfDB Laboratory, African University of Science and Technology, Abuja for his assistance with some of the laboratory work.

I want to extend my sincere appreciation to my PhD Dissertation Committee: Prof. Winston. O. Soboyejo, Dr. Abdulhakeem Bello, Dr. Vitalis Anye, Dr. O. K. Oyewole and Dr. A. Kenfack for their support and technical guidance.

This academic pursuit would have been impossible without the continuous prayers and emotional supports from my family especially my dearest wife whom I call “Treasure”, Mrs. Ifunanya Faith Orisekeh and my delightful son, Jedidiah Chukwumuanya Orisekeh and ofcourse my siblings and in-laws. I am truly grateful to my bosom friends, Dr. Kelechi Ibegbulem and Dr. Ogechukwu Onugha. Finally and most importantly, with bended knees, I say thanks to the almighty God the fountain of wisdom, knowledge, and understanding for making this dream come to pass.

## LIST OF PUBLICATIONS

- [1] **K. I. Orisekeh**, V. Anye, O. K. Oyewole, R. Ahmed, D. K. Orisekeh, O. V. Oyelade, S. A. Adeniji, S. Umar, A. Bello and W. O. Soboyejo Mechanical Properties of Polyvinyl Pyrrolidone /Polyvinyl Alcohol-Based Solid Electrolytes. *Journal of Applied Polymer Science* 2022
- [2] O. V. Oyelade, O. K. Oyewole, Y. A. Olanrewaju, R. Ichwani, R. Koech, D. O. Oyewole, S. A. Adeniji, D. M. Sanni, J. Cromwell, R. A. Ahmed, **K. I. Orisekeh**, V. C. Anye and W. O. Soboyejo “Understanding the effects of annealing temperature on the mechanical properties of layers in FAI-rich perovskite solar cells,” *AIP Adv.*, vol. 12, no. 2, p. 025104, 2022.
- [3] **K. Orisekeh**, B. Singh, Y. Olanrewaju, M. Kigozi, G. Ihekwe, S. Umar, V. Anye, A. Bello, S. Parida and W.O. Soboyejo “Processing of  $\alpha$ -Fe<sub>2</sub>O<sub>3</sub> Nanoparticles on Activated Carbon Cloth as Binder-Free Electrode Material for Supercapacitor Energy Storage,” *J. Energy Storage*, vol. 33, no. July, 2021.
- [4] R. A. Ahmed, N. Ebechidi, I. Reisy, **K. Orisekeh**, A. Huda, A. Bello, O. K. Oyewole and W. O. Soboyejo “Pressure-induced interfacial contacts and the deformation in all solid-state Li-ion batteries,” *J. Power Sources*, vol. 521, no. October 2021, 2022.
- [5] Y. A. Olanrewaju, **K. Orisekeh**, Omolara V. Oyelade, R. K. Koech, R. Ichwani, A. I. Egun, D. I. Amune, A. Bello, V. C. Anye, O. K. Oyewole and Winston O. Soboyejo “Effects of temperature-dependent burn-in decay on the performance of triple cation mixed halide perovskite solar cells,” *AIP Adv.*, vol. 12, no. 1, p. 015122, 2022.
- [6] S. Adeniji, O. Oyewole, R. Koech, D. Oyewole, J. Cromwell, R. Ahmed, O. Oyelade, D. Sanni, **K. Orisekeh**, A. Bello and W. Soboyejo “Failure Mechanisms of Stretchable Perovskite Light-Emitting Devices under Monotonic and Cyclic Deformations,” *Macromol. Mater. Eng.*, vol. 306, no. 11, pp. 1–9, 2021.
- [7] M. Kigozi, R. Koech, , **K. Orisekeh**, R. Kali, O. L M Kamoga, B. Padya, A. Bello, G. N Kasozi, P. K. Jain, J. B. Kirabira, A. P. Onwualu and N. Y Dzade “Cobs Porous Carbon-Based Materials With High Energy And Excellent Cycle Stability For Supercapacitor Applications,” *Prepr. Res. Sq.*, p. 27, 2021.
- [8] O. F. Ngasoh, V. C. Anye, E. B. Ojo, T. T. Stanislas, A. Bello, B. Agyei-Tuffour, **K. Orisekeh**, O. K. Oyewole, N. Rahbar and W. O. Soboyejo “Mechanical Properties of Epoxy/Clay Composite Coatings on an X65 Steel Substrate,” *Cogent Eng.*, vol. 8, no. 1, 2021.
- [9] G. O. Ihekwe, I. I. Obianyo, **K. I. Orisekeh**, G. M. Kalu-Uka, I. C. Nwuzor, and A. P. Onwualu, “Plasticity characterization of certain Nigeria clay minerals for their application in ceramic water filters,” *Sci. Prog.*, vol. 104, no. 2, pp. 1–13, 2021.

- [10] A. Bello, D.M. Sanni, S.A. Adeniji, V. Anye, **K. Orisekeh**, M. Kigozi and R. Koech “Combustion synthesis of battery-type positive electrodes for robust aqueous hybrid supercapacitor,” *J. Energy Storage*, vol. 27, no. October 2019, p. 101160, 2020.
- [11] M. Kigozi, R. K. Koech, **K. Orisekeh**, I. Ojeaga, E. Tebandeke, G. N Kasozi, A. P. Onwualu  
“Synthesis and characterization of graphene oxide from locally mined graphite flakes and its supercapacitor applications,” *Results Mater.*, vol. 7, no. June, p. 100113, 2020.
- [12] G. O. Ihekweme, J. N. Shondo, **K. I. Orisekeh**, G. M. Kalu-Uka, I. C. Nwuzor, and A. P. Onwualu, “Characterization of certain Nigerian clay minerals for water purification and other industrial applications,” *Heliyon*, vol. 6, no. 4, p. e03783, 2020.

## TABLE OF CONTENTS

### Contents

All rights reserved.....	iii
DEDICATION .....	iv
ABSTRACT.....	v
PREFACE.....	vi
ACKNOWLEDGEMENTS .....	vii
LIST OF PUBLICATIONS .....	viii
LIST OF FIGURES .....	xiv
LIST OF TABLES .....	xvii
LIST OF ABBREVIATIONS.....	xviii
<b>CHAPTER ONE .....</b>	<b>1</b>
<b>1.0 Introduction.....</b>	<b>1</b>
1.1 Background.....	1
1.2 Problem Statement.....	2
1.3 Research Objectives.....	3
1.4 Scope of the work .....	4
<b>REFERENCES.....</b>	<b>5</b>
<b>Chapter Two.....</b>	<b>8</b>
<b>2.0 LITERATURE REVIEW .....</b>	<b>8</b>
2.1 Energy storage systems.....	8
<b>2.1.1. Energy storage system components.....</b>	<b>9</b>
<b>2.2. Batteries Energy Storage Systems (BESS).....</b>	<b>9</b>
2.3. Energy Storage System-Supercapacitors (ESS-SCs).....	10
<b>2.3.1. Electric double-layer capacitors (EDLC).....</b>	<b>12</b>
<b>2.3.2. Pseudo-capacitors.....</b>	<b>14</b>
<b>2.3.3. Hybrid supercapacitors (HSC) .....</b>	<b>15</b>
<b>2.4. Carbon-based electrode materials.....</b>	<b>17</b>
2.4.1. Graphene/graphene oxide .....	18
2.4.2. Graphene-Metal oxide composite .....	20
2.5. Activated carbon (AC).....	28
2.5.1. Controlling of shape and size in mesoporous carbon.....	33

2.6. Synthesis approach for electrode materials.....	37
2.6.1. Sol-gel method .....	37
2.6.2. Electro-polymerization / Electrodeposition .....	38
2.6.3. In-situ polymerization.....	39
2.6.4. Direct coating.....	40
<b>2.6.5. Chemical vapour deposition (CVD) .....</b>	<b>40</b>
2.6.6. Vacuum filtration technique.....	41
2.6.7. Hydrothermal/solvothermal method .....	41
2.6.8. Co-precipitation method .....	42
2.6.9. Dealloying method.....	42
2.6.10. Other synthesis methods .....	43
2.7. Concept of supercapacitor technology .....	44
<b>2.7.1. Cell Construction .....</b>	<b>44</b>
2.7.2. Electrode .....	44
<b>2.7.3. Electrolyte.....</b>	<b>45</b>
2.7.4. Separator .....	46
2.8. Characteristics of supercapacitors.....	46
<b>2.8.1. Supercapacitor Capacitance .....</b>	<b>47</b>
<b>2.8.2. Supercapacitor Rated Voltage .....</b>	<b>48</b>
2.8.3. Supercapacitor Internal Resistance .....	49
<b>2.8.4. Temperature .....</b>	<b>50</b>
<b>2.8.5. Supercapacitor Energy and Power Densities .....</b>	<b>51</b>
<b>2.8.6. Charging/Discharging Supercapacitor.....</b>	<b>51</b>
2.9. Applications of supercapacitors .....	51
<b>2.9.1. Advantages and Limitations of Supercapacitors .....</b>	<b>53</b>
<b>2.9.2. The limitations are as follows: .....</b>	<b>54</b>
2.10 Mechanical Performance of Solid State Electrolytes .....	54
<b>2.10.1 Deformation of Solid State Electrolytes .....</b>	<b>56</b>
<b>References.....</b>	<b>60</b>
<b>CHAPTER THREE .....</b>	<b>66</b>
<b>3.0. Processing of <math>\alpha</math>-Fe<sub>2</sub>O<sub>3</sub> Nanoparticles on Activated Carbon Cloth as Binder-Free Electrode Material for Supercapacitor Energy Storage.....</b>	<b>66</b>
3.1. Introduction.....	66

3.2. Materials and Experimental Methods .....	69
<b>3.2.1. Materials</b> .....	69
3.3. Activation Process of the Carbon Cloth (CC).....	70
<b>3.3.1. Preparation of <math>\alpha</math>-Fe<sub>2</sub>O<sub>3</sub> Nanoparticles on CC and Activated Carbon Cloth (ACC)</b> .....	70
3.4. Materials Characterization .....	70
3.5. Preparation of the binder-free Electrodes and assembly of Symmetrical Device.....	71
3.6. Results and Discussion .....	72
<b>3.6.1. Microstructure and Morphology</b> .....	72
3.6.2. Electrochemical Performance of Binder-free Electrodes.....	80
<b>3.6.3. Implications</b> .....	87
<b>3.6.4. Summary and Concluding Remarks</b> .....	87
<b>REFERENCES</b> .....	88
<b>CHAPTER FOUR</b> .....	96
<b>4.0. Mechanical Properties of Polyvinyl Pyrrolidone /Polyvinyl Alcohol-based Solid Electrolytes</b> ..	96
4.1. Introduction.....	96
<b>4.1.1. Theory</b> .....	102
4.2. Materials and Methods.....	105
<b>4.2.1. Materials</b> .....	105
<b>4.2.2. Preparation of the Solid Polymer Blend</b> .....	105
4.3. Tensile Tests .....	107
<b>4.3.1. Fracture Tests</b> .....	107
<b>4.3.2. Nanoindentation Measurements</b> .....	108
<b>4.3.3. Materials Characterization</b> .....	109
4.4. Results and Discussions .....	110
4.4.1. Microstructures .....	110
<b>4.4.2. Indentation Measurements and Fracture Toughness</b> .....	113
<b>4.4.3. Result of Tensile Tests</b> .....	119
4.5. Deconvolution and mapping Results using Statistical Deconvolution Toolbox.....	120
4.6. Research Findings and Implications .....	123
4.7. Summary and Concluding Remarks .....	123
<b>REFERENCES</b> .....	125
<b>CHAPTER FIVE</b> .....	133
<b>5.0. Conclusion, Contributions to Knowledge, Challenges and Recommendations for Future work.</b> .....	133

5.1. Conclusion .....	133
5.2. Contributions to Knowledge .....	134
5.3. Challenges and Recommendations for Future work. ....	135

LIST OF FIGURES

**Figure 2:1** Schematic operation principle of a battery cell..... 10

**Figure 2.2** The supercapacitor taxonomy ..... 12

**Figure 2.3** EDCL device set up ..... 13

**Figure 2.4** : Graphene oxide synthesis by chemical oxidation method from graphite .....25

**Figure 3.1.** SEM micrographs (a) Untreated CC (b) Activated CC (c) 0.1g  $\alpha - \text{Fe}_2\text{O}_3\text{-CC}$  (d) 0.1g  $\alpha - \text{Fe}_2\text{O}_3\text{-ACC}$  (e) 0.2g  $\alpha - \text{Fe}_2\text{O}_3\text{-CC}$  (f) 0.2g  $\alpha - \text{Fe}_2\text{O}_3\text{-ACC}$ . HRTEM images (g) Unannealed  $\text{Fe}_2\text{O}_3$  (h) annealed  $\text{Fe}_2\text{O}_3$  .....71

**Figure 3.2.** XRD patterns (a) CC & ACC (b) unannealed  $\text{Fe}_2\text{O}_3$  and annealed  $\alpha\text{-Fe}_2\text{O}_3$  powder (c) 0.1 g and 0.2g  $\alpha\text{-Fe}_2\text{O}_3$  on CC, 0.1 g and 0.2 g  $\alpha\text{-Fe}_2\text{O}_3$  on ACC..... 73

**Figure 3.3.** Raman spectra (a) ACC & CC (b)  $\alpha\text{-Fe}_2\text{O}_3\text{-ACC}$  &  $\alpha\text{-Fe}_2\text{O}_3\text{-CC}$  ..... 74

**Figure 3.4.** XPS spectra (a, b) Long scan, (c, d) C1s, (e, f) Fe2p and (g, h) O1 peaks of the  $\alpha\text{-Fe}_2\text{O}_3\text{-CC}$  and  $\alpha\text{-Fe}_2\text{O}_3\text{-ACC}$  respectively. .... 75

**Figure 3.5.** Comparison (a) CV and (b) GCD curves of 0.1g  $\alpha\text{-Fe}_2\text{O}_3\text{-CC}$ , 0.1 g  $\alpha\text{-Fe}_2\text{O}_3\text{-ACC}$ , 0.2g  $\alpha\text{-Fe}_2\text{O}_3\text{-CC}$  and 0.2g  $\alpha\text{-Fe}_2\text{O}_3\text{-ACC}$ , (c) CV and (d) at different scan rate and at different specific current for 0.1 g  $\alpha\text{-Fe}_2\text{O}_3\text{-ACC}$ . ....81

**Figure 3.6.** EIS plots (a) for all the devices, (b) fitting of the Nyquist data for the  $\alpha$ -Fe<sub>2</sub>O<sub>3</sub>-ACC and (c) Efficiency as a function of the cycle number. ....83

**Figure 4.1.** (a) Sketch of Indentation load-displacement curve. (b) Energy release rate sketch for ease of calculation. ....100

**Figure 4.2..** (a) Flexible transparent film and (b) 3-D design of flexible film with Solid works software .....104

**Figure 4.3.** (a) Dog-Bone specimen (b) Schematics diagram of single edge notched specimen under tension .....105

**Figure 4.4.** SEM micrographs (a) PVA + PVP (b) PVA + PVP + 1 wt % LiClO<sub>4</sub> (c) PVA + PVP + 2 wt % LiClO<sub>4</sub> (d) PVA + PVP + 3 wt % LiClO<sub>4</sub> (e) PVA + PVP + 4 wt % LiClO<sub>4</sub> (f) PVA + PVP + 5 wt % LiClO<sub>4</sub> .....109

**Figure 4.5:** (a) XRD patterns of 2 wt% PVA: 2 wt% PVP with blends of various concentrations of Lithium perchlorate. (b) FTIR spectra of 2 wt% PVA: 2 wt% PVP with blends of various concentrations of Lithium perchlorate. ....111

**Figure 4.6.** Indentation Plots (a) Hardness Vs Displacement (b) Elastic Modulus Vs Displacement (c) Force Vs Displacement (d) Force Vs Time (e) Elastic Modulus Vs Hardness (f) 3-D image of polymer blend before indentation (g) 3-D image of polymer blend after indentation. ....113

**Figure 4.7.** (a) Plots of force-displacement curves, (b) fracture toughness values and (c) Optical images of failure mechanisms during fracture of the flexible polymer blends .....115

**Figure 4.8.** Plot of Tensile stress (MPa) against Tensile strain (%) .....117

**Figure 4.9.** (a) Statistical deconvolution mapping of Elastic Modulus (b) Statistical deconvolution mapping of Hardness (c) Elastic Modulus Vs Hardness (d) Probability density function (PDF) and cumulative density function (CDF) against Hardness (GPa) .....

118

## LIST OF TABLES

<b>Table 2.1:</b> Graphene and GO nanomaterials in EDLCs .....	27
<b>Table 2.2:</b> Carbon-based EDLC as electrode materials .....	34
<b>Table 3.1.</b> XPS peak fitting results for $\alpha$ -Fe <sub>2</sub> O <sub>3</sub> -CC and $\alpha$ -Fe <sub>2</sub> O <sub>3</sub> -ACC. ....	77
<b>Table 3.2.</b> Electrochemical measurements obtained at different mass concentrations .....	82
<b>Table 3.3</b> - Comparison of some Metal Oxide based composite electrodes .....	84
<b>Table 4.1.</b> Indentation measurements and tensile tests of the PVA/PVP/LiClO <sub>4</sub> Blend at different salt concentration. ....	112
<b>Table 4.2.</b> Summary of the fracture toughness values using single edge notched specimen under tension result.....	116
<b>Table 4.3.</b> Results of the statistical deconvolution mapping of mechanical properties from indentation experiments .....	119
<b>Table 4.4</b> PDF and CDF against Hardness (GPa) .....	120

## LIST OF ABBREVIATIONS

SCs: Supercapacitors

MSCs: Micro-supercapacitors

LiBs: Lithium-ion batteries

HEVs' Hybrid electric vehicles

EDLCs: Electric double-layer capacitors

ESS: Energy storage system

BESS: Battery energy storage system

CC: Carbon cloth

ACC: Activated carbon cloth

H<sub>2</sub>SO<sub>4</sub>: Sulphuric acid

H<sub>2</sub>O<sub>2</sub>: Hydrogen peroxide

HCl: Hydrochloric acid

FeCl<sub>3</sub>.6H<sub>2</sub>O,: Iron (111) Chloride Anhydrous

α-Fe<sub>2</sub>O<sub>3</sub> : Alpha-Iron (III) Oxide

Na<sub>2</sub>SO<sub>4</sub>,: Sodium Sulfate

HNO<sub>3</sub> : Nitric acid

C<sub>2</sub>H<sub>5</sub>OH : Ethanol

KOH: Potassium hydroxide

GCD: Galvanostatic Charge/Discharge

CV: Cyclic Voltammetry

EIS: Electrochemical Impedance Spectroscopy

HTM: Hydrothermal method

FTIR: Fourier Transform Infrared Spectroscopy

SEM: Scanning Electron Microscopy

HRTEM: High-resolution Transmission Electron Microscopy

XRD: X-ray Diffraction.

XPS: X-ray photoelectron spectroscopy

FEGSEM: Field-Emission Gun Scanning Electron Microscope

RAMAN: Raman spectroscopy

SSEs' Solid State Electrolytes

PVA: Poly {Vinyl alcohol}

PVP: Polyvinylpyrrolidone

LiClO<sub>4</sub>

:

Lithium

perchlorate

## CHAPTER ONE

### 1.0 Introduction

#### 1.1 Background

New research directions towards flexible electronics have greatly inspired the development of thin film energy storage devices [1], [2] as well as thin-film batteries [3] and micro-supercapacitors (MSCs) [4]. Supercapacitors (SCs) have exceptional properties such as high power density, long lifetimes, facile fabrication, low cost, and little or no maintenance requirements [5]. They are used in hybrid electric vehicles (HEVs) to increase efficiency. They can also complement or replace batteries in electrical energy storage applications [6]. Since hybrid vehicles turn off the engine completely when the car comes to a stop, supercapacitors can offer efficient power for rapid restarts. There is, therefore, an interest in the development of high performance energy storage devices like batteries and supercapacitors or its hybrids. The drive for supercapacitors is to develop an improved combination of high power density and high energy density. Furthermore, with the opportunities for further integration into electric or hybrid electric vehicles and other portable electronic devices, it is increasingly important for supercapacitors to be small, lightweight, stretchable and flexible. However, currently available supercapacitors with liquid electrolytes are limited by the leakage of electrolyte, low energy densities (both in weight and volume), and the low yield of the electrode materials. For the development of electrode materials, there are several materials that can be explored like carbon nanomaterials like graphene, carbon nanotubes, carbon nano onions, activated carbon, carbon aerogels, conducting polymers, composites of metal oxides [7]–[10]. Supercapacitors can be classified as either electric double layer capacitors (EDLCs), pseudocapacitors or hybrid

supercapacitors, these will be elaborated more in chapter two but suffice to state here that pseudocapacitive materials that store charges electrochemically have attracted significant attention in recent years due to their high theoretical specific capacity, as well as their high energy densities and environmentally friendliness. Transition metal oxides that have been explored as electrode materials include  $\text{RuO}_2$ , [11]  $\text{MnO}_2$  [12],  $\text{Co}_2\text{O}_3$  [13],  $\text{Co}_3\text{O}_4$  [14],  $\text{NiO}$  [15], [16],  $\text{Fe}_3\text{O}_4$  [17],  $\text{TiO}_2$  [18], and  $\text{V}_2\text{O}_5$  [19]. Carbon cloth is also being explored due to its attractive combination of flexibility, good electrical conductivity, high specific surface area, large capacitance, and chemical/thermal stability as well their versatile syntheses route [20]–[22]. Also, the development of solid state electrolyte will be explored. In the case of organic electrolytes and ionic liquids, they are associated with challenges of low ionic conductivity (high internal resistance), highly flammable, high electrolyte leakage and are quite expensive [23].

## 1.2 Problem Statement

In the energy sector, the conversion of different energy systems into electrical energy is a growing concern. Several methods of energy conversions like solar energy, wind energy, thermometric, photo-electrochemical etcetera with emphasis on renewable energy are being explored for conversion into electric energy. This increase in global energy generation has necessitated the drive for energy storage systems like batteries and supercapacitors that can be utilized to store excess power generation as well as during peak demand when production is very low. However, high cost of the fabrication of electrode materials, effects of addition of binder materials to the electrochemical performance, weight and environmental impact are major challenges. This research work explores the development of a one-step method for the processing of electrode materials for supercapacitors. A facile, one-step, hydrothermal method will be used to optimize synthesized  $\alpha\text{-Fe}_2\text{O}_3$  nanoparticles on carbon cloth and activated carbon cloth. The

latter and the former will be studied as binder-free flexible materials for the fabrication of stretchable symmetric supercapacitor electrode materials for energy storage. The  $\alpha$ -Fe<sub>2</sub>O<sub>3</sub> nanoparticles will be grown on conductive carbon cloth that will serve as a scaffold for quick electron transport, while providing strong support. The use of polymer binder/conductive additives will be avoided, while exploring the development of novel flexible supercapacitors with improved capacity for energy storage.

Similarly, since the conventional lithium-ion batteries (LiBs).which plays a major role in the market exhibits significant fire and explosion risks that are associated with the chemical instability of liquid electrolytes e.g. due to the presence of carbonates that are highly volatile and flammable [23]. This research work will also address these issues by developing a polymer solid-based electrolyte and studying the underlying mechanical properties so as to provide a robust solid electrolyte for application in energy storage devices.

### 1.3 Research Objectives

To produce efficient, low cost, light weight and binder-free electrode materials as well as the development of solid state electrolyte and subject it to test of mechanical properties for applications in supercapacitor as energy storage device.

. The specific objective of the study was as follows;

- i. To optimize the growth of  $\alpha$ -Fe<sub>2</sub>O<sub>3</sub> nanoparticles on carbon cloth (CC) and activated carbon cloth (ACC) using hydrothermal method.
- ii. To characterize the composition, morphologies and microstructures of the resulting electrodes materials.

iii. The resulting electrode materials are integrated as binder-free, symmetric device, which were then assembled and tested for electrochemical capacitors.

iv. Development of polymer-based solid electrolyte using a mixture of host polymers of Polyvinyl Alcohol (PVA), Polyvinyl Pyrrolidone (PVP) and lithium perchlorate ( $\text{LiClO}_4$ ) integrated into flexible and light-weight transparent films

v. Carry out test for Young's modulus, hardness, fracture toughness, tensile and deconvolution mapping to determine the mechanical properties of the flexible and light-weight transparent films

#### 1.4 Scope of the work

The scope of the study for the first research work was to optimize the growth of  $\alpha\text{-Fe}_2\text{O}_3$  nanoparticles on carbon cloth (CC) and also to study the impact of activation (functionalization) of the materials that can be used as electrode materials for applications in supercapacitors.

While for the second research work, the scope was the development of solid state electrolytes (SSEs) that are safe, environmentally friendly, with robust mechanical properties using a mixture of a polymer matrix of polyvinyl pyrrolidone (PVP)/polyvinyl alcohol (PVA) and lithium perchlorate salt ( $\text{LiClO}_4$ ).

## REFERENCES

- [1] M. Beidaghi, Y. Gogotsi, “Capacitive energy storage in micro-scale devices: recent advances in design and fabrication of micro-supercapacitors,” *Energy Environ. Sci.*, vol. 7, p. 867, 2014.
- [2] D. Ge, L. Yang, L. Fan, C. Zhang, and X. Xiao, “Foldable supercapacitors from triple networks of macroporous cellulose fibers, single-walled carbon nanotubes and polyaniline nanoribbons,” *Nano Energy*, 2014.
- [3] Z. L. C.J. Zhang, S.-H. Park, O. Ronan, A. Harvey, A. Seral-Ascaso, “Enabling Flexible Heterostructures for Li-Ion Battery Anodes Based on Nanotube and Liquid-Phase Exfoliated 2D Gallium Chalcogenide Nanosheet Colloidal Solutions,” *Small*, vol. 13, no. 1701677, pp. 1–11, 2017.
- [4] V. T. P. Huang, C. Lethien, S. Pinaud, K. Brousse, R. Laloo, “On-chip and freestanding elastic carbon films for micro-supercapacitors,” *Science (80-. )*, vol. 351, no. 6274, pp. 3717–3720, 2016.
- [5] Z. Liu, Z. Wu, S. Yang, R. Dong, X. Feng, and K. Müllen, “Ultraflexible In-Plane Micro-Supercapacitors by Direct Printing of Solution-Processable Electrochemically Exfoliated Graphene,” pp. 2217–2222, 2016.
- [6] P. Simon, Y. Gogotsi, “Materials for electrochemical capacitors,” *Nat. Mater.*, vol. 7, pp. 845–854, 2008.

- [7] B. G. Choi, M. Yang, W. H. Hong, J. W. Choi, and Y. S. Huh, "3D Macroporous Graphene Frameworks for Supercapacitors with High Energy and Power Densities," no. Xx, 2012.
- [8] L. L. Zhang, R. Zhou, and X. S. Zhao, "Graphene-based materials as supercapacitor electrodes," *J. Mater. Chem.*, vol. 20, no. 29, pp. 5983–5992, 2010.
- [9] P. Simon and Y. Gogotsi, "Capacitive Energy Storage in Nanostructured Carbon-Electrolyte Systems," *Acc. Chem. Res.*, vol. 46, no. 5, pp. 1094–1103, 2013.
- [10] Y. Gao *et al.*, "Chemical activation of carbon nano-onions for high-rate supercapacitor electrodes," *Carbon N. Y.*, vol. 51, pp. 52–58, 2013.
- [11] Z.-S. Wu *et al.*, "Anchoring Hydrated RuO<sub>2</sub> on Graphene Sheets for High-Performance Electrochemical Capacitors," *Adv. Funct. Mater.*, vol. 20, no. 20, pp. 3595–3602, 2010.
- [12] W. Wei, X. Cui, W. Chen, and D. G. Ivey, "Manganese oxide-based materials as electrochemical supercapacitor electrodes," *Chem. Soc. Rev.*, vol. 40, no. 3, pp. 1697–721, Mar. 2011.
- [13] X.-C. C. Dong *et al.*, "3D graphene-cobalt oxide electrode for high-performance supercapacitor and enzymeless glucose detection," *ACS Nano*, vol. 6, no. 4, pp. 3206–13, Apr. 2012.
- [14] S. K. Meher and G. R. Rao, "Effect of microwave on the nanowire morphology, optical, magnetic, and pseudocapacitance behavior of Co<sub>3</sub>O<sub>4</sub>," *J. Phys. Chem. C*, vol. 115, no. 51, pp. 25543–25556, 2011.
- [15] A. Bello, K. Makgopa, M. Fabiane, D. Dodoo-Ahrin, K. I. I. Ozoemena, and N. Manyala,

- “Chemical adsorption of NiO nanostructures on nickel foam-graphene for supercapacitor applications,” *J. Mater. Sci.*, vol. 48, no. 19, pp. 6706–6712, Jun. 2013.
- [16] D. Wang, W. Ni, H. Pang, Q. Lu, Z. Huang, and J. Zhao, “Preparation of mesoporous NiO with a bimodal pore size distribution and application in electrochemical capacitors,” *Electrochim. Acta*, vol. 55, no. 22, pp. 6830–6835, 2010.
- [17] N. Nagarajan and I. Zhitomirsky, “Cathodic electrosynthesis of iron oxide films for electrochemical supercapacitors,” *J. Appl. Electrochem.*, vol. 36, no. 12, pp. 1399–1405, 2006.
- [18] X. Lu *et al.*, “Hydrogenated TiO<sub>2</sub> nanotube arrays for supercapacitors,” *Nano Lett.*, vol. 12, no. 3, pp. 1690–6, Mar. 2012.
- [19] S. D. Perera *et al.*, “Vanadium Oxide Nanowire--Carbon Nanotube Binder-Free Flexible Electrodes for Supercapacitors,” *Adv. Energy Mater.*, vol. 1, no. 5, pp. 936–945, 2011.
- [20] M. Sevilla and A. B. Fuertes, “Direct Synthesis of Highly Porous Interconnected Carbon Nanosheets and Their Application as High-Performance Supercapacitors,” *ACS Nano*, vol. 8, no. 5, pp. 5069–5078, 2014.
- [21] M. Biswal, A. Banerjee, M. Deo, and S. Ogale, “From dead leaves to high energy density supercapacitors,” *Energy Environ. Sci.*, vol. 6, no. 4, pp. 1249–1259, 2013.
- [22] L. Miao, Z. Song, D. Zhu, L. Li, L. Gan, and M. Liu, “Recent advances in carbon-based supercapacitors,” *Mater. Adv.*, 2020.
- [23] K. X. L. Suo, O. Borodin, T. Gao, M. Olguin, J. Ho, X. Fan, C. Luo, C. Wang, ““ Water-in-salt ’ electrolyte enables high-voltage aqueous lithium-ion chemistries,” *Science* (80-

), vol. 350, no. 6263, 2015.

## Chapter Two

### 2.0 LITERATURE REVIEW

#### 2.1 Energy storage systems

The need to store harvested power (due to excess or demand during down time) in the form of energy has led to the development of the energy storage system (ESS) which in turn can be converted to electrical power on demand. It is to this end that the demands for energy storage systems are rising because of its numerous applications in portable devices, hybrid electric vehicles (HEVs) [1], [2]. Also, the global increase in population growth and industrial revolution has resulted in high emissions of greenhouse gases like CO<sub>2</sub> that deplete the ozone layers with high consequences of human existence due to environmental pollution hence the need for renewable energy and the attendant storage systems. There is no doubt that ESS, which forms an integral parts of the renewable energy matrix has a major role to play, hence the increasing research to optimize the development of energy storage systems. The essence of ESS is to create a back-up for stability and steady supply of energy during peak/down time [1], [3] .Also, ESS mitigates against power fluctuation which affects active electronics devices that could cause system malfunctions.

Similarly, to mitigate greenhouse effects, there is strong advocate of power generation using solar and/or wind energy which could trigger the used of electric cars powered by supercapacitors and batteries which are typical examples of energy storage systems (ESS) [1]. This trend has led to research in the development of suitable environmentally friendly electrode

and electrolyte materials for improved electrochemical performance. Vis-à-vis cost with robust mechanical properties [1]

### **2.1.1. Energy storage system components**

It is important to categorize the energy storage capacity of ESS according to their functions. These components are battery storage, reliable system operation, and grid connection. The battery system consists of the following;

- a) Cells made up of battery designed and built for a given voltage and capacity
- b) Systems that manages and protect the battery from external effects
- c) Thermal system to protect the cell from damaging operation like the voltage, current, and temperature aimed to provide controls for the temperature of the cells to optimal performance conditions [1].

### **2.2. Batteries Energy Storage Systems (BESS)**

The energy storage system-batteries (ESS-B) is rated as one of the most useful and efficient systems for stabilization of the electricity network system [1]. ESS-B are economical, low maintenance, compact, and easy to assemble in the network system. These are composed of several connected cells arranged in series or parallel which uses a chemical reaction process to convert electrical energy into chemical energy and vice versa. The lead-acid ESS-B is the most widely used technology for largescale production. The advancement of technology has resulted in new ESS-B which includes; Sodium-sulfur, lithium-ion, sodium-ion, lithium-sulfur, sodium-nickel chloride, nickel-cadmium, metal-air, magnesium ion, and other several technologies as secondary cells [1]. A battery system consists of cells composed of two electrodes namely anode and cathode and the electrolyte. If the anode and cathode are of same material, it is said to be symmetric but if different materials, it is asymmetric. The assembly of electrodes and

electrolytes is kept close in a sealed container to avoid interaction with the atmosphere. The electrolytic ion exchange between the electrodes creates the flow of electrons through the system to the external circuit as shown in Figure 2.1.

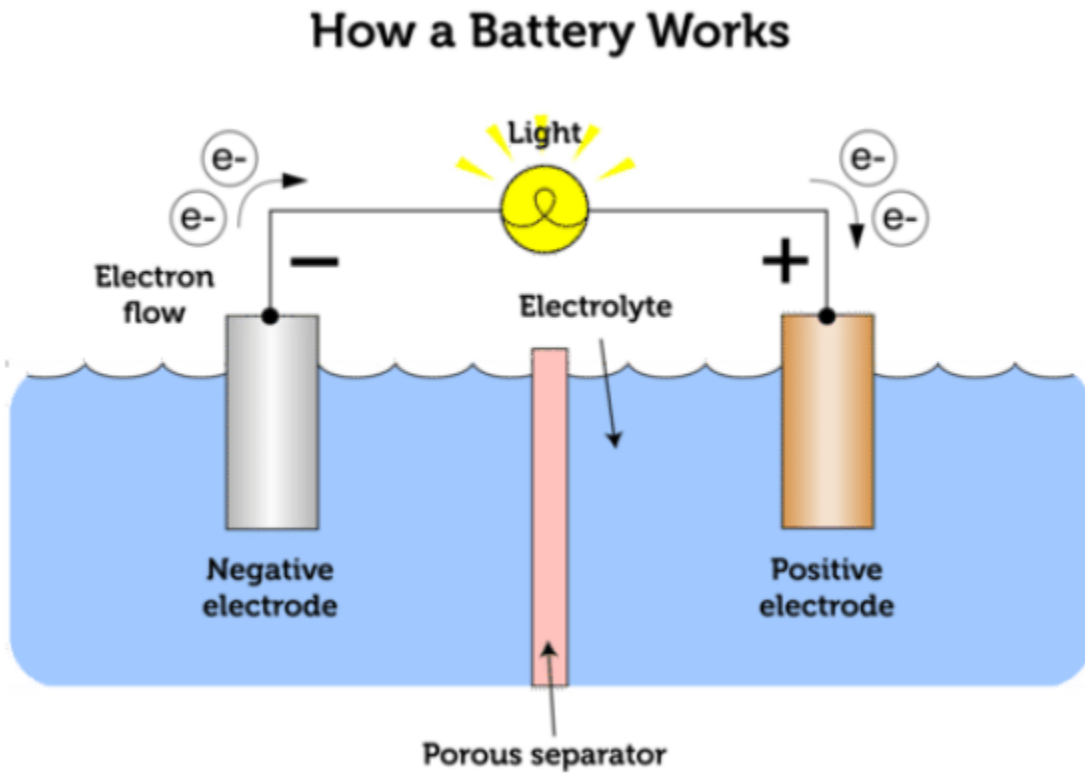


Figure 2:1 Schematic operation principle of a battery cell. [1]

### 2.3. Energy Storage System-Supercapacitors (ESS-SCs)

Supercapacitors as an energy storage system have demonstrated capacity for high power density with features for improved energy density and could serve as complimentary or possible alternatives for batteries. [1]

$$E = \frac{1}{2}CV^2 \dots\dots\dots(2.1)$$

where  $E$  is energy,  $C$  is capacitance and  $V$  is voltage. The major thrust of the development of supercapacitors is to use material(s) with high capacitance and voltage to improve the energy density which is achieved by using multi-functional electrode materials with smart designs. The chemical and physical characteristics of the electrode materials are responsible for the high energy conversion and storage. The effects of the double layer supercapacitor's capacitance is generated from pure electrostatic charge accumulated at the electrode/electrolytic ion interface. The capacitance of SCs is defined by the electrochemical double-layer capacitor (EDLC) materials or pseudo-capacitor coming from reversible redox (Reduction and oxidation) reactions. When the SC combines both mechanisms it is called hybrid SC as shown in Figure 2.2 [4]. The electrode materials used in SC are the most important component of the SC. [5].. The supercapacitors electrochemical performance largely depends on surface area, pore volume, electrical conductivity, electrolyte ions permeability etc.[5]

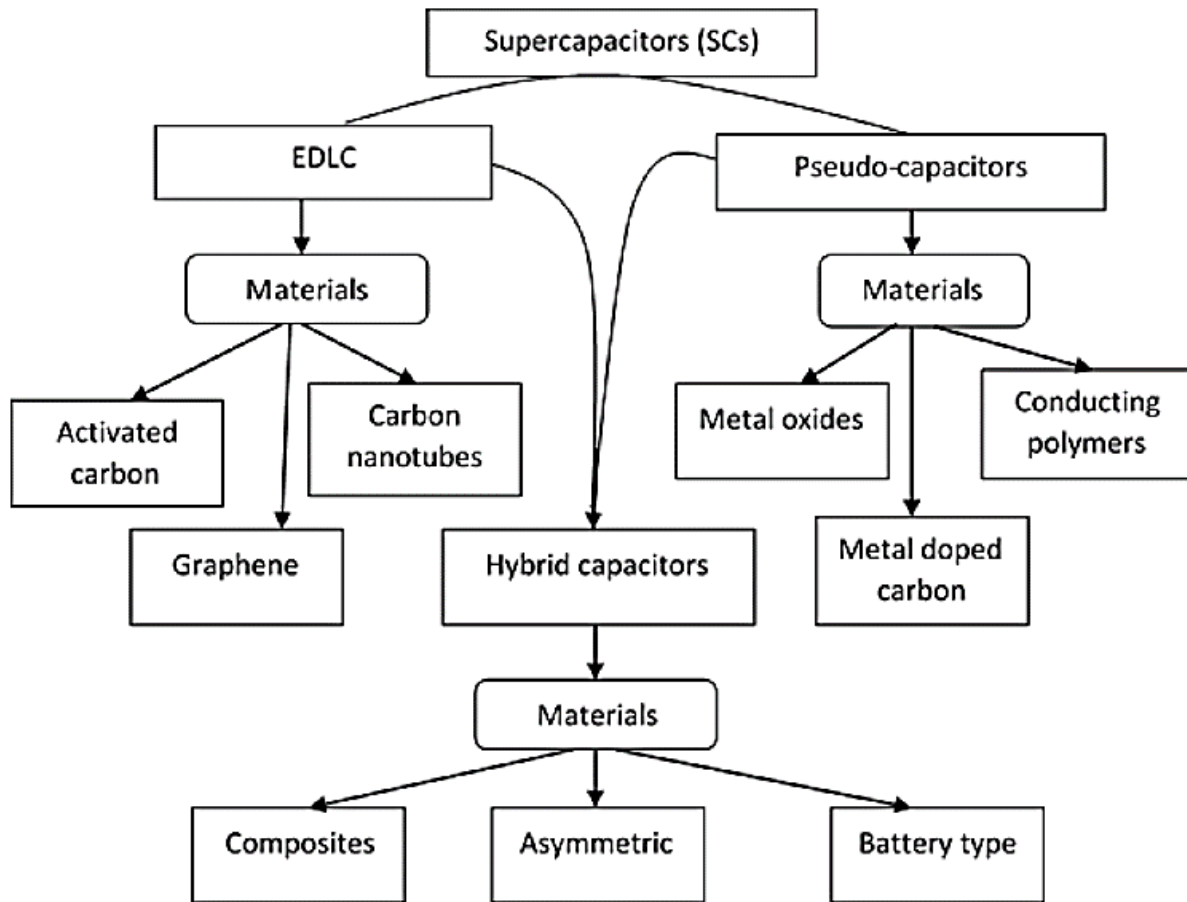


*Figure 2.2 The supercapacitor taxonomy [1], [4]–[6]*

### 2.3.1. Electric double-layer capacitors (EDLC)

From figure 2.3, we can see that the EDLC is a principle based on the electrostatic charge stored between the electrode material and the electrolyte solution interface or by a non-faradaic process which is a principle that conveys no transfer of charges between electrolyte and electrode. On application of voltage to a setup of supercapacitors, charges are accumulated on the surface of the electrode as a result of potential difference, opposite charges are attracted given rise to diffusion of electrolytic ions over the separator to the opposite electrode. According to [4], the formation of a double layer at the surface of the electrode is to avoid the ions recombining. The

effects of this process result in decrease in the electrode distance as a result of increase in surface area so that the electrochemical double-layer capacitor can achieved higher energy density.

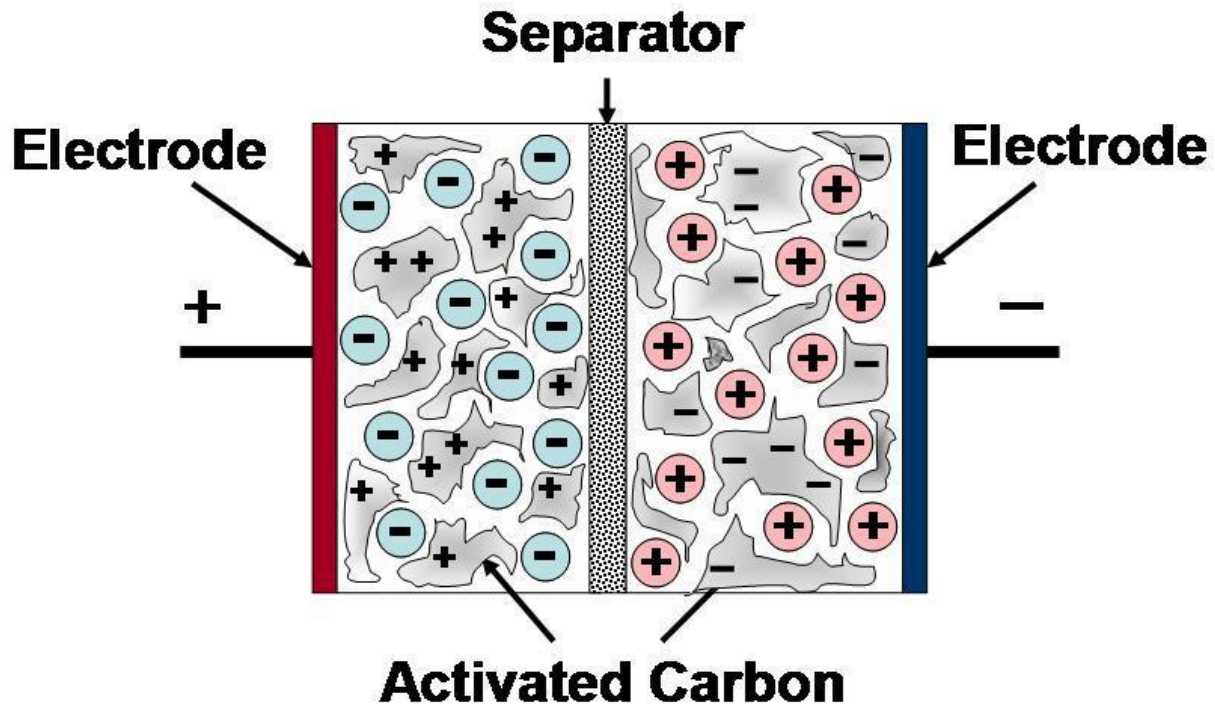


Figure 2.3 EDCL device set up [1]

The fundamental equation for all capacitors to determine the capacitance is shown in equation 2.2 [4], [7]

$$C = \frac{A\epsilon_r\epsilon_o}{d} \dots\dots\dots (2.2)$$

Where A is the surface area of the used electrode,  $\epsilon_o$  is the permittivity of free space,  $\epsilon_r$  is the relative permittivity of the dielectric material and d is the distance between two electrodes.

As seen in from equation (2.2), the capacitance of a capacitor can be enhanced by increasing the dielectric constant of the material, increasing the surface area, and decreasing the distance of the electrodes. Similarly, you can increase the pore volume, surface area, particle size which are all

material properties. The charge and discharge cycles of the EDCL are highly reversible because of the non-faradaic behaviour of the electrical mechanism.[1], [8] The EDLC storage principle allows a very fast energy uptake, better power performance, and delivery due to the non-faradaic process which causes no chemical reaction. The non-faradaic process prevents swelling and expansion of active materials which is common in batteries during the charge-discharge process. [1]

### **2.3.2. Pseudo-capacitors**

The Pseudo-capacitors utilizes the transfer of charges between the electrode and electrolyte using the faradaic process of storing charges. [5] stated that when a voltage is applied to a pseudo-capacitor device, it triggers a reduction-oxidation (redox) reaction on the surface of the electrode due to transfer of charges across the double –layers which generate a faradaic current in the supercapacitor cell. This process creates higher energy density and specific capacitance than materials made up of EDLC. Examples of pseudo-capacitors electrode materials are metal-oxides, conducting polymers, metal doped carbon etc., however, they have stability limitations during long cycles as well as low power density [4].

#### **2.3.2.1. Conducting polymers**

The conducting polymers as a type of supercapacitor is capable of high conductivity at low electrical series resistance (ESR) at comparative low cost to EDLC from carbon based supercapacitors. Examples of this kind of supercapacitor are polyaniline, polythiophene, polypyrrole etc and they are characterized with high potential density [1], this characteristics is due to its high conductivity and flexibility to enhance capacitance [8], however, like pseudo-capacitor supercapacitors, they are limited by low cyclic stability compared to supercapacitors from carbon-based materials. [4] stated that doping is required to increase its conductivity which

could affect device performance due to increase in volume and by extension its thickness as a result of swelling

### **2.3.2.2. Metal oxides pseudocapacitors**

Metal oxides pseudo-capacitors kind of supercapacitors gives high specific capacitance as a result of its high conductivity, however, it has a comparatively high cost. Their usage in the supercapacitor industry is still low as a result of its method of fabrication like hydrothermal synthesis, spray deposition, oxidation, sol-gel, intercalation, anodic deposition, insertion etc. [8]. They are capable of improving capacitance at lower current density but have challenges of short term stability due to crack or defects in the electrode stability [8] which can be overcome when in composite with carbon [4].

### **2.3.3. Hybrid supercapacitors (HSC)**

As the name suggests, this hybrid-supercapacitors (HSC) is a combination of pseudo-capacitors and EDLC as it explores the high power and energy density of the battery-like electrode and capacitor-like electrode respectively. It takes advantage of the mixture of carbon and conducting polymer or metal electrode capability to store the charges as well as ability to use faradaic and non-faradaic processes to achieve high energy storage in the electrode [9] to achieve improved cyclic stability and low cost compared to EDLC. According to [4], [5], the electrode mixtures are classified as either asymmetric, Battery-type, or composite.

#### **2.3.3.1. Asymmetric hybrid supercapacitors**

This uses the process of faradaic and non-faradaic of the EDLC and pseudo-capacitor properties of the electrode together. For the asymmetric configuration, carbon is mainly the negative electrode with either conducting polymer or metal oxide as the positive electrode [1], [5]. They

are set to work simultaneously to reach high power and energy density requirements. One electrode will be a capacitive electrode and the other will be a faradaic electrode. The metal oxide electrodes have a high intrinsic volumetric capacity which leads to an increased energy density [10]

This kind of configuration demonstrate higher energy density and excellent cycling stability compared to symmetric supercapacitors [4]. These capacitors has a limitation of short self-discharge which can be improved by introducing a simple rocking chair mechanism to ensure maximum potential at zero current [1]. There is also a possibility of electrolyte ion depletion of the electrodes causing a decrease in conductivity with an increase in the internal resistance [4].

#### 2.3.3.2. Composite hybrid SC

These SC employ composite electrodes with a combination of carbon-based materials with either conducting polymer or metal oxides in a single electrode. The single electrode will contain both chemical and physical charge storage mechanisms. The capacitive double layer of charges offered by carbon-based materials and improves the contact between the electrolyte and the pseudocapacitor materials. The composite electrode materials increase capacitance with faradaic reaction [1], [9]. The composite electrode materials include binary and ternary composite. The binary composites use two different electrode materials and the ternary composite uses three different electrode materials for a single electrode [5], [11].

The objective of the composite hybrid is to have synergistic results of specific capacitance, excellent cycling stability, and high conductivity. The conductivity of composite is highly tuneable but it depends on carbon structure and the porosity [6]. This makes pore diameter and important factor that determines the ions' absorptivity on the surface of the electrode to define

charge-discharge characteristics composite materials have a limitation when successive ion diffusion reduces to protruding nano whiskers which grow on the carbon nanofibers even through the surface area of the metal oxide increases [4].

### **2.3.3.3. Battery-type hybrid**

The battery-type hybrids are situated around the centre position of the Ragone plot with capability for higher specific capacitance, power density, and energy density. This kind of energy storage system makes use of two different electrodes like asymmetric hybrids. They use a mixture of battery and supercapacitors electrodes to explore the properties of both in a single cell [1], [4]. These combinations develop an electroactive nanoparticle which leads to faster reactions with the electrolyte hence leading to a redox faster reaction process. The electrode materials create a Helmholtz double layer where the charge is stored at the interface between electrolyte and carbon electrode [6]. This result at the interface due to like-charges being repelled from each other and attraction in the counter ions which causes a mechanism in physical charge storage [4].

## **2.4. Carbon-based electrode materials**

The development of electrode for supercapacitors applications using carbon materials is a growing concern. The applications of carbon material is due to its exceptional properties of low cost, availability, environmentally friendly, high surface area, and facile synthesis. The storage mechanism involved in carbon materials is the electrochemical double layer occurring at the interface between the electrolyte and electrode. The capacitance of the material depends on the surface area, pore size distribution, surface functionality, pore shapes and structure, and electrical conductivity [1], [5]. The high specific surface area in carbon materials leads to a high capability for the accumulation of charges at the interface of the electrolyte and electrode. Some of the

carbon materials used as electrode materials include; graphene/graphene oxide, activated carbon, carbon nanotubes, carbon onion, carbon aerogel etcetera [1]

#### 2.4.1. Graphene/graphene oxide

This material has become highly sourced for and used since its discovery by Novoselov and Geim in 2004 as stated by Kigozi [1]. The graphene is an  $sp^2$ -bond flat sheet thin layer. The 2-dimensional honeycomb lattice of carbon arranged with fully conjugated structures of alternating C=C and C-C bonds. Its suitability for the development of an energy storage system is as a result of its unique quasi-metal physical-chemical. The use of graphene as a material for an electronic application requires specific functionalization of the graphene sheets into their derivative at a molecular level. This makes surface functionalization of graphene sheets an important aspect using different covalent and non-covalent methods for making graphene materials with the bulk and surface properties required for potential application which include energy conversion and storage. The excellent electrical, high mechanical strength, thermal conductivity, and theoretical surface area ( $2600\text{m}^2/\text{g}$ ) make it suitable for energy storage devices[1], [7]. The functionalized graphene is graphene oxide (GO) with functional groups on the surface and the allotropes like 3D-graphite, 1D carbon nanotubes all have hexagonal rings structure with different orientations in space [12].

Graphene can be activated using several methods such as: exfoliation method, introducing spacers between its layers, templating technique, or forming hydrogel by reducing graphene oxide. For application purposes, graphene is not used as pristine but it has to be applied as reduced graphene oxide or doped graphene or activated graphene or graphene/polymer composites or graphene/metal oxide composites [1], [7] Literature reported new carbon material by chemical modification of one-atom-thick layer of graphene with specific surface area 705

$\text{m}^2/\text{g}$ , which exhibited high specific capacitance of 135 F/g in aqueous electrolyte and 99 F/g in organic electrolyte. Also, exhibited good retention ability over a wide range of voltage scan rates (Muhammad Khalid, 2019). Another literature reported the synthesis of graphene with thermal exfoliation of graphitic oxide at a very high temperature of 1050 °C which demonstrate a high surface area of 925  $\text{m}^2/\text{g}$  and specific capacitance is 117 F/g in aqueous 2M  $\text{H}_2\text{SO}_4$  electrolyte. Alternatively, functionalization of graphene can also be attained by controlled thermal exfoliation at low temperatures [1], [13] without compromising its capacitance performance. Chemical functionalization of graphene oxide platelets grown on highly porous, intrinsically flexible, and ordered carbon films by nitrogen doping [7] has proven to increase its electrical as well as super-capacitive properties. The above-discussed activation methods have led to the production of materials with high capacitance but for actual practical application of these materials, the other important factor to be considered is energy density. The commercially accessible batteries have higher energy density than supercapacitors. This means that supercapacitors can provide a very high energy pulse when required but can store less energy per unit weight, as compared to batteries. The literature reported the synthesis of 1-layer graphene in a curved form which limited the face-to-face restacking of its sheets, hereafter, utilizing maximum possible electrode surface. This resulted in supercapacitor electrode material with a very high specific energy of 86 and 136 Wh/kg at room temperature and 80°C respectively at 1 A/g current density [9] . There is also a description for the development of sponge-like graphene nanostructures that exhibited a high energy density of 48 kW/kg. There is a new approach to efficiently maximize the surface of each layer of graphene structure by using the “in-plane” strategy in place of stacking [14]. Unlike conventional (stacked) assembly, the entire electrochemical (specific) surface area cannot be used because some of the regions are

unapproachable to the electrolyte ions. Although, the new structural design assists the percolation of electrolyte ions between graphene layers to reach the current collector. Therefore, facilitating the high usage of available specific surface area [14]. This type of in-plane 2D graphene supercapacitor has shown a high specific capacitance of 250 F/g at current density 176 mA/g with good retention rate for 1500 cycles.

#### 2.4.2. Graphene-Metal oxide composite

Some carbon-based materials are carbon nanotubes, carbon quantum dots, graphene, and nitrogen-doped carbons that can be used as single electrode materials because of their unique electrical, structural, and mechanical properties. However, they demonstrate low volumetric capacitance performance and are hard to fabricate. Composing nanocarbon like graphene applied to supporting 3-D activated carbon matrices may create high-capacity composite electrodes [1], [15]. Furthermore, the nanoworld may be too far from practical realities. Nanomaterials that can display outstanding performance at low electrode loading in research testing may not fit heavily loaded electrodes which are necessary for practical devices. Composite materials may provide the right solution for active nanomaterials embedded in micrometric size carbonaceous matrices that can serve as a robust active mass with excellent inter-particles electronic contact and appropriate mechanical stability [16] Embedding nanocarbon like graphene or nanotubes may create mesoporous structures with high specific surface area and excellent cycle stability. For SCs applications, the porosity of the electrode material is a crucial factor and proved to be highly established when various nanocarbon are embedded in activated carbon matrices. This can help achieve materials that are interesting synergy in which the carbonaceous matrix stabilizes the active nanoparticles, thus improving their charge storage capability, and the latter moieties, in

turn, stabilize meso-porosity of the composite matrices what enables to obtain high-rate capability [1], [12].

The MnO<sub>2</sub>/CNT composite was prepared using a simple hydrothermal treatment. The MnO<sub>2</sub>/CNT nanocomposite electrode displayed a higher specific capacitance and rate capability compared to pure MnO<sub>2</sub> and CNT electrodes. High specific capacitance gotten in the composite can be attributed to the high specific surface area of MnO<sub>2</sub> and high porous structure [5]. In literature, an asymmetric supercapacitor was assembled using MnO<sub>2</sub> and graphene. The prepared composite of MnO<sub>2</sub>-coated/graphene was used as a cathode while pure graphene was used as an anode. The process of electro-activation was used on a graphene electrode where a capacitance of 245 F/g at a charging current of 1 mA was reported. When MnO<sub>2</sub> was deposited, the capacitance increased to 328 F/g at the same charging current resulting in an energy density of 11.4 Wh/kg and a power density of 25.8 kW/kg [5]

CNT and graphene can be surface functionalized by metal oxide, polymers, or oxidizing to be stunned by the presence of some impurities. In research carried out CNT/ MnO<sub>2</sub> composite, first, it was observed that there was a vertical alignment in CNTs resulting in a higher capacitance as compared to random ones. This indicates that morphology affects capacitance significantly. Secondly, when water plasma treatment was applied on the surface, it gave higher results due to the clearer and larger active surface of nanotubes. Lastly, the addition of MnO<sub>2</sub> via the electrochemical deposition technique exhibited the highest specific capacitance of 475 F/g [5]. When carried out using a composite of reduced graphene oxide (RGO) with molybdenum sulfide (MoS<sub>2</sub>) synthesized by a simple process of one-pot hydrothermal. The resultant composite exhibited a specific capacitance of 253 F/g at a current density of 1 A/g with excellent cycling stability [4].

Activated carbon having good properties like large-good electrical properties, surface area, and the moderate cost was used in three different metal oxides Cobalt (Co), Nickel (Ni), and Manganese (Mn) for different combinations to produce the highest specific capacitance. The AC was used as anode and a combination of any two of the metal oxides as a cathode. The degree of inversion was diverse by a factor of 0.2 to study the effect on the performance. A combination of 12 different samples was organized and the highest specific capacitance was 78 F/g from (Mn<sub>0.6</sub>Co<sub>0.4</sub>) which was due to large pores that were examined from the SEM images that allowed easy diffusion of electrolyte. The least value was 5F/g for (Mn<sub>0.8</sub>Co<sub>0.2</sub>) due to a non-uniform crystalline image with a hairy surface that made it difficult for electrolytic ion movement [9]

Several metal-oxides like MnO<sub>2</sub>, RuO<sub>2</sub>, TiO<sub>2</sub>, NiO, ZnO, Fe<sub>3</sub>O<sub>4</sub>, MnO<sub>2</sub>, MoO<sub>3</sub>, Mn<sub>3</sub>O<sub>4</sub>, Co<sub>3</sub>O<sub>4</sub>, and CoMoO<sub>4</sub> [1], [7] among others have been used as possible electrode material in supercapacitors [1], [17]. When these active materials are added to the graphene structure in an appropriate quantity, they can exhibit an excellent electrode material performance. When added, the metal oxide nanoparticle acts as nano-spacers between the graphene layers to prevent it from restacking. Also, the free space between the 2-D graphene sheets creates a smooth horizontal way for the mobility of the electrolytic ions hence improving the energy storing capacity. The literature described the supercapacitor behaviour of graphene-SnO<sub>2</sub> and graphene-ZnO composite materials [14]. They found that the electrochemical performance of graphene-ZnO composite was improved to a great extent in terms of capacitance value and reversibility when compared to pristine SnO<sub>2</sub> or ZnO or graphene. The specific capacitance of 61 F/g and energy density of 4.8 Wh/kg was reported, which was greater than that of graphene-SnO<sub>2</sub> samples. Graphene- MnO<sub>2</sub> composite with high MnO<sub>2</sub> content (78 wt.%) exhibited a specific capacitance

of 310 F/g at a scan rate of 2 mV/s. The literature claims that hybridization of MnO<sub>2</sub> and graphene caused an increase in the specific surface area exhibiting a higher conductivity and that led to a high-performance rate [14]. Besides conventional symmetric supercapacitors, several studies have been carried out to exploit the potential of asymmetric supercapacitors devices based on metal oxide/graphene composites [1], [14]. Fabrication of asymmetric supercapacitors aims to attain a higher energy density. The most crucial step when assembling is the choice of two such electrodes that have the same working potential range and appropriate wettability in the same electrolyte. This allows the extension of the operating potential window along with the enhanced capacitance performance rate. In literature, a study established that an asymmetric supercapacitor assembled using MnO<sub>2</sub> nanoparticles as anode and graphene as cathode displayed a specific capacitance of 37 F/g and could operate up to a voltage range of 2.0 V with capacitance retention of 96% for 500 cycles. This displayed a much higher energy density of 25.2 Wh/kg and power density of 100 W/kg when compared to 4.9 Wh/kg of MnO<sub>2</sub>/ MnO<sub>2</sub> and 3.6 Wh/kg of graphene/ graphene-based symmetric supercapacitors [14].

The planar SC was fabricated by using a  $\delta$ -MnO facial assembly set with reduced graphene oxide (RGO) flakes. The interactions caused due to morphologically and the synergic interaction with electrostatic effects was enhanced by the RGO and MnO<sub>2</sub> nanosheets integration. Synthesis of graphene aerogels (GA) has also been reported in the literature using a sol-gel method [18]. The synthesized GA exhibited a good specific surface area of 793 m<sup>2</sup>/g, a high pore volume of 3 cm<sup>3</sup>/g, and a high specific capacitance of 410 F/g. The effect of the 3D network of GA support and the structural advantages resulted in good stability with depletion of 5% in 50,000 cycles and capacity of 410 F/g. An outstanding electrical and mechanical property of 3D graphene foam has been reported using the CVD synthesis of graphene foam (GF) on nickel foam (NF). This was

followed by the  $\text{CoMoO}_4$  [1] and  $\text{MnO}_2$  [17] hydrothermal deposition. There was no need for any other metal current collector since graphene has good mechanical and support conductance. The specific capacitance of 144 F/g for GF-Ni (OH) and 439.7 F/g for GF- $\text{CoMoO}_4$  was reported with a power density of 44 W/kg and 900 W/kg respectively which describe its usage for stretchable and flexible SCs due to its structural property and superior electrochemical. Literature reported about the graphene nanocomposites employing an in-solution process [17] with the  $\text{Co}_3\text{O}_4$  and  $\text{Mn}_3\text{O}_4$ . Using Hummer's method for synthesis of graphene oxide (GO) and the precursor solution was intermixed with the graphene oxide. The  $\text{Mn}_3\text{O}_4/\text{Co}_3\text{O}_4$  composite was deposited onto the RGO using thermal and microwave to assist the treatment carried out. The cobalt oxide nanoparticle microwave-assisted intercalation was also proposed using graphene wrapping [19].

Nanostructured carbon-based electrode materials are most widely used for electrochemical applications due to their good electrical properties, low cost, chemical and thermal stability, and good reversible redox reaction feasibility. Though, these properties do not offer good energy density-high specific capacitance and stable cycle life. To overcome these defects, the nanostructured carbon-based materials are mostly combined with the metal oxides. Thus, the designing of an electrode with flexible carbon fiber foam (CFF) and  $\text{MnO}_2$  has been employed as advanced research that contributes to the electrochemical behaviour during both the charging and discharging period. The choice of CFF as the current collector is due to its high corrosion resistance, easy fabrication, low cost, 1D structure, and high electrical conductivity.  $\text{MnO}_2$  had been recognized as a promising candidate for its simple synthesis process [6].

A few researchers have successfully developed a solid-state highly flexible CFF/ $\text{MnO}_2$ -based electrode material for supercapacitor applications. Hydrothermal synthesis is one of the methods

used to functionalize CFF with coral-like MnO<sub>2</sub> nanostructure for the improvement of the pseudocapacitive properties [20]. The specific capacitance of 467 F/g with 100% initial capacitance maintenance after 5000 cycles is attributed to the presence of the unique structure of the electrode which permitted fast ion diffusion. Also, observed an energy density of 20 Wh/kg and faster charge and discharge rates. Morphology of the thermally aged CFF/MnO<sub>2</sub> and CFF hybrids were examined after reaction at 175 °C. In the report, observations made by the FESEM images exposed the interaction between CFF and MnO<sub>2</sub> which was quite strong and the CFF acted as a good substrate. In addition to these, an energy density of 20 Wh/kg and power density of 0.175 kWh/kg was reported for the devices fabricated with CFF/MnO<sub>2</sub> [6].

Graphene and graphene oxide (G/GO) are used in SCs applications because they do not depend on the distribution of pores in the solid-state as compared to other carbon materials [5]. If the theoretical SSA is fully utilized, graphene can produce a capacitance of 55 F/g [11]. When graphene is used as an electrode material, all major surface sheets are readily available for electrolyte interaction. The synthesis of GO by acid oxidation of graphite [11] followed by chemical reduction, provides an effective method for low-cost mass production of reduced graphene oxide (RGO) that can directly be used as EDLC electrode materials. The traditional way of producing graphene is initiated by graphite using the oxidation method to form graphene oxide. This is achieved by Hummer's method or modified Hummer's methods and other methods as shown in Figure 2.4. For producing GO sheets, a complete exfoliation of graphite oxide can mechanically be carried out by sonication [6].

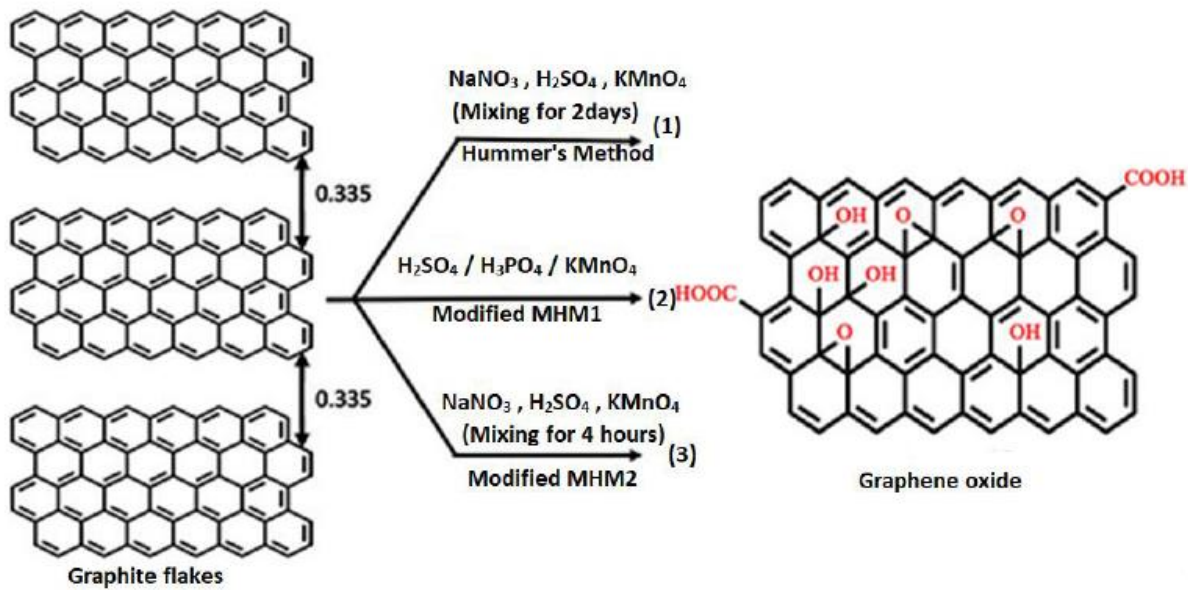


Figure 2.4 : Graphene oxide synthesis by chemical oxidation method from graphite [1]

The method of producing graphene is the chemical oxidation. A functional groups like hydroxyl, carbonyl, and peroxy is introduced between carbon layers of graphite. These functional groups weaken the binding van der Waal bonds between carbon layers to peel off layer by layer from graphite [6]. The resulting GO can be reduced to graphene by adding hydrazine solution into the GO solution. The reason why graphene with high surface area is desirable is because it significantly reduces high inter-sheets contact resistance compared to graphene with smaller area. The limitation of graphene sheets is that it easily forms restacks and irreversible agglomeration to their graphite structure which makes determining intrinsic capacitance difficult. The graphene-based SCs are capable of operating up to a potential of 4.5V and an energy density of 85.6Wh/kg at room temperature and 136Wh/kg at 80 °C in the ionic liquid [11].

The oxides of graphene work as an important alternative material to be used for nanocomposite formation. To improve the electrochemical properties of graphene-based electrodes, the materials have to be doped with chemicals having electron donors and acceptors. From the literature, a

specific capacitance of 242 F/g was reported by using N-doped-graphene oxide for SC with a capacitance of 320 F/g obtained from highly nitrogenated graphene oxide [1]. The GO synthesized by modified hummer's method was experimented on a 2.5 to 7.5 A/g and the highest current density of 7.5 A/g produced energy density of 58.25 Wh/kg and power density of 13.12 kW/kg [5]. The conventional graphene and RGO electrodes with electrolyte ions can only transfer charges between graphene sheets that inevitably leads to a much longer ion-transport path with their ions transferring through the graphene sheets. Kigozi [1] reported that hollow-graphene sheets can allow ions to a path through the holes with limited transport path while keeping the electron-transport efficiency. Doping graphene using hetero-atoms can improve the electrochemical/electrical properties of energy storage including other properties of energy storage [1]. Several works of literature have been reported with doping and improvement with GO as shown in Table 2.1.

Table 2.1: Graphene and GO nanomaterials in EDLCs [1]

<b>Electrode</b>	<b>Electrolyte</b>	<b>Specific capacitance (F/G)</b>	<b>Energy density (Wh/Kg)</b>	<b>Power density (Wh/Kg)</b>	<b>References</b>
G – functionalized - OH & -COOH	0.075 M hydroquinone & 1MH <sub>2</sub> SO <sub>4</sub>	3199 at 5mV/s	-	-	(G. Wang et al., 2014)
Hollow graphene	EMIMBF <sub>4</sub> /AN	298 at 1A/g	53	1000	(Y. Xu et al., 2014)
N-doped graphene	1M TEABF <sub>4</sub>	280 at 20A/g	48	800	(Y. Liu et al., 2016)
N/P doped RGO	6M KOH	165 at 0.1A/g	-	-	(Ke & J., 2016)
Graphene aerogel	3M KOH	4.76 at 0.4A/g	0.26	4080	(Zhu C, 2016)
Graphene aerogel	0.5M H <sub>2</sub> SO <sub>4</sub>	325 at 1A/g	45	7000	(Jung et al., 2015)
2D micro porous GO	EMMBF <sub>4</sub>	151.3 at 0.1A/g	42	10000	(Hao L, 2015)
N-doped GO	6M H <sub>2</sub> SO <sub>4</sub>	396.5 at	-	-	(Jia, Y, & G,

Graphene / CNT	PVA/H <sub>3</sub> PO <sub>4</sub>	0.2A/g 31.5 at 0.04A/g	-	-	2016) (H. Sun et al., 2014)
Free standing graphene	1M Na <sub>2</sub> SO <sub>4</sub>	150.2 at 1A/g	-	-	(G. Sun et al., 2015)
RGO/Fe <sub>2</sub> O <sub>3</sub>	Organic solvent	855.2mAh/g at 0.02A/g	129.6	1870	(M. Li et al., 2016)
RGO/Cu	-	81.3	11.25	5000	(Purkait et al., 2018)
Metal oxide/RGO	H <sub>3</sub> PO <sub>4</sub> /PVA	281.3F/cm <sup>3</sup>	18.2 mWh/cm <sup>3</sup>	76.4 mW/cm <sup>3</sup>	(W Ma et al., 2016)
C-GO	6M KOH	329.5 at 0.5A/g	-	-	(Y. Song et al., 2016)
MnO <sub>2</sub> CNT/GO	6M KOH	210 at 1mA/cm <sup>2</sup>	24	10000	(Leea & B-H, 2016)
CoO/GO	2M KOH	889 at 2A/g	28.7	1600	(R. Wang et al., 2017)

## 2.5. Activated carbon (AC)

The growing increase in the practices of agricultural crop production has led to an increase in the production of biomass waste. The conversion and utilization of the biomass waste into value-added materials cannot be over emphasised. Biomass such as maize corn cobs, rice husks, coconut shells, sugarcane bagasse etc. has been explored for the production of porous activated carbon for industrial applications [1], [21]–[27] The Activated Carbon (AC) with varying surface areas are abundantly being used for industrial applications which includes energy storage materials, removal of toxic compounds, purification, and separation in liquids and gases, catalysts or catalysts support [1], [23], [28], [29], reduction in CO<sub>2</sub> [30] removal of dyes and odour [29].

Zea Mays (Maize or corn) is the most widely cultivated cereal grain food in Africa. This is widely used in most homes as support for food and income-earning for the rural economy. [1] The production yield per hectare (tons/hectare/year) of approximately 30 YPH by 2018, which

was greater than the USA, China and Brazil combined at 22 tons/hectare/year [1]. Normally, the maize corn cobs are treated as agricultural crop residue/waste as a result of harvesting where only the grains are taken for further processing and the cobs are disposed-off in the farm, power plant sites, and others are burnt to ashes. There are two major methods for conversion of biomass like corn cobs into AC which are; Chemical and physical activation [23], [29]. The physical activation has mainly two (2) stages namely; carbonization of the carbonaceous material and activation at elevated temperatures in a suitable atmosphere of gases like Argon or Nitrogen [1]. This process results in the removal of some volatiles, hence producing a wide range of pores which creates porous AC. This method has been adopted in industries for commercial production of micro-porous AC because of its environmental sustainability.

For the chemical activation process, the precursors (biomass) are impregnated with chemicals having dehydrating properties such as  $H_2SO_4$ ,  $H_3PO_4$ ,  $ZnCl_2$ ,  $K_2CO_3$ ,  $NaOH$ ,  $KOH$  to mention but a few. These are used to carbonize at different conditions based on the design of the experiments [1]. Some chemicals are used to activate lignocellulosic materials which include  $H_3PO_4$  and  $ZnCl_2$ . Strong bases like  $KOH$  and  $NaOH$  are used in the activation of coal precursors and chars [29]. However, the chemical method has a limitation with some chemicals like  $ZnCl_2$  because of environmental contamination which includes corrosion and lack of chemical recovery methods. Impregnated  $KOH$  precursors yield large micro-porosity because it intercalates with the carbon matrix [31]. The chemical method provides several merits to the precursor which may include the use of single-stage activation, working at low-temperature ranges, short holding working time, higher porous structure, and high yield [1].

The chemical characterization of AC is mostly determined by the ability of the surface to obtain heteroatoms. This forms functional groups and delocalization around the structure which

primarily identifies the acidic or basic character of the AC at the surface [1]. AC has reducing capability because of the functional groups of oxygen such as phenolic, lactone, carboxyl, and quinone [1] Different carbonaceous electrode materials are used in supercapacitors (SC) because of high surface area, porosity, and surface functional groups. Materials such as AC [1], [32] carbon composites, metal carbide-derived carbon, Graphene and its derivatives, Carbon aerogels [33], [34] among others. The charge storage of electrochemical double-layer supercapacitors (EDLS) is based on interfacial layers formation of the electrode surfaces. This makes the surface area of materials for electrodes very important in SC application [32], [35]. AC-derived materials are highly levelled to have higher porosity, high surface area, high chemical, and physical stability, and high packing density [36], [37] Commercially available ACs are synthesized from different biomass due to their low cost of production and environmental friendliness. The porous nature of AC material is advantageous in SC application with microporous and microporous being more influential for charge transfer in the performance. The macropores also facilitate the transport zone with the structure of carbon materials. The high capacitance values are primarily due to the surface area of the material and the stability of electrolytes [1] Liquid phase oxidation method of treatment is known in introducing oxygen and its functional groups onto the surface of activated carbon (AC) at lower temperatures of operation compared to other methods of gas phase [30]

AC is highly on-demand as materials for the fabrication of the SC electrodes. These have high specific surface area (SSA), low cost and availability make them widely preferred active materials for electrodes. In the synthesis, the carbonization process aids the production of amorphous carbon and the thermal chemical conversion of the precursors. The activation process leads to the manipulation of SSA. This is reached by partial controlled oxidation of carbon

precursors gained either by chemical or physical activation [6]. The theoretical SSA of AC is about  $3000 \text{ m}^2/\text{g}$  although literature reports a usable SSA range of 1000 to  $2000 \text{ m}^2/\text{g}$  [38]. The most commercially available have a working potential of 2.7V when employing AC as an electrode material and specific capacitance range of 100 to  $120 \text{ F/g}$  [39] and a volumetric capacitance up to  $660 \text{ F/cm}^3$  [6] and the specific capacitance of  $300 \text{ F/g}$  [1]. These two processes result in activated carbon with theoretical surface area ( $3000 \text{ m}^2/\text{g}$ ) and pore size distribution in a wide range of macro-pores, mesopores, and micropores ( $>50\text{--}2 \text{ nm}$ ) [7] The micropores are in general considered to be inaccessible for electrolyte ions thus not capable of supporting an electrical double layer. The mesopores have maximum contribution towards capacitance in an electrical double layer capacitor followed by micropores [9] EDLC and pseudocapacitance both are surface phenomena, thereby, activated carbon with a high surface area is the perfect candidate for application as electrode material [4]. Though, the experimental value of capacitance for activated carbon-based supercapacitor was found to be in the range 1 to  $10 \mu\text{F/cm}^2$  which is lower than the theoretical calculations. This has been explained in detail by W. Li et al. [1], [40] and found that the surface area of the electrode material is not the only factor that determines the performance of the electrode. Several parameters need to be considered for calculating capacitance for instance; shape, structure, and size distribution of the pores along with the electrical conductivity and wettability of electrode in the particular electrolyte [1]. This creates new phenomena for use of mesoporous carbon (pore size 2 to 50 nm) for supercapacitor applications, which contributes to easy ion-transport over the conventional activated carbon and hence, demonstrates high power capability [40][14] synthesized mesoporous carbon by carbonizing a mixture of polyvinyl alcohol and inorganic salt and showed a specific capacitance of about  $180 \text{ F/g}$  in aqueous  $\text{H}_2\text{SO}_4$  electrolyte. The performance of mesoporous carbons can be

further enhanced by the controlled introduction of micropores. [1] showed that a specific balance between mesopores to micropores ratio can tune the specific capacitance to 223 F/g in 6 M KOH electrolyte at 2 mV/s scan rate with 73% retention cyclability. This improved capacitance has been attributed to the presence of hierarchical porous structure of the electrode material that consists of interconnected micropores and mesopores, having a high surface area of 2749 m<sup>2</sup>/g, and large pore volume of 2.09 cm<sup>3</sup>/g. The interconnected porous structure facilitates the easy movement of ions. The performance of mesoporous carbon can also be improved by its functionalization. The functionalized mesoporous carbon can then act as an efficient pseudo-capacitor electrode in addition to EDLC.

Different functional groups like —OH, —COOH or —C=O can be easily introduced by activating the mesoporous carbon using strong acids like nitric acid, sulfuric acid or ammonium persulfate. Jia et al. [1] pyrolyzed the mixture of milk powder and sodium hydroxide without any substrate resulting in the formation of N-doped mesoporous carbon which showed a high capacitance of 396.5 F/g at 0.2 A/g in the electrolyte solution of H<sub>2</sub>SO<sub>4</sub> along with high stability in their capacitance of 95.9% for capacitance retention after 2000 cycles at 50 mV/s. [1] have also observed that the capacitance of mesoporous carbon increased from 117 to 295 F/g (10 mV/s scan rate) after its treatment with nitric acid.

(Dubey and Guruviah, [6] obtained AC by carbonization of waste of fibreboards at 500 °C and activated with KOH at 800 °C varying the ratio of KOH/cake mass. This resulted in an SSA range of 1456 to 1647m<sup>2</sup>/g giving a specific capacitance range of 212 F/g to 223 F/g. AC materials electrodes properties like low cost and electrical conductivity are hindered by the low effective SSA caused by randomly connected micropores with sizes less than 2 nm which are hardly accessible by electrolytic ions (Z. Yang et al., 2015). To address that challenge, the

prepared mesoporous carbon of pore diameter ranging from 2 to 50 nm with high SSA was used as an SC electrode. This was to facilitate a fast ion-transport pathway and high-power density. The AC material exhibited a specific capacitance of 180 F/g in aqueous H<sub>2</sub>SO<sub>4</sub> as electrolyte [1]. The volumetric specific capacitance, power density, and energy density of mesoporous AC electrodes could be influenced directly by content and population between micropores and mesopores are required for electrochemical energy storage efficiency [11].

### 2.5.1. Controlling of shape and size in mesoporous carbon

The control of the shape and size of the mesoporous carbon material can be done through different synthetic techniques. The material can be produced as an ordered mesoporous carbon with homogeneously balanced pores of regular size. This can facilitate ion-transportation and charge storage hence improving capacitance and rate capability. The literature reported highly ordered sizes of 2.8nm and 8nm which were synthesized by SBA-16 silica with mesostructured templates and polyfurfuryl alcohol as the source of carbon [40]. The two types of sized materials reported an SSA of 1880 and 1510 m<sup>2</sup>/g respectively and a specific capacitance of 205 F/g for the 2.8 nm diameter as the highest capacitance. The mesoporous carbon can also be manipulated to introduce micropores in the materials. [1] reported activation of mesoporous carbon with CO<sub>2</sub> at 950 °C which imparted micropores in the mesoporous carbon and improved the specific capacitance from 115 F/g to 225 F/g in 6M KOH. This improvement of the specific capacitance can be attributed to the formation of hierarchical pores with SSA of 2749 m<sup>2</sup>/g and balanced mesopores and micropores.

The synthesis of mesoporous carbon materials using carbonization of non-conventional materials such as biomass is being adopted more and more as shown in Table 2.2. [1] reported production of N-doped mesoporous carbon materials by a one-step pyrolysis method using a mixture of

KOH and milk powder without any template. The produced materials exhibited an SSA of 2145.5 m<sup>2</sup>/g and pore volume of 1.25 cm<sup>3</sup>/g resulting in a specific capacitance of 396.5 F/g at 0.2 A/g in 6 M H<sub>2</sub>SO<sub>4</sub> giving capacitance retention of 95.9 % after 2000 cycles at 50 mV/s. the structure of pores and the shape of the mesoporous can be also further explored to improve the electrochemical performance. A composite of AC with graphene exhibited high SSA with improved specific capacitance. [1] reported a composite of graphene-AC porous materials with SSA of 3290 m<sup>2</sup>/g with the specific capacitance of 174 F/g, the volumetric capacitance of 100 F/cm<sup>3</sup> resulting in the energy density of 74 Wh/kg and power density of 333 kW/kg.

Table 2.2: Carbon-based EDLC as electrode materials [1]

<b>Electrode</b>	<b>Electrolyte</b>	<b>Specific capacitance (F/G)</b>	<b>Current density (A/g)</b>	<b>Retention cycles</b>	<b>References</b>
N-doped mesoporous carbon	-	288	0.1	25000	(JG Wang, Liu, H Sun, et al., 2018)
N-doped micro-mesoporous carbon	6M KOH	226	1.0	2000	(A. Chen et al., 2016)
N-doped mesoporous carbon	Ionic liquid	186	2.5	-	(D. Liu et al., 2016)
Layered N-doped mesoporous carbon	0.5M H <sub>2</sub> SO <sub>4</sub>	810	1.0	5000	(T. Lin et al., 2015)
	2M Li <sub>2</sub> SO <sub>4</sub>	710	1.0	5000	
N-doped mesoporous carbon	Ionic liquid	225	0.5	1000	(M. Xie et al., 2014)
Hierarchically N-doped mesoporous carbon	0.5M H <sub>2</sub> SO <sub>4</sub>	537	0.5	10000	(Han et al., 2016)

Incorporation of heteroatoms such as nitrogen, boron, phosphorous, and sulfur (N, B, P, and S) into the carbon network by replacing some carbon atoms offers a significant change in the electronic, electrical, and surface charges properties of the carbon materials. Doping of heteroatom in carbon materials can be done either by in situ preparation of carbon or through post-treatment by heteroatom containing precursor [7]. In particular, nitrogen doping has gained more attention in a supercapacitor, because nitrogen doping not only improves the electrical conductivity and wettability but also contribute additional pseudocapacitance by enhancing the surface polarity and electron donor affinity of carbon. Kigozi [1] stated that from the studies made by Wang et al, nitrogen doping facilitates the formation of well-defined mesopores and resulted in improved electrochemical performance. Also he stated [1] that Lin et al. developed N-doped mesoporous few-layer carbon with a large surface area of  $1900 \text{ m}^2/\text{g}$  for supercapacitor. It was reported that the as-developed few-layer carbon showed the highest ever specific capacitance of  $810 \text{ F/g}$  in a three-electrode cell and  $710 \text{ F/g}$  in a full cell at  $1 \text{ A/g}$  in  $0.5\text{M H}_2\text{SO}_4$  and  $2\text{M Li}_2\text{SO}_4$  electrolytes. The full cell device showed high stability with 50,000 repeating cycles between 0 to 1.2 V and demonstrated the highest specific energy of  $23.0 \text{ Wh/kg}$  while maintaining the specific power density of  $18.5 \text{ kW/kg}$  in  $2\text{M Li}_2\text{SO}_4$  electrolyte. Though the exact mechanism has not yet been confirmed it is evident that the pyrrolic N, pyridinic N, or quaternary N plays a crucial role in determining the ion flow towards the electrode, hence, influencing the capacitance of the electrode (A. Chen et al., 2016). Nitrogen and phosphorus dual doped mesoporous carbon was also prepared, which reveals a high specific capacitance of  $220 \text{ F/g}$  at a current density of  $1 \text{ A/g}$  with an excellent rate capability of 91% in a  $6 \text{ M KOH}$  aqueous electrolyte [1]. This value of capacitance was found lower than nitrogen and sulfur or nitrogen and oxygen dual doped mesoporous carbon synthesized using polyhedral oligosilsesquioxanes,

which showed an almost rectangular cyclic voltammogram curve in a wide potential window from  $-2$  to  $+2$  V in an ionic liquid electrolyte. These electrode materials showed a gravimetric and volumetric specific capacitance of 163 F/g and  $106 \text{ F cm}^{-3}$  at a current density of 0.25 A/g [1]. Another form of activated mesoporous carbon is carbon nanofibers. The ease of preparation and highly mesoporous structure of these fibers exhibited excellent electrode material for electrochemical double-layer capacitors. [1] prepared polyacrylonitrile fibers followed by NaOH activation, and observed high specific capacitance of 371 F/g in the aqueous KOH (6 M), 213 F/g in non-aqueous  $\text{LiClO}_4$  (1 M), and 188 F/g in ionic liquid electrolyte solutions. Mesoporous carbons have also been extensively studied in the form of composites with other active materials, including conductive polymers (polyaniline, poly-3-hexylthiophene) and metal oxides (Manganese oxide  $\text{MnO}_2$ , Ruthenium oxide  $\text{RuO}_2$  [7]) In particular, pristine conducting polymers with their excellent electrochemical properties have displayed capacitance 10–100 times higher than EDLCs but they suffer from some limitations like poor stability and short lifetime. Thus, combining the properties of conducting polymers with mesoporous carbon can result in an electrode material with optimum properties. For instance, chemical polymerization of polyaniline onto an ordered bi-modal-mesoporous carbon resulted in the formation of PANI nanowires growing out of mesoporous carbon substrate has been reported by [1]. The subsequent composite exhibited a specific capacitance of 517 F/g in 1M  $\text{H}_2\text{SO}_4$  electrolyte with a 91.5% retention rate after 1000 cycles. Chen et al. have presented a facile synthesis of highly porous N-doped carbon nanofibers coated with polypyrrole by carbonization which showed a specific capacitance of 202 F/g in aqueous KOH (6M) electrolyte at a current density of 1 A/g. It displayed a maximum power density of 90 kW/kg while maintaining high capacitance retention and cyclability. This

kind of N-doped carbon nanofiber-based composites exemplifies unconventional and practically potential candidates for a competent electrode material for supercapacitors [1].

## 2.6. Synthesis approach for electrode materials

The method of synthesis of electrode materials plays an important role in controlling the structures and properties of the materials, different synthesis methods are described briefly:

### 2.6.1. Sol-gel method

Sol-gel is a facile method to prepare materials with greater purity and homogeneity. The sol-gel method is so named, as in its micro-particles in the solution (sol) agglomerate and link together in regulated conditions to form an integrated network (gel). Two basic variations of the sol-gel method are the colloidal method and the polymeric or the alkoxide method, which are different from each other depending on the type of precursors used. In both methods, the precursor is mixed in a liquid (usually water is used for the colloidal method and alcohol for the polymeric method) and is then activated with the addition of an acid or a base. Then, as obtained, the activated precursor reacts forming a network, which develops with temperature and time maximally up to the container size [41]. Many TMOs have been prepared by this method. This process provides the advantage of preparing materials for different morphologies. The electrode material prepared by this process possesses high SSA with better electrochemical behaviour which can also be controlled by temperature, change of surfactants, solvents, and reaction time. [1] reported this method for the production of activated carbon fiber material (ACFM)-Ni(OH)<sub>2</sub> composite which exhibits the specific capacitance of appx 370–380 F/g. Also, the dependence of shape, structure, and volume of material on the composition and concentration of the solution was established. [1] due to deposition of NiCo<sub>2</sub>O<sub>4</sub> films by a sol-gel method which exhibit the specific capacitance of 2157 F/g at a 0.133 mA/cm<sup>2</sup> current density and good cycling stability

(96.5% specific capacitance retained after 10,000 cycles). NiO/LaNiO<sub>3</sub> electrode fabricated by spin-coating on Pt/Ti/SiO<sub>2</sub>/Si (100) substrate showed a specific capacitance of 2030 F/g at a 0.5 A/g and high stability (83% of the specific capacitance retention after 1000 cycles). This superior electrochemical response can be related to high porosity, well-connected network structures with reduced mass transfer resistance between electrolyte and ion which facilitates electron hopping in nanoparticles.

### 2.6.2. Electro-polymerization / Electrodeposition

This is a common synthesis technique that provides precise regulation over the thickness of films and on the rate of polymerization. By suitable choice of deposition solution, nanostructured films with different mass loading and morphologies can be prepared by this method. This technique involves simple processing conditions and not many toxic chemicals are used in it. It is generally used for preparing CPs such as PANI, PEDOT, PPy, among others. [1] prepared MnO<sub>2</sub>-PEDOT:PSS composite by a co-electrodeposition strategy which exhibits an areal specific capacitance of 1670mF/cm<sup>2</sup> at 0.5 mA/cm<sup>2</sup> and excellent mechanical robustness. Nano sized MnO<sub>2</sub> electrodes on Au nanowire stems are grown electrochemically by Chen et al. [4] which exhibit high specific capacitance (1130 F/g at 2 mV/s), high energy density (15 Wh/kg at 50 A/g), high power density (20 kW/kg at 50 A/g) and long-term stability (90% of specific capacitance left after 5000 cycles). ZnO@Ni<sub>3</sub>S<sub>2</sub> core-shell nanorods are formed by the electrodeposition method by [1] which exhibit a specific capacitance of 1529 F/g at 2 A/g and retain 42% of initial specific capacitance after 2000 cycles. Stretchable CNT-PPy films are deposited by electrochemical deposition by Guo et al [42]

### 2.6.3. In-situ polymerization

In this process, monomers are dispersed into an aqueous solution using the sonication process. Then an oxidizing agent is mixed to initialize the polymerization in the aqueous solution and the sample is obtained by filtering the solution. Earlier this method yielded only irregular aggregates with a little portion of nanofibers, but with slight modification, nanoparticles, nanorods, and nanofibers were reported with better solution processability and better physical and chemical properties. A simple strategy for the growth of PEDOT structures on carbon fiber cloth (CFC) by in situ polymerization is reported [43]. When a supercapacitor device is fabricated with these nanostructures, it exhibits a specific capacitance of 203 F/g at 5 mV/s, an energy density of 4.4 Wh/kg, and a power density of 40.25 kW/kg in 1M H<sub>2</sub>SO<sub>4</sub> electrolyte. Also, it possesses 86% specific capacitance retention after 12,000 cycles. It was reported that Wang et al [1] deposited PANI nanowires within the multi-walled carbon nanotubes (MWCNTs) by in situ electro-polymerization. The aligned MWCNTs provide support to the organic polymers along with providing a pathway for the transfer of charge. Also, confined MWCNT channels limit the structural changes in PANI chains while charging-discharging and enhance the lifetime of the structure. The films made with porous carbon encapsulated in MWCNTs showed a specific capacitance of 296 F/g at 1.6 A/g. Different  $\pi$ -conjugated sulfonate templates and additional assistance of graphene and MWCNTs are employed to enquire about the polymerization behaviour of PEDOT by Zhou et al.as reported by Kigozi [1]. As prepared PEDOT: MWCNT composite reveals an interconnected network due to the  $\pi$ - $\pi$  interaction of PEDOT with non-covalent functionalized MWCNT and exhibits a specific capacitance of 199 F/g at 0.5 A/g.

#### 2.6.4. Direct coating

This technique is employed for the fabrication of those SC electrodes in which active material, in the form of a slurry, is applied directly on the substrate. Often, additives such as carbon black, polyvinylidene fluoride (PVDF), acetylene black, polytetrafluoroethylene (PTFE) are introduced as binders to provide maximum adhesion along with retaining electrical conductivity. The working electrode is fabricated with 90 wt% electrode materials (NiO) and 10 wt% PVA in mills water as a solvent and the slurry obtained is pasted on the Pt disc. [1] prepared supercapacitor electrode slurry by mixing nitric acid-treated carbon cloth with 10% PVDF and DMF (N, N-dimethyl formamide) and the prepared slurry is coated on a stainless-steel substrate.[1] synthesized supercapacitor electrode by coating the slurry formed by adding active material with acetylene black and PTFE onto Ni foam.

#### 2.6.5. Chemical vapour deposition (CVD)

CVD technique is generally used where the porosity is very important. This process is performed under vapour phase, where the initial material is prepared in vapour form, flowed, and subjected to a high temperature (800 to 1000 °C). The as-prepared structures have even morphology [1] Among various synthesis methods of graphene, for instance, mechanical cleavage of graphite, chemical exfoliation of graphite (in organic solvents), manufacturing of multi-layered graphene by arc discharge, reduction of graphene oxide (GO) synthesized from the oxidation of graphite, graphene synthesized by CVD provides better results owing to their large crystal domains, monolayered structure and fewer defects in the sheets, which help enhance carrier mobility [1] demonstrated that high-efficiency SCs with improved electrochemical characteristics can be fabricated by CVD-grown graphene hybridized with MWCNTs. [44] prepared hybrid carbon

materials consisting of MWCNTs and graphitic layers, produced by CVD, over MgO assisted metal catalyst, such materials provide fast charge transport in the cell.

#### 2.6.6. Vacuum filtration technique

This quick and proficient technique uses the simple concept of vacuum filtration to prepare nanocomposites from a physical combination of different materials. Generally, a mixture of materials is prepared followed by simple vacuum filtration and drying of the filtrate. In this method, the composition can be simply altered by varying the concentration or the weight percentage of each constituent in the mixture. Graphene suspension, developed by vacuum filtration deposition [1] for fabricating graphene-based Ni foam electrodes, shows a higher  $E_d$  and Pd along with good cycling performance. [1] synthesized a nanocomposite of graphene/AC/PPy by vacuum filtration method. As prepared electrode exhibits the  $C_s$  of 178 F/g at  $0.5 \text{ mA/cm}^2$  and retains 64.4% of  $C_s$  after 5000 charge/ discharge cycles. [1] reported that this technique was used to prepare graphene/ polymer electrode on Ni foam in which the vacuum pressure and its duration controls the distribution of graphene.

#### 2.6.7. Hydrothermal/solvothermal method

The hydrothermal process can be ascribed as environment-friendly superheated aqueous solution dispensation. Also, this provides controlled diffusivity within a closed system. The process has superiority over other techniques as it is ideal for preparing designer particulates (particles with high purity, crystallinity, quality, and controlled chemical and physical characteristics). Also, this is a low-temperature sintering process with a small energy requirement which is simple to implement and scale up [1]. Though, this process has lesser control over nanoparticle aggregation. The solvent properties (i.e., dielectric constant, solubility) change radically in the supercritical phase. Thus, the supercritical phase gives a favourable condition for particle

formation owing to increased reaction rate and great supersaturation. If some other solvent is used instead of water, then the method is called solvothermal synthesis. A lot of SC electrodes have been fabricated using this process such as rod-like hollow  $\text{CoWO}_4/\text{Co}_{1-x}\text{S}$  Cobalt disulfide-reduced graphene oxide ( $\text{CoS}_2\text{-rGO}$ ) [45] hexagonal  $\text{NiCo}_2\text{O}_4$  nanoparticles [1].

#### 2.6.8. Co-precipitation method

This is a facile method for the large-scale production of powder samples. For precipitation to take place, the concentration of one solute should be more than the solubility limit and temperature should be high enough for fast separation into precipitates. Here, it is difficult to regulate the morphology of prepared samples due to the fast rate of precipitation. Various supercapacitor structures have been reported using this method such as  $\text{CoFe}_2\text{O}_4$ -magnetic nanoparticles with different precursors [1]  $\text{Ni}_3(\text{PO}_4)_2@\text{GO}$  composite [46] which displays a specific capacitance of 1329.59 F/g at a 0.5 A/g and 88% of the Cs retention after 1000 cycles.

#### 2.6.9. Dealloying method

The Dealloying method, also known as selective dissolution, is an easy, flexible and economical technique to produce nanoporous metallic materials (NPMs) with structures like core-shell, hollow core-shell, and porous nanoparticles [1] In this method, the more active material is removed from a solution of binary metallic solid by electrolytic dissolution thus producing an interconnected porous structure. Such structures possess higher surface area, good mechanical and compression strength along with size-scale dependent elastic modulus. Much attention has been given to NPMs prepared by this method since the important work of [1] and has become a very important method to produce NPMs in the last decade. They examined the fixed voltage dealloying of AgAu alloy particles in the size range of 2 to 6 nm and 20 to 55 nm. They demonstrated that only the core-shell structures (2 to 6 nm in diameter) evolved above the

potential corresponding to  $\text{Ag}^+/\text{Ag}$  equilibrium. CuS nanowire on a nanoplate network with improved electrochemical performance has been prepared by Wang et al. as reported by Kigozi [1] using an improved dealloying method at two contrasting reaction temperatures.  $\text{Cu}_2\text{O}$  has been synthesized by oxidation assisted dealloying method [1] The free-dealloying method has been used for the synthesis of Cu-based metallic glasses in HF and HCl solutions [1] reported a green and universal technique (vapour phase dealloying) for fabricating porous materials by using vapour pressure among constituent elements in an alloy, to selectively eliminate a component with high vapour pressure, for producing 3-dimensional bi-continuous open nanoporosity. With this technique, extensive elements can be fabricated with tunable pore sizes along with full recovery of the evaporated component. Flexible electrodes of  $\text{Co}_3\text{O}_4$  flakes and  $\gamma\text{-Fe}_2\text{O}_3$  nanoparticles have been prepared by oxidation-assisted dealloying method for the first time by Wang et al as reported by Kigozi [1].

#### 2.6.10. Other synthesis methods

There are other synthesis methods which have been reported for SC electrodes. One of the methods that has been used is the microwave for the rapid synthesis of tin selenide [1] Nitrogen functionalized carbon nanofibers (N-CNFs) are prepared by carbonizing PPy-coated nanofibers (NFs), which in turn are obtained by ‘electrospinning’ and deacetylation of electrospun cellulose acetate NFs and PPy polymerization [1]. An additive-free, cost-effective, and scalable ‘successive ionic layer adsorption and reaction (SILAR) method’ has been quoted to prepare Ni-Co binary hydroxide on RGO [1] The pulsed layer deposition method is used to fabricate NiO on graphene foam [1]. Free-standing 3D porous RGO and PANI hybrid foam has been fabricated by ‘dipping and dry method. Hierarchical porous carbon microtubes have been synthesized by carbonization along with KOH activation.

## 2.7. Concept of supercapacitor technology

Based on the charge accumulation process, a supercapacitor is mainly divided into a dual-layer capacitor and a pseudocapacitor. The dual-layer capacitor is a capacitive-type (non-Faradic) supercapacitor because when it is charged; there will be a combination of positive and negative charges at each electrode. The combinations are separated by the electrolyte. In the case of pseudocapacitor, the chemical reactions are occurred within the active materials of the electrodes according to Faraday's laws. Consequently, the amount of the stored charge is related to the type of the active materials and the potential of the electrodes [47].

### 2.7.1. Cell Construction

A supercapacitor has similarity with conventional capacitor; however, the major difference of a supercapacitor from the conventional capacitor is that its electrode material is based on carbon. It is made up of two electrodes immersed in the electrolyte and separated by a separator [47].

### 2.7.2. Electrode

The electrodes are made of conductive metal current collector coated by activated carbon rough powder providing a large specific surface area and small distance of about 10 Å. The carbon powder is pressurized to increase conductivity and decrease the contact resistance between the powder and the metal collector. Since the capacitance of any capacitor is proportional to the area and inversely proportional to the distance, the carbon powder provides the area of an electrode up to 3000 m<sup>2</sup>/g and hence maximizing the number of electrolyte ions absorbed and so is the capacitance which increases linearly up to 250 F/g [34].

### 2.7.3. Electrolyte

Supercapacitor electrolyte is a chemical liquid containing ions or a source of ions (charges). When applying a voltage to the electrodes the electrical potential draws the ions into the activated carbon so that positively charged ions will be attracted to the negative electrode and the negatively charged ions are attracted to the positive electrode. The accumulation of the ions on both electrodes will form double layers inside activated carbon pores. The diameter of the ions and the size of activated carbon pores determine the double-layer phenomena and hence the capacitance. Because the activated carbon is an extremely pored material therefore, a very large number of ions can be absorbed into the electrodes of the capacitor resulting in high capacitance [47]. Two types of electrolyte are used; aqueous and non-aqueous electrolyte (organic) which can classify the supercapacitor as following:

**Aqueous electrolyte:** Aqueous electrolyte based on sulphuric acid or potassium hydroxide. Their ions diameter is relatively small which allows higher ions absorption by the activated carbon pores and therefore, lower internal resistance. This leads to limiting the insulating ability of the electrolyte which on the other hand limits the cell voltage. The typical cell voltage is 1.23 V [47].

**Organic electrolyte:** Non-aqueous electrolyte is quaternary salts dissolved in an organic solvent. Unlike the aqueous electrolyte, organic ions have a bigger diameter which limits the ions' penetration or absorption into the activated carbon pores. The internal resistance of organic electrolyte is a bit high compared to the aqueous electrolyte internal resistance resulting in providing a high voltage range of 3 to 3.5 V [47]. The type of electrolyte used in the supercapacitor may be associated with determining the energy density and power density of the supercapacitor due to the role of the cell voltage range and the internal resistance. As stated, the

aqueous electrolyte has a lower voltage range than the organic electrolyte. Equation (2.2) illustrates that the cell voltage determines the stored energy [48].

$$E = \frac{1}{2}CV^2 \quad \dots\dots\dots(2.1)$$

Where E is the energy, C is the capacitance and V is the cell voltage

In contrast, the organic electrolyte has higher internal resistance than the aqueous electrolyte by a factor of four as shown in Eqn (2.2) [48]

$$P = \frac{V^2}{4(ESR)} \quad \dots\dots\dots(2.2)$$

Where P is the power and ESR is the internal resistance.

It can be seen from Eqn (2.1) and (2.2) that aqueous electrolyte has a lower energy density than the organic electrolyte due to its low voltage, but on the other hand, has higher power density than the organic electrolyte due to its low internal resistance.

#### 2.7.4. Separator

A separator is a barrier used as a spacer between the electrodes to prevent electrodes short circuit. It blocks any electronic contact (short circuit) in the cell, but on the other hand, it allows ionic transfer between electrodes. The separator comes in a form of polymer, in case of organic electrolyte is used, and glass fiber or ceramic in case of aqueous electrolyte [47].

#### 2.8. Characteristics of supercapacitors

The supercapacitor has a series of characteristics that influence and determine its performance. These factors are the capacitance, rated voltage, power and energy densities, and finally its charge and discharge behaviours over time. Supercapacitors have the advantages of high-power

density, safety, a broad range of operating temperatures, and superfast charge times. The charging time for a supercapacitor generally ranges from a few seconds to minutes, and the typical cycling life can reach 100,000 cycles with only a slight performance degradation. [1] These aforementioned technological features allowed supercapacitors to become the next generation of energy storage devices. However, they still have low energy densities. The energy density of standard supercapacitor devices is limited to 10's of Wh /kg. Thus, supercapacitors are also used as EV starters and cabin door switchers for airplanes, which require a high-power density and a short discharge time. The first advantage of using supercapacitors as EV power suppliers is their long cycling life, which is superior to the lifetime of LIBs, which is generally 2,000 times, or 5–6 years if the device is charged once daily [1]. Furthermore, supercapacitors have a rapid charging time of several minutes or less, which is much less than the time required to fill oil. For example, the bottleneck is the running distance (energy density), which should be at least 100 km for use in EVs. Thus, the energy density must also be greater than 100 W h/kg. In this case, the mileage goes to infinity with negligible charging times. EV mobility can be greatly enhanced using supercapacitors whose performance is competitive with LIBs.

### 2.8.1. Supercapacitor Capacitance

Due to its large surface area of the electrodes and to the very small distance, supercapacitors have a very large capacitance reaching thousands of Farads compared to the conventional capacitor whose capacitances range from 1  $\mu$ F up to 1 F. The capacitance is determined from Eqn (2.4) [48].

$$C = \epsilon_d^A \text{ Farads} \dots\dots\dots(2.3)$$

Where  $\epsilon$  is the dielectric constant, A is the geometric area and d is the distance between the formed layers.

Considering Eqn (2.3), if the area is in the range of thousands of square meters and the distance of the range of nanometers, the capacitance, according to the equation, will be in the range of the thousands of Farads. The capacitance is also determined by Eqn (2.4), as the capacitance can be defined as the ratio of the stored charge to the applied voltage [48].

$$C = \frac{Q}{V} \quad \text{Farads} \quad (2.4)$$

### 2.8.2. Supercapacitor Rated Voltage

In general, the supercapacitor has a lower rated voltage (1.23 to 3.5 V) due to the limit of breakdown potential of the electrolyte, however; the supercapacitor cells can be connected in series to form a module to meet the desired high voltage. Although this arrangement would provide a rated voltage to meet a certain required voltage, it affects the total capacitance of the module as the capacitance of several capacitors connected in series will reduce the total capacitance of the module and hence the stored charge. Equation (2.6) illustrates the reduction in overall capacitance [6].

$$\frac{1}{C_{Total}} = \frac{1}{C_1} + \frac{1}{C_2} + \frac{1}{C_3} + \frac{1}{C_4} + \dots + \frac{1}{C_n} \dots\dots\dots(2.5)$$

Where  $C_{Total}$  is the overall capacitance of the module and "n" is the number of capacitors connected in series. On the other hand, several supercapacitors can be arranged together to achieve specific requirements in terms of capacitance, voltage, current, energy density, and power density. Consequently, there are three arrangement methods such as series, parallel, or a combination of them.

Commercially, the rated voltage is on the order of 2.5 V to 2.7 V while the capacitance reaches a few thousand Farads. Due to their low voltage levels, supercapacitors need to be connected in series so as to obtain the required voltage levels, reaching a few hundreds of volts. However, the total capacitance and stored energy are reduced. The main disadvantage of this arrangement is that the total voltage over the whole series string of the supercapacitors may not be symmetrically shared between the individual supercapacitors based on the variations between their parameters. If the terminal voltage of any supercapacitor increases more than its rated voltage, this supercapacitor may be damaged. The solution to this problem is to equalize the total voltage between the different supercapacitors by using high-efficiency power electronics [10]. To increase the capacitance as well as the energy and power densities, the supercapacitors need to be connected in parallel. Also, the total current which can be delivered increases corresponding to the number of supercapacitors and vice versa. However, this current may be equally shared or not between the supercapacitors depending upon the percentage of the difference between their parameters. From the previous two methods, not all requirements are achieved because when the total voltage needs to be increased, the capacitance cannot be and vice versa. By connecting the supercapacitors in a series-parallel arrangement, the required capacitance and total voltage can be achieved but this arrangement needs an equalization circuit to be added [47].

### 2.8.3. Supercapacitor Internal Resistance

The internal resistance of supercapacitor is represented by equivalent series resistance (ESR) and equivalent parallel resistances (EPR) are as follows [10]

### **2.8.3.1. Equivalent series resistance (ESR)**

The internal resistance of the supercapacitor is the sum of its component's resistivity such as electrodes, electrolyte, and any external circuit involved such as wire resistance as well as the ion size that is absorbed by pores. It is known as equivalent series resistance (ESR). It determines the voltage during the discharge and the amount of power that can be delivered by the supercapacitor, the lower the ESR the higher power. This leads to the fact that supercapacitor efficiency is a function of these series resistances.

### **2.8.3.2. Equivalent parallel resistance (EPR)**

Supercapacitor storage performance decays over time as it has a short-term energy performance. This is due to leakage current or self-discharge. This leakage current is modelled as a parallel resistor connected in parallel with the supercapacitor. It is called the Equivalent parallel resistance (EPR). It increases proportionally with temperature. Consequently, as the EPR increases the leakage decreases increasing long-term energy [10].

### **2.8.4. Temperature**

The supercapacitor performance remains unaffected over a wide range of temperatures. Unlike a lead-acid battery, there is no chemical reaction taking place in the charge and discharge process which gives the supercapacitor a lead of the lead-acid battery. The supercapacitor can operate without effect within a temperature range of +70 Co down to -20 Co. However, the conductivity of the organic electrolyte will be affected and hence limiting the performance of the supercapacitor [16].

### **2.8.5. Supercapacitor Energy and Power Densities**

Energy and power densities are factors that are shared between batteries, conventional capacitors, and supercapacitors. In the case of batteries, the ability to store energy is very high but the speed of delivering that energy is very poor, in other words, batteries have high energy density but low power density. However, in the case of a conventional capacitor, the capability of delivering power is very high but the ability to store energy is very poor. This gap between the batteries and conventional capacitor energy and power densities are filled in by supercapacitor [47].

### **2.8.6. Charging/Discharging Supercapacitor**

A supercapacitor is the same as the conventional capacitor and unlike the battery when it comes to charge and discharge behaviors. It charges rapidly and exponentially and discharges in the same minor of charging over a short time [1] The charging time is only limited by the RC circuit. As the supercapacitor is made of several series RC circuits, therefore, the charging time is depending on the value of the RC circuit. Moreover, and unlike the batteries the charging and discharging cycle is considered unlimited as no chemical reaction takes place throughout the process [47].

## **2.9. Applications of supercapacitors**

Supercapacitors found its way into many industrial aspects from power systems to standby and automotive systems both fossil and electric vehicles. It is also used in telecommunications and digital cameras. The following is a brief description of the supercapacitor used in some applications [47].

Transmission lines: Due to variation in power demand a storage device becomes necessary. As a matter of fact, a storage device is the heart of FACTS devices, the supercapacitor is used in these FACTS devices to improve power transfer and enhance power quality and provide stability in voltage and frequency.

UPS: In this application, the supercapacitor is combined with the storage batteries to provide power over a short period of interruption so that the batteries are only delivering their energy over a long period of interruption which, consequently, extends the battery's life.

Telecommunications: The need for fast response backup systems during the lack of the main power source in this field is a very important issue to get high reliable operation and avoid interruption of the communication system. This requires a sort of backup batteries, UPS or other sorts of what it is called Hot Standby System, however, this system has an issue of power consumption which means high cost. However, a supercapacitor can act very fast as a cold standby unit and dissipate almost no energy.

Cold starting of diesel-fuelled engine: Diesel fuelled engines are quite hard to start-up in cold weather where the lubrication oil temperature drops below 0 degrees making an increase in the viscous friction which requires high cranking torque to start the engine. This cranking torque requires a high current from the lead-acid battery which is also affected by the cold weather as its internal resistance increases as the temperature drops, which limits the discharge current and hence reduces the ability to sustain the cranking current during engine start. This issue is overcome by using a bank of a supercapacitor as it does not get affected by low temperature so that the cranking current surge is provided by the supercapacitor.

Hybrid electric vehicle: The hybrid electric vehicle operation involves transient power demand due to acceleration and deceleration which require storage devices with high power density along with high energy density. As the hybrid electric vehicle was driven by a bank of batteries, which are known for low power density and high energy density, the battery life will be affected, however, by combining the supercapacitor with the battery, the transient current will be supplied by the supercapacitor resulting in battery life being extended [47].

### **2.9.1. Advantages and Limitations of Supercapacitors**

The advantages are as follows: [1]

1. Unlike batteries, supercapacitors have virtually unlimited cycle life because they can be deep cycled up to a wide range of times, reaching thousands (about 500000 times).
2. Due to their low impedance compared to batteries, supercapacitors can enhance high pluses of energy without lifetime deterioration. Furthermore, within a very small period (a few seconds), fast charging can be achieved.
3. Supercapacitors have about 100 times higher specific power density than batteries.
4. If they are overcharged, nothing dangerous happens but the lifetime may affect them. Also, there is no need for an overcharge detection circuit because, within their rated voltage, it can be charged up to any voltage.
5. In terms of temperature, supercapacitors can be operated and stored in a range of (-40° to 70° Co) with relatively small changes to the parameters.
6. Maintenance-free, friendly to the environment, and completely pollution-free.
7. Explosion risk is minimal

### 2.9.2. The limitations are as follows:

a) The energy density is low and it is of an order of one-fifth to one-tenth the energy of batteries.

b) For batteries, supercapacitors have a high self-discharge rate.

c) The EDLC cells can withstand a low voltage of about 2.7 V. In the case of high voltage applications, several cells must be connected in series according to the amount of rated voltage required. However, they cannot be directly connected because the terminal voltage of each cell may differ from the other cells. Consequently, damage to cells that have terminal voltages higher than their voltage ratings. Mainly, this is due to their capacitances not the same causing supercapacitors with smaller capacitances to have higher terminal voltages.

d) Due to may not be possible to use the full stored energy depending upon the application, because, during discharging, the terminal voltage decreases exponentially.

### 2.10 Mechanical Performance of Solid State Electrolytes

There is a growing concern in the use of liquid electrolyte for energy storage systems due to its hazardous effects especially as a result of leakages, combustion tendencies, weight etc. hence the recent research on solid state electrolyte of which polymer plays a major role . Some of the polymers used are PVA, PVP, PEO etc. there are available, non-toxic and renewable nature which is environmentally friendly, low cost, mechanical strength and establishes a good contact between the electrolyte interfaces and the electrodes.[49]–[53] It is to this end that the mechanical behaviour of solid polymer electrolyte vis-à-vis the electrochemical performance is being studied [52], [54]. Some of the mechanical properties studied includes Young's modulus, hardness, tensile strength, fracture toughness, thermal stability etc. Young's modulus ( $E$ ) is use to

determine the solid's stiffness or resistance to elastic deformation under loading condition. It tells us the relationship between stress (force per unit area) to strain (proportional deformation) along an axis. The fundamental principle is due to the fact that a material undergoes elastic deformation when it is compressed or extended with a tendency to reverse to its original shape at the removal of the load. More deformation occurs in a flexible material compared to that of a stiff material. Which means:

- An elastic solid material will result to low Young's modulus
- An inelastic solid material or material with high stiffness may result in high Young's modulus.

$$E = \frac{\sigma}{\epsilon} = \frac{\frac{F}{A}}{\frac{\Delta L}{L_0}} \dots\dots\dots(2.6)$$

where E is Young's modulus, usually expressed in Pascal (Pa),  $\sigma$  is the uniaxial stress,  $\epsilon$  is the strain, F is the force of compression or extension, A is the cross-sectional surface area or the cross-section perpendicular to the applied force,  $L_0$  is the original length and  $\Delta L$  is the change in length.

Hardness can be defined as the ability of a material to resist deformation. It is the measure of maximum energy a material can absorb before fracture can occur. Hardness is material property dependent on strain, toughness, strength, elastic stiffness, ductility, plasticity, viscosity etc. It is measured in Pascal (Pa).

For ultimate tensile strength which is also known as tensile strength, we define it as the maximum load which a material can support without fracture due to stretching when you divide by the material original cross-sectional area.

For polymeric material, Thermal stability is defined as its ability to resist the action of heat at a certain temperature while maintaining its properties (strength, toughness, or elasticity).

In considering a test specimen after breakage, then we say that the ratio of changed in length to its initial length is defined as elongation at break, which is also called fracture strain. It is that ability of a material like natural plant fibre to withstand changes of shape without cracking.

Therefore the mechanical performance of solid state electrolytes are very important as these will enable us to predict the behaviour of the material vis-à-vis the electrochemical performance over time in a way to develop a more robust energy storage system which no doubt will benefit manufacturers and end users.

### **2.10.1 Deformation of Solid State Electrolytes**

Deformation of materials deals with the changes in shape or size as a result of applied forces (tensile, compressive, bending, twisting, shear etc.) or variations in temperature resulting to phase transformation (thermodynamics and Kinetics). Sometimes, these forces can caused permanent deformation. There are different types of deformation like elastic deformation (the strain is reversible) plastic deformation (the strain is irreversible) and fracture deformation (this case result to crack initiation and propagation) The major causes of deformation of solid-state electrolyte are due to material defects such as surface cracks, subsurface pores, voids, and

pinholes [55]–[57] Another factor that can affect solid state electrolyte is thermal instability as a result of phase transformation as seen in Gibb’s free energy (G).

$$G = H - TS \dots\dots\dots (2.7)$$

Where H = Enthalpy (heat content), T = Absolute temperature and S= Entropy (Measure of randomness/disorder)

D. Golodnitsky et al. [58] carried out research on the structure and mechanism of ion conduction in polyethylene-oxide-based solid polymer electrolytes because of the assertion that the conductivity in polymer electrolytes is as a result its amorphous phase above the glass-transition temperature ( $T_g$ ) given effects to a more dynamic, disordered environment which played a critical role in enhancing ion transport capability. However, it has been observed that ionic conductivity can also be attributed to polymer electrolytes, in crystalline ion–polyether 1:6 complexes and polymer-in-salt electrolytes. These results have opened a new trend in the search for ion transport in solid polymer electrolytes and how deformation affects its performances

Hui-Chia Yu et al. [59] in their work evaluated the stress state and deformation of solid-state composite cathodes due to thermal contraction and cycling. They discovered differences during charge/discharge cycles in the thermal contraction/expansion and volume changes which led to internal stresses that ultimately caused degradation of solid-state composite cathodes and possesses obstacles in the realization of their practical applications. They also examined the effects of cathode thickness and selections of different cathode materials on the resulting residual stresses and deformations and found out that the (de)lithiation stresses during cycling are more than twice the thermal residual stresses after sintering. Furthermore, they also found out that the

maximum (de)lithiation and thermal residual stresses are sensitive to the cathode thickness only when the cathode-layer thickness is comparable to that of the electrolyte separator layer.

Yuki Kamikawa et al [60] “Elastic–Plastic Deformation of a Solid Electrolyte Interface Formed by Reduction of Fluoroethylene Carbonate: A Nanoindentation and Finite Element Analysis Study” stated that the evaluation of mechanical properties of a solid electrolyte interface (SEI) is critical to determine its stability on silicon anodes because of expansion during lithiation. They also employed cyclic loading tests and numerical methods for SEI to rate the elastoplasticity and viscoelasticity and the effects of stress field in the silicon anode. Davide Grazioli et al. [61] carried out a study on the effect of mechanical stresses arising in solid polymer electrolytes (SPEs) on the electrochemical performance of lithium-ion (Li-ion) solid-state batteries. They also used time-dependent finite element analyses of interdigitated plate cells during a discharge process with a constitutive model that couples ionic conduction within the SPE with its deformation field, as a result of the coupled nature of the processes taking place in the SPE, the non-uniform ionic concentration profiles that developed during the discharge process induced stresses and deformations within the SPE; at the same time the mechanical loads applied to the cell affect the charge conduction path. They reported that study of the parametric show that stresses induced by ionic redistribution favour ionic transport and enhance cell conductivity up to a 15% increase compared to the solution obtained with a purely electrochemical model. It was observed that, when the contribution of the mechanical stresses is included in the simulations, the localization of the electric current density at the top of the electrode plates is more pronounced compared to the purely electrochemical model. This suggests that electrode utilization, a limiting factor for the design of three-dimensional battery architectures, depends on the stress field that develop in the SPE. The stress level is indeed significant, and mechanical failure of the polymer

might occur during service. S. Berg et al.[62] Studied the impact of mechanical deformation on the electrochemical performance polymer electrolytes. They employed a stretchable solid polymer electrolyte film and subjected it to tensile deformation (approximately 48% strain), through which ion diffusion occurs while observing thermodynamics laws which governs Multiphysics equations accounting for large deformation mechanics and material nonlinearity. Firstly, they used a theoretical approach to demonstrate how through-plane ionic conductivity changes when the polymer is subjected to stretching. Secondly, they used experiment method to measure changes in through-plane ionic conductivity with applied uniaxial strain in a sample of polyethylene oxide (PEO). Their findings showed that both theoretical and experimental results are in good agreement that ion conduction is enhanced with increasing strain which underscore the importance of the study of mechanical deformation in solid state electrolyte. Yaolong He et al. [63] carried out the mechanical integrity of a solid polymer electrolyte (SPE) in an all-solid-state batteries (ASSBs) by implementing a sequence of quasi-static uniaxial tension and stress relaxation tests on a lithium perchlorate-doped poly (vinyl alcohol) electrolyte, and then discussed the viscoelastic behaviour as well as the strength of SPE film during the physical ageing process. It was observed that the measured elastic modulus, yield stress, and characteristic relaxation time boost with the prolonged ageing time. Also, it was observed that the shape factor for the classical time-decay equation and the tensile rupture strength are independent of the ageing history. Furthermore, it was seen that the peak tensile stress in SPE film for the fully discharged ASSB significantly increases as the ageing proceeds due to the stiffening of the electrolyte composite which will result in the deformation of the cell system structure.

## References

- [1] K. Moses, “Activated Carbon and Graphene Oxide for Supercapacitors and Batteries Application,” African University of Science and Technology, 2021.  
<http://repository.aust.edu.ng/xmlui/handle/123456789/5029>
- [2] L. A. Wong, V. K. Ramachandaramurthy, P. Taylor, J. B. Ekanayake, S. L. Walker, and S. Padmanaban, “Review on the optimal placement, sizing and control of an energy storage system in the distribution network,” *J. Energy Storage*, vol. 21, no. December 2018, pp. 489–504, 2019.
- [3] D. Sandoval, P. Goffin, and H. Leibundgut, “How low exergy buildings and distributed electricity storage can contribute to flexibility within the demand side,” *Appl. Energy*, vol. 187, pp. 116–127, 2017.
- [4] S. Najib and E. Erdem, “Current progress achieved in novel materials for supercapacitor electrodes: Mini review,” *Nanoscale Adv.*, vol. 1, no. 8, pp. 2817–2827, 2019.

- [5] Z. S. Iro, C. Subramani, and S. S. Dash, "A brief review on electrode materials for supercapacitor," *Int. J. Electrochem. Sci.*, vol. 11, no. 12, pp. 10628–10643, 2016.
- [6] R. Dubey and V. Guruviah, "Review of carbon-based electrode materials for supercapacitor energy storage," *Ionics (Kiel)*, vol. 25, no. 4, pp. 1419–1445, 2019.
- [7] M. Khalid, P. Bhardwaj, and H. Varela, "Carbon-Based Composites for Supercapacitor," *Sci. Technol. Adv. Appl. Supercapacitors*, 2019.
- [8] M. Faisal, M. A. Hannan, P. J. Ker, A. Hussain, M. Bin Mansor, and F. Blaabjerg, "Review of energy storage system technologies in microgrid applications: Issues and challenges," *IEEE Access*, vol. 6, no. 1, pp. 35143–35164, 2018.
- [9] M. Khalid, *A review on the selected applications of battery-supercapacitor hybrid energy storage systems for microgrids*, vol. 12, no. 23. 2019.
- [10] T. S. Mathis, N. Kurra, X. Wang, D. Pinto, P. Simon, and Y. Gogotsi, "Energy Storage Data Reporting in Perspective—Guidelines for Interpreting the Performance of Electrochemical Energy Storage Systems," *Adv. Energy Mater.*, vol. 9, no. 39, pp. 1–13, 2019.
- [11] X. Chen, R. Paul, and L. Dai, "Carbon-based supercapacitors for efficient energy storage," *Natl. Sci. Rev.*, vol. 4, no. 3, pp. 453–489, 2017.
- [12] A. Borenstein, O. Hanna, R. Attias, S. Luski, T. Brousse, and D. Aurbach, "Carbon-based composite materials for supercapacitor electrodes: A review," *J. Mater. Chem. A*, vol. 5, no. 25, pp. 12653–12672, 2017.
- [13] X. H. L. Wang, H. Yang, X. Liu, R. Zeng, M. Li, Y. Huang, "Constructing Hierarchical Tectorum-like  $\alpha$ -Fe<sub>2</sub>O<sub>3</sub> / PPy Nanoarrays on Carbon Cloth for Solid-State Asymmetric Supercapacitors Angewandte," *Angew. Chem Int. Ed.*, vol. 58, pp. 1105–1110, 2017.
- [14] Y. Liu, K. Shi, and I. Zhitomirsky, "Asymmetric supercapacitor, based on composite MnO<sub>2</sub>-graphene and N-doped activated carbon coated carbon nanotube electrodes," *Electrochim. Acta*, vol. 233, pp. 142–150, 2017.
- [15] G. H. Sonawane, S. P. Patil, and S. H. Sonawane, "Nanocomposites and Its Applications," *Appl. Nanomater.*, pp. 1–22, 2018.
- [16] B. Moyo, D. Momodu, O. Fasakin, A. Bello, J. Dangbegnon, and N. Manyala, "Electrochemical analysis of nanoporous carbons derived from activation of polypyrrole for stable supercapacitors," *J. Mater. Sci.*, vol. 53, no. 7, pp. 5229–5241, 2018.
- [17] X. Cao *et al.*, "Reduced Graphene Oxide-Wrapped MoO<sub>3</sub> Composites Prepared by Using Metal-Organic Frameworks as Precursor for All-Solid-State Flexible Supercapacitors," *Adv. Mater.*, vol. 27, no. 32, pp. 4695–4701, 2015.
- [18] C. C. Wang, H. C. Chen, and S. Y. Lu, "Manganese oxide/graphene aerogel composites as an outstanding supercapacitor electrode material," *Chem. - A Eur. J.*, vol. 20, no. 2, pp. 517–523, 2014.
- [19] R. Kumar, H. J. Kim, S. Park, A. Srivastava, and I. K. Oh, "Graphene-wrapped and cobalt

- oxide-intercalated hybrid for extremely durable super-capacitor with ultrahigh energy and power densities,” *Carbon N. Y.*, vol. 79, no. 1, pp. 192–202, 2014.
- [20] K. R. Reddy, M. Hassan, and V. G. Gomes, “Hybrid nanostructures based on titanium dioxide for enhanced photocatalysis,” *Appl. Catal. A Gen.*, vol. 489, pp. 1–16, 2015.
- [21] M. Biswal, A. Banerjee, M. Deo, and S. Ogale, “From dead leaves to high energy density supercapacitors,” *Energy Environ. Sci.*, vol. 6, no. 4, pp. 1249–1259, 2013.
- [22] X. Chen *et al.*, “A novel hierarchical porous nitrogen-doped carbon derived from bamboo shoot for high performance supercapacitor,” *Sci. Rep.*, vol. 7, no. 1, pp. 1–11, 2017.
- [23] A. Elmouwahidi, E. Bailón-García, A. F. Pérez-Cadenas, F. J. Maldonado-Hódar, and F. Carrasco-Marín, “Activated carbons from KOH and H<sub>3</sub>PO<sub>4</sub>-activation of olive residues and its application as supercapacitor electrodes,” *Electrochim. Acta*, vol. 229, pp. 219–228, 2017.
- [24] J. Hou *et al.*, “From rice bran to high energy density supercapacitors: A new route to control porous structure of 3D carbon,” *Sci. Rep.*, vol. 4, pp. 1–6, 2014.
- [25] J. Mi, X. R. Wang, R. J. Fan, W. H. Qu, and W. C. Li, “Coconut-shell-based porous carbons with a tunable micro/mesopore ratio for high-performance supercapacitors,” *Energy and Fuels*, vol. 26, no. 8, pp. 5321–5329, 2012.
- [26] L. Wei, M. Sevilla, A. B. Fuertes, R. Mokaya, and G. Yushin, “Hydrothermal carbonization of abundant renewable natural organic chemicals for high-performance supercapacitor electrodes,” *Adv. Energy Mater.*, vol. 1, no. 3, pp. 356–361, 2011.
- [27] T. Wei, Q. Zhang, X. Wei, Y. Gao, and H. Li, “A Facile and Low-Cost Route to Heteroatom Doped Porous Carbon Derived from Broussonetia Papyrifera Bark with Excellent Supercapacitance and CO<sub>2</sub> Capture Performance,” *Sci. Rep.*, vol. 6, no. February, pp. 2–10, 2016.
- [28] A. Barroso-Bogeat, M. Alexandre-Franco, C. Fernández-González, and V. Gómez-Serrano, “Activated carbon surface chemistry: Changes upon impregnation with Al(III), Fe(III) and Zn(II)-metal oxide catalyst precursors from NO<sub>3</sub><sup>-</sup> aqueous solutions,” *Arab. J. Chem.*, vol. 12, no. 8, pp. 3963–3976, 2019.
- [29] S. M. Yakout and G. Sharaf El-Deen, “Characterization of activated carbon prepared by phosphoric acid activation of olive stones,” *Arab. J. Chem.*, vol. 9, pp. S1155–S1162, 2016.
- [30] M. S. Shafeeyan, W. M. A. W. Daud, A. Houshmand, and A. Shamiri, “A review on surface modification of activated carbon for carbon dioxide adsorption,” *J. Anal. Appl. Pyrolysis*, vol. 89, no. 2, pp. 143–151, 2010.
- [31] D. Prahas, Y. Kartika, N. Indraswati, and S. Ismadji, “Activated carbon from jackfruit peel waste by H<sub>3</sub>PO<sub>4</sub> chemical activation: Pore structure and surface chemistry characterization,” *Chem. Eng. J.*, vol. 140, no. 1–3, pp. 32–42, 2008.
- [32] F. Yao, D. T. Pham, and Y. H. Lee, “Carbon-Based Materials for Lithium-Ion Batteries, Electrochemical Capacitors, and Their Hybrid Devices,” *ChemSusChem*, vol. 8, no. 14,

- pp. 2284–2311, 2015.
- [33] Y. J. Lee, G. P. Kim, Y. Bang, J. Yi, J. G. Seo, and I. K. Song, “Activated carbon aerogel containing graphene as electrode material for supercapacitor,” *Mater. Res. Bull.*, vol. 50, pp. 240–245, 2014.
- [34] A. Vlad, N. Singh, S. Melinte, J. F. Gohy, and P. M. Ajayan, “Carbon Redox-Polymer-Gel Hybrid Supercapacitors,” *Sci. Rep.*, vol. 6, no. February, pp. 3–8, 2016.
- [35] X. Y. Chen, C. Chen, Z. J. Zhang, and D. H. Xie, “High performance porous carbon through hard-soft dual templates for supercapacitor electrodes,” *J. Mater. Chem. A*, vol. 1, no. 25, pp. 7379–7383, 2013.
- [36] D. Das, D. P. Samal, and M. BC, “Preparation of Activated Carbon from Green Coconut Shell and its Characterization,” *J. Chem. Eng. Process Technol.*, vol. 06, no. 05, 2015.
- [37] C. Lekakou, O. Moudam, F. Markoulidis, T. Andrews, J. F. Watts, and G. T. Reed, “Carbon-based fibrous EDLC capacitors and supercapacitors,” *J. Nanotechnol.*, vol. 2011, 2011.
- [38] T. Purkait, G. Singh, D. Kumar, M. Singh, and R. S. Dey, “High-performance flexible supercapacitors based on electrochemically tailored three-dimensional reduced graphene oxide networks,” *Sci. Rep.*, vol. 8, no. 1, pp. 1–13, 2018.
- [39] R. Wang *et al.*, “Construction of 3D CoO Quantum Dots/Graphene Hydrogels as Binder-Free Electrodes for Ultra-high Rate Energy Storage Applications,” *Electrochim. Acta*, vol. 243, pp. 152–161, 2017.
- [40] W. Li, J. Liu, and D. Zhao, “Mesoporous materials for energy conversion and storage devices,” *Nat. Rev. Mater.*, vol. 1, no. 6, 2016.
- [41] A. S. Aricò, P. Bruce, B. Scrosati, J.-M. Tarascon, And W. Van Schalkwijk, “Nanostructured materials for advanced energy conversion and storage devices,” *Mater. Sustain. Energy*, vol. 4, no. May, pp. 148–159, 2010.
- [42] F. M. Guo *et al.*, “High performance of stretchable carbon nanotube-polypyrrole fiber supercapacitors under dynamic deformation and temperature variation,” *J. Mater. Chem. A*, vol. 4, no. 23, pp. 9311–9318, 2016.
- [43] M. Rajesh, C. J. Raj, R. Manikandan, B. C. Kim, S. Y. Park, and K. H. Yu, “A high performance PEDOT/PEDOT symmetric supercapacitor by facile in-situ hydrothermal polymerization of PEDOT nanostructures on flexible carbon fibre cloth electrodes,” *Mater. Today Energy*, vol. 6, pp. 96–104, 2017.
- [44] E. V. Lobiak *et al.*, “One-step chemical vapor deposition synthesis and supercapacitor performance of nitrogen-doped porous carbon-carbon nanotube hybrids,” *Beilstein J. Nanotechnol.*, vol. 8, no. 1, pp. 2669–2679, 2017.
- [45] S. Venkateshalu, D. Rangappa, and A. N. Grace, “Hydrothermal Synthesis and Electrochemical Properties of CoS<sub>2</sub>-Reduced Graphene Oxide Nanocomposite for Supercapacitor Application,” *Int. J. Nanosci.*, vol. 17, no. 1–2, pp. 1–8, 2018.

- [46] J. J. Li *et al.*, “Advanced asymmetric supercapacitors based on  $\text{Ni}_3(\text{PO}_4)_2@\text{GO}$  and  $\text{Fe}_2\text{O}_3@\text{GO}$  electrodes with high specific capacitance and high energy density,” *RSC Adv.*, vol. 5, no. 52, pp. 41721–41728, 2015.
- [47] A. Moftah and A. Al Shetiti, “Review of Supercapacitor Technology,” no. November, 2019.
- [48] A. Laheäär, P. Przygocki, Q. Abbas, and F. Béguin, “Electrochemistry Communications Appropriate methods for evaluating the efficiency and capacitive behavior of different types of supercapacitors,” vol. 60, pp. 21–25, 2015.
- [49] S. Li *et al.*, “Electrochimica Acta Effect of sulfolane on the performance of lithium bis ( oxalato ) borate-based electrolytes for advanced lithium ion batteries,” *Electrochim. Acta*, vol. 65, pp. 221–227, 2012.
- [50] H. Xiang, J. Chen, Z. Li, and H. Wang, “An inorganic membrane as a separator for lithium-ion battery,” *J. Power Sources*, vol. 196, no. 20, pp. 8651–8655, 2011.
- [51] X. Huang and J. Hitt, “Lithium ion battery separators : Development and performance characterization of a composite membrane,” *J. Memb. Sci.*, vol. 425–426, pp. 163–168, 2013.
- [52] T. Sudiarti, D. Wahyuningrum, B. Bundjali, and I. Made Arcana, “Mechanical strength and ionic conductivity of polymer electrolyte membranes prepared from cellulose acetate-lithium perchlorate,” *IOP Conf. Ser. Mater. Sci. Eng.*, vol. 223, no. 1, 2017.
- [53] E. Vaulina and S. Widyaningsih, “Mechanical strength and ionic conductivity of polymer electrolyte membranes prepared from cellulose acetate-lithium perchlorate.”
- [54] L. Yue *et al.*, “All solid-state polymer electrolytes for high-performance lithium ion batteries,” *Energy Storage Mater.*, vol. 5, pp. 139–164, 2016.
- [55] T. M. Wilkinson, S. Zargari, M. Prasad, and C. E. Packard, “Optimizing nano-dynamic mechanical analysis for high- resolution , elastic modulus mapping in organic-rich shales,” pp. 1041–1049, 2015.
- [56] H. Amanieu, D. Rosato, M. Sebastiani, F. Massimi, and D. C. Lupascu, “Materials Science & Engineering A Mechanical property measurements of heterogeneous materials by selective nanoindentation : Application to  $\text{LiMn}_2\text{O}_4$  cathode,” *Mater. Sci. Eng. A*, vol. 593, pp. 92–102, 2014.
- [57] L. L. Baranowski, C. M. Heveran, V. L. Ferguson, and C. R. Stoldt, “Multi-Scale Mechanical Behavior of the  $\text{Li}_3\text{PS}_4$  Solid-Phase Electrolyte,” pp. 4–10, 2016.
- [58] D. Golodnitsky, E. Strauss, E. Peled, and S. Greenbaum, “Review—On Order and Disorder in Polymer Electrolytes,” *J. Electrochem. Soc.*, vol. 162, no. 14, pp. A2551–A2566, 2015.
- [59] H. C. Yu *et al.*, “Deformation and stresses in solid-state composite battery cathodes,” *J. Power Sources*, vol. 440, no. September, 2019.
- [60] Y. Kamikawa, K. Amezawa, and K. Terada, “Elastic-Plastic Deformation of a Solid

- Electrolyte Interface Formed by Reduction of Fluoroethylene Carbonate: A Nanoindentation and Finite Element Analysis Study,” *J. Phys. Chem. C*, vol. 124, no. 41, pp. 22488–22495, 2020.
- [61] D. Grazioli, V. Zadin, D. Brandell, and A. Simone, “Electrochemical-mechanical modeling of solid polymer electrolytes: Stress development and non-uniform electric current density in trench geometry microbatteries,” *Electrochim. Acta*, vol. 296, pp. 1142–1162, 2019.
- [62] S. Berg, T. Kelly, I. Porat, B. Moradi-Ghadi, and H. Ardebili, “Mechanical deformation effects on ion conduction in stretchable polymer electrolytes,” *Appl. Phys. Lett.*, vol. 113, no. 8, 2018.
- [63] Y. He, S. Li, S. Zhou, and H. Hu, “Mechanical integrity degradation and control of all-solid-state lithium battery with physical aging poly (vinyl alcohol)-based electrolyte,” *Polymers (Basel)*, vol. 12, no. 9, 2020.

## CHAPTER THREE

### 3.0. Processing of $\alpha$ -Fe<sub>2</sub>O<sub>3</sub> Nanoparticles on Activated Carbon Cloth as Binder-Free Electrode Material for Supercapacitor Energy Storage

#### 3.1. Introduction

New research directions towards flexible electronics have greatly inspired the development of thin film energy storage devices, [1,2] as well as thin-film batteries [3] and micro-supercapacitors (MSCs) [4]. Supercapacitors (SCs) have exceptional properties such as high power density, long lifetimes, facile fabrication, low cost, and little or no maintenance requirements [5] they are used in hybrid electric vehicles (HEVs) to increase efficiency. They can also complement or replace batteries in electrical energy storage applications [6]. Since hybrid vehicles turn off the engine completely when the car comes to a stop, supercapacitors can offer efficient power for rapid restarts. There is, therefore, an interest in the development of high performance energy storage devices. Furthermore, with the opportunities for further integration into electric or hybrid electric vehicles, it is increasingly important for supercapacitors to be small, lightweight, stretchable and flexible. However, currently available supercapacitors with liquid electrolytes are limited by the leakage of electrolyte, low energy densities (both in weight and volume), and the low yield of the electrode materials.

In the case of organic electrolytes and ionic liquids, they are associated with challenges of low ionic conductivity (high internal resistance), highly flammable, high electrolyte leakage and are quite expensive [7], but they are capable of withstanding very high potential which stands as a merit to these electrolytes. Apart from these electrolytes, redox active electrolytes are also being investigated, for example, Le-Qing Fan et. al. [8] reported a redox-active ionic liquid-based ionogel electrolyte (IGE) consisting of 1-butyl-3-methylimidazolium iodide (BMIMI) IL, poly

(vinylidene fluoride-co-hexafluoropropylene) (PVDF-HFP) and carbon nanotubes (CNTs) prepared using a solution casting method. The devices fabricated using this electrolyte displayed a high specific energy of  $50.1 \text{ Wh kg}^{-1}$  as a result of pseudocapacitance contribution from the redox-reactions and the increased ionic conductivity of CNTs network that provided a fast ion transfer channel. A redox-active poly(vinyl alcohol) (PVA)-based gel polymer electrolyte (GPE) [9] with a maximum ionic conductivity of  $61.1 \text{ mS cm}^{-1}$  also achieved a high energy density of  $43.1 \text{ Wh kg}^{-1}$ . Research report on carbon hydrangeas with typical ionic liquid matched pores was also reported [10] using a simple synthetic route to obtain carbon hydrangeas integrated with unique geometry, high surface areas, with a well-developed pore structure which could achieves an ultrahigh specific energy of  $101.2 \text{ Wh kg}^{-1}$ . Core shells of hierarchical porous carbon spheres with N/O doping, was used as efficient energy materials displayed a large specific energy of  $31.6 \text{ Wh kg}^{-1}$  at a specific power of  $550 \text{ W kg}^{-1}$  with a high voltage of  $2.25 \text{ V}$ . This was accompanied with a capacitance retention of 86.2% after 10,000 cycles and broad temperature applicability from  $20$  to  $80 \text{ }^\circ\text{C}$  [11]. Pseudocapacitive materials that store charges electrochemically have attracted significant attention in recent years due to their high theoretical specific capacity, as well as their high energy densities. Transition metal oxides that have been explored as electrode materials in include  $\text{RuO}_2$ , [12]  $\text{MnO}_2$  [13],  $\text{Co}_2\text{O}_3$  [14],  $\text{Co}_3\text{O}_4$  [15],  $\text{NiO}$  [16,17],  $\text{Fe}_3\text{O}_4$  [18],  $\text{TiO}_2$  [19], and  $\text{V}_2\text{O}_5$  [20]. Thus, in this current work, we explore the use of Iron oxide ( $\alpha\text{-Fe}_2\text{O}_3$ ) as a promising electrode material for potential applications in supercapacitors. This is due to its high theoretical capacity, environmental friendliness and abundance [21]. Iron oxide has also been shown to exhibit high oxygen ion mobility on the surfaces of electrodes during redox reactions [22–24]. The use of carbon cloth is explored due to its attractive combination of flexibility, good electrical conductivity, high specific surface area,

large capacitance, and chemical/thermal stability as well their versatile syntheses route [25–27]. Different forms of carbon materials such as carbide-derived carbons [28,29], graphene [30,31], onion rings [32,33] activated carbon [34], carbon nanotubes (CNTs) [35,36], and carbon aerogels [37] have been tested as electrodes for supercapacitors. Composite of transition metal oxide have also been explored, for example Ye et al. [38] reported core-shell carbon-coated ferric oxide ( $\text{Fe}_2\text{O}_3@\text{C}$ ) nanoparticles with excellent supercapacitor electrochemical performance. Mahdi et al.[39], fabricated nano  $\text{Fe}_2\text{O}_3$ /carbon black electrodes using a mechanical pressing method. The supercapacitor based on  $\text{Fe}_2\text{O}_3$ /carbon black had a specific capacitance of  $40.07 \text{ Fg}^{-1}$  in 2 M KCl at  $10 \text{ mVs}^{-1}$  and retained 80% of their capacitance after 500 cycles. Ying Li et al. [40], prepared  $\text{Fe}_2\text{O}_3$ /activated carbon using a solvothermal method and the devices, based on  $\text{Fe}_2\text{O}_3$ /activated carbon, possessed high specific capacitance values of about  $240 \text{ Fg}^{-1}$  at  $1 \text{ Ag}^{-1}$ .

Luo et al. [41], reported that  $\text{Fe}_2\text{O}_3@\text{C}$  was prepared with pyrolyzine  $\text{Fe}(\text{NO}_3)_3 \cdot 9\text{H}_2\text{O}$  impregnated starch gels and  $\text{Fe}_2\text{O}_3@\text{C}$  had a specific capacitance of  $267.2 \text{ Fg}^{-1}$  at  $0.35 \text{ Ag}^{-1}$  with a high voltage of 1-4 V, retained 91.7% of its capacitance after 5000 cycles. In 2018, Jien Li et al.[42] reported a large area specific capacitance (up to  $2775 \text{ mF cm}^{-2}$ ) using porous  $\text{Fe}_2\text{O}_3$  nanospheres that were anchored to activated carbon cloth. They were able to show that  $\text{Fe}_2\text{O}_3@\text{ACC}$  electrodes have large specific capacitance, compared to  $\text{Fe}_2\text{O}_3$  based electrodes in aqueous electrolytes. They also demonstrated that  $\text{Fe}_2\text{O}_3@\text{ACC}$  has higher specific capacitance in positive potential windows than in negative potential windows at a scan rate larger than  $30 \text{ mVs}^{-1}$ , they concluded that the low diffusion potential barrier for  $\text{Li}^+$  ions on  $\text{Fe}_2\text{O}_3$  contributed to the excellent pseudocapacitive performance. They also acknowledged the poor stability of challenges of most Fe-based electrodes, and the effects of such stability on supercapacitor performance and cycle life.

In this work, we will explore the development of a one-step method for the processing of electrode materials for supercapacitors. A facile, one-step, hydrothermal method will be used to optimize the synthesized  $\alpha$ -Fe<sub>2</sub>O<sub>3</sub> nanoparticles on carbon cloth and activated carbon cloth. The latter and the former will be studied as binder-free flexible materials for the fabrication of stretchable symmetric supercapacitor electrode materials for energy storage. The  $\alpha$ -Fe<sub>2</sub>O<sub>3</sub> nanoparticles will be grown on conductive carbon cloth that will serve as a scaffold for quick electron transport, while providing strong support. We will also avoid the use of polymer binder/conductive additives, while exploring the development of novel flexible supercapacitors with improved capacity for energy storage [42].

## 3.2. Materials and Experimental Methods

### 3.2.1. Materials

The chemicals and reagents were used as received without any further purification. The Iron (III) Chloride Anhydrous (FeCl<sub>3</sub>.6H<sub>2</sub>O, >98%) and Sodium Sulfate Anhydrous (Na<sub>2</sub>SO<sub>4</sub>, after drying 99%) were purchased from Merck Millipore, Darmstadt, Germany. The Sulfuric acid (H<sub>2</sub>SO<sub>4</sub>, 98%) and Nitric acid (HNO<sub>3</sub>, 69%) used for the activation of the carbon cloth were purchased from Sigma-Aldrich, Darmstadt, Germany. Ethanol (C<sub>2</sub>H<sub>5</sub>OH, 99.9%) used was obtained from Ultrapure, Darien, Connecticut, USA. Potassium hydroxide Pellets (KOH, 85%) was purchased from Merck Millipore, Darmstadt, Germany. It was used for the preparation of 3 M KOH electrolyte. Deionized water was used for the preparation of the samples. The carbon cloth was purchased from Sainergy Fuel India Pvt Ltd, Chennai, Tamil Nadu, India.

### 3.3. Activation Process of the Carbon Cloth (CC)

Before carrying out the hydrothermal process, the carbon cloth (CC) was treated for 2 hours with a mixture of  $\text{H}_2\text{SO}_4$  and  $\text{HNO}_3$  in a volume ratio of 1:3 at  $80\text{ }^\circ\text{C}$  [43]. The treated CC was then washed with deionized (DI) water, sonicated for 10 minutes, cleansed with ethanol, sonicated for 10 minutes, and dried in a vacuum oven at  $60\text{ }^\circ\text{C}$  for 12 hours.

#### **3.3.1. Preparation of $\alpha\text{-Fe}_2\text{O}_3$ Nanoparticles on CC and Activated Carbon Cloth (ACC)**

Various concentration of  $\text{FeCl}_3 \cdot 6\text{H}_2\text{O}$  (0.05g, 0.1g, 0.2g, 0.4g and 0.8g) and a constant concentration (0.1195 g) of  $\text{Na}_2\text{SO}_4$  were prepared by dissolving and stirring in a 35 mL aqueous solution for 10 minutes, before transferring to a Teflon-lined stainless-steel autoclave. The different concentrations prepared, was optimized on the CC as shown in Table 1. The optimized parameter was then repeated for the ACC as follows; the dried CC or ACC were immersed in the resulting solution prior to hydrothermal treatment at  $120\text{ }^\circ\text{C}$  for 6 hours. This was followed by annealing in Argon gas at  $450\text{ }^\circ\text{C}$  for 3 hours to obtain the required  $\alpha\text{-Fe}_2\text{O}_3$  nanoparticles on the CC and ACC [44]. To examine the  $\text{Fe}_2\text{O}_3$  that was deposited on the ACC, the powder in the Teflon-lined stainless-steel autoclave was recovered and centrifuged at 5500 rpm for 12 minutes, followed by washing with deionized water and ethanol respectively and dried in a vacuum oven at  $60\text{ }^\circ\text{C}$  for 6 hours. The dried material was annealed in Argon gas at  $450\text{ }^\circ\text{C}$  for 3 hours to obtain the required  $\alpha\text{-Fe}_2\text{O}_3$  powder.

### 3.4. Materials Characterization

The surface morphology of samples was characterized using a scanning electron microscope (SEM Hitachi S-3400N), while the microstructure was characterized using a JEOL Model JSM-7600F Field-Emission Gun Scanning Electron Microscope (FEGSEM). High-resolution Transmission Electron Microscopy (HRTEM) was carried out using a JEOL Model JEM 2100F

high resolution transmission electron microscope with the following characteristics (point resolution 0.19 nm; line resolution of 0.1 nm). The HRTEM was carried out with a magnification range between 50 x and 1.5M x at 200 kV, Selected Area Diffraction patterns were obtained from the HRTEM. X-ray diffraction (XRD) patterns use to obtain information about the crystallinity of the samples were obtained using a Philips X-Pert PRO X-ray diffractometer with N-filtered Cu K $\alpha$  radiation ( $\lambda = 1.5418 \text{ \AA}$ ) in the range ( $2\theta = 10-90^\circ$ ) (Manufactured by PANalytical, Almelo, the Netherlands). Raman spectroscopy produces a unique fingerprint for identification of materials using the vibrational modes present in the materials. In this regard, Raman data were acquired using the Horiba HR800 UV spectrometer (Horiba Jobin-Yvon Kyoto, Japan) with an excitation wavelength of 514.4 nm, 5 mW power and 30 seconds exposure time and 100x resolution lens. Surface analysis of the sample was performed using the X-ray photoelectron spectroscopy (XPS) Kratos Analytical, Stretford, Manchester, United Kingdom (UK) (Axis Supra) with analysis pressure of  $< 2 \times 10^{-9}$  Torr. The XPS was used to determine chemical compositions and the presence of functional groups in the samples. The XPS system was fitted with a monochromatic Al K $\alpha$  (1486.6 eV) X-ray source.

### 3.5. Preparation of the binder-free Electrodes and assembly of Symmetrical Device.

Two pieces of the  $\alpha$ -Fe<sub>2</sub>O<sub>3</sub>-ACC (same was carried out for  $\alpha$ -Fe<sub>2</sub>O<sub>3</sub>-CC) with area cross sections of 2 cm x 2 cm and Whatman™ (Cytiva, Mariborough, Massachusetts, USA) filter paper 42, with area cross sections of 2.5 cm x 2.5 cm, serve as separators. They were immersed in a 3 M KOH aqueous electrolyte, to soak for 12 hours before been transferred into a Swagelok setup for electrochemical measurements in a Biological Potentiostat (SP-300, Manufactured by Biologic, Seyssinet-Pariset, France). The electrochemical measurements were carried out within a window of 0-1 V at scan rates between 2 mV s<sup>-1</sup> and 200 mV s<sup>-1</sup>. The galvanostatic charge-discharge

(GCD) was carried out within a potential window of 0-1 V at various specific currents. Electrochemical Impedance Spectroscopy (EIS) was carried out within a frequency range between 100 kHz to 10 mHz. The stability of the device was measured at a constant applied specific current, set at 1 V for 10000 cycles.

## 3.6. Results and Discussion

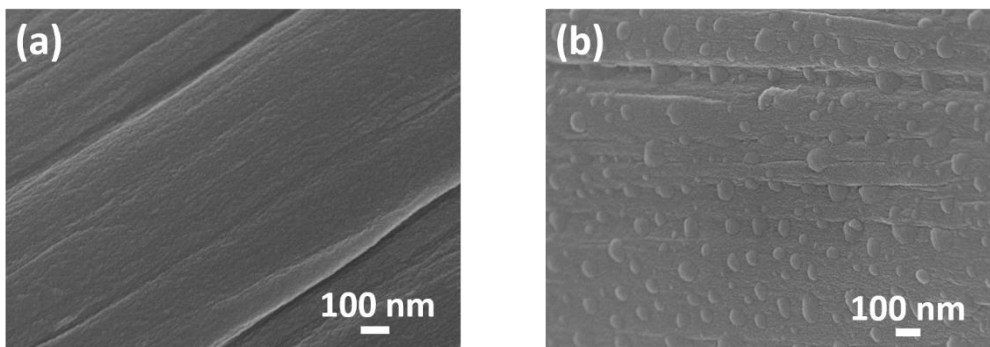
### 3.6.1. Microstructure and Morphology

The microstructures and surface morphologies produced as a result of the deposition of  $\alpha$ -Fe<sub>2</sub>O<sub>3</sub> on the CC and ACC are presented in fig. 3.1. Figure 3.1 (a and b) show the surfaces for the CC and ACC, the micrograph for the CC shows a very plain surface while the ACC shows a very rough surface due to the acid treatment, this is expected to enhance the growth and homogenous dispersion of the nanoparticles. Furthermore, at the same deposition conditions, well-controlled, well-defined and uniform particle coating morphologies were observed after the activation of the ACC as shown in figs. 3.1 (c-d). Higher levels of  $\alpha$ -Fe<sub>2</sub>O<sub>3</sub> deposition resulted in thick, agglomerated coatings on the plain of both sample when the mass was increased from 0.1 to 0.2 g as shown in fig. (e-f). The differences in the  $\alpha$ -Fe<sub>2</sub>O<sub>3</sub> nanoparticle growth on the ACC and CC were attributed to the effects of oxidation and the functional groups present on the surfaces of the CC after the acid treatment. The activation of the carbon cloth modified the surfaces for covalent bonding, due to the presence of the hydroxyl and carboxylic groups [42] which resulted in a more uniform coating of the ACC with nanoparticles than the CC. Furthermore, the ACC provided more surface area for redox reactions and covalent bonding. This again suggests that the  $\alpha$ -Fe<sub>2</sub>O<sub>3</sub> particles were more strongly bonded to the ACC than the CC. The HR-TEM was also used for direct imaging of the structures of the samples and was carried out on the powder that was obtained from the surface of the CC and ACC before and after annealing. The results of

the images and the corresponding inset of the selected area electron diffraction (SAED) pattern are presented in

fig. 3.1 (g, h). The SAED pattern confirms the crystallinity of the  $\alpha\text{-Fe}_2\text{O}_3$  nanoparticles. HR-TEM images of the samples taken before and after annealing shows two different morphologies. The formation of  $\text{Fe}_2\text{O}_3$  from the hydrothermal process resulted in rod-like structures with low intensity peaks as observed from the XRD data presented in fig. 3.2b However, after annealing in an argon atmosphere for 3 hours at 450 °C a shape changes from rod to irregular spherical shapes. The formation of the irregular nanoparticles could be due to aggregation in oriented alignment of the rods directly side by side, followed by fusion to form the spherical particles observed in the TEM micrographs. The SAED pattern (inset) revealed the crystallinity of the sample as shown in

Fig. 3.1 (g, h). This is in agreement with the XRD data which correspond to the crystalline phase observed.



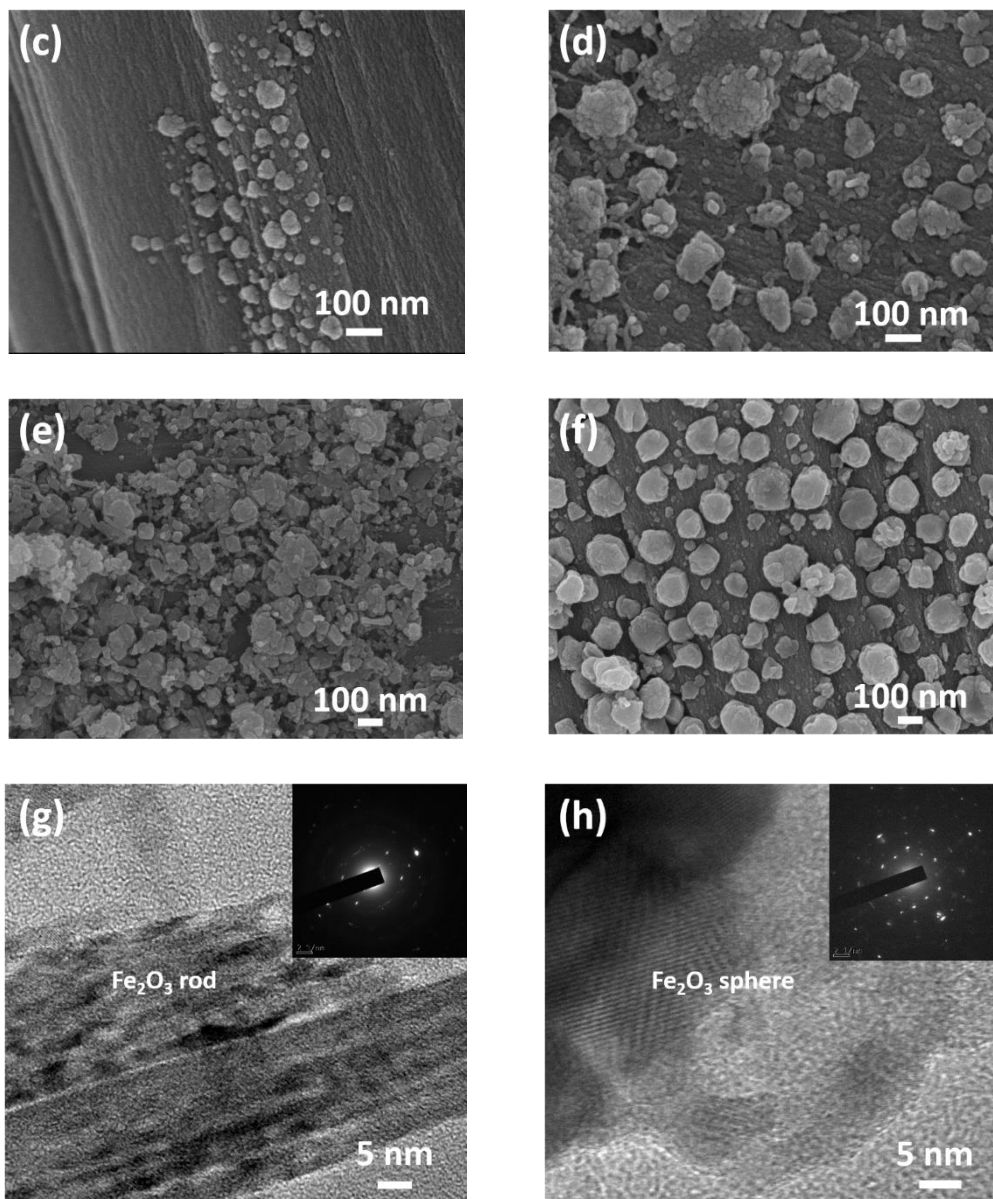


Figure 3.1. SEM micrographs (a) Untreated CC (b) Activated CC (c) 0.1g  $\alpha$  –  $\text{Fe}_2\text{O}_3$ -CC (d) 0.1g  $\alpha$  –  $\text{Fe}_2\text{O}_3$ -ACC (e) 0.2g  $\alpha$  –  $\text{Fe}_2\text{O}_3$ -CC (f) 0.2g  $\alpha$  –  $\text{Fe}_2\text{O}_3$ -ACC. HRTEM images (g) Unannealed  $\text{Fe}_2\text{O}_3$  (h) annealed  $\text{Fe}_2\text{O}_3$ .

The crystallographic structures of the CC, ACC,  $\text{Fe}_2\text{O}_3$ ,  $\alpha$ - $\text{Fe}_2\text{O}_3$ - CC and  $\alpha$ - $\text{Fe}_2\text{O}_3$ - ACC were investigated using X-ray diffraction (XRD) and the results are presented in Figs. 3.2. The XRD results obtained from the structures deposited on CC and ACC in fig. 3a revealed two peaks at  $26^\circ$  and  $43^\circ$  respectively. These peaks confirm the presence of graphitic carbon phases of (012) and (113) using JCPDs no. 33-0664. The obtained  $\text{Fe}_2\text{O}_3$  powder revealed low intensity peaks at

21.2°, 26.8°, 36.6°, 53° and can be indexed to the JCPDs no. 85-0987. However, after annealing a hematite crystalline phase of  $\alpha$ -Fe<sub>2</sub>O<sub>3</sub> is observed in fig. 3.2b with sharp peaks at 30.17°, 35.59°, 44.68°, 57.3°, 62.75°, 65.03° and 82.3° indexed to hematite phase corresponding to planes indexed at (104), (110), (113), (018), (214), (300) and (220) with reference to JCPDs no. 85-0987. Similar peaks were observed on the CC and ACC substrates at 26°, 30.17°, 35.59°, 43°, 53°, 62.4° and 26°, 30.17°, 35.59°, 43°, 53°, 62.4° with presence of the carbon peaks indicating that  $\alpha$ -Fe<sub>2</sub>O<sub>3</sub> was grown successfully on CC and ACC. The low intensity peaks observed in fig. 3.2c for the iron oxide is due to the sensitivity of these peaks to the presence of carbon in the material.

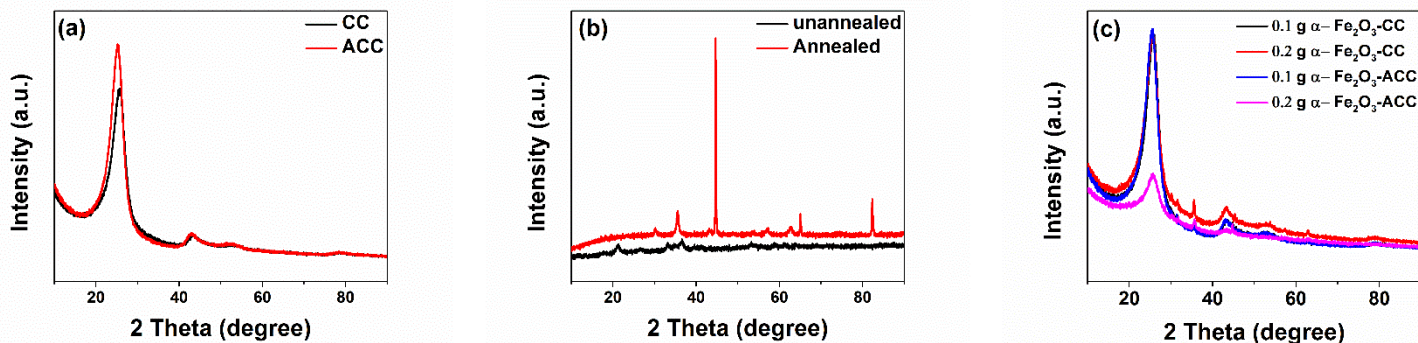


Figure 3.2. XRD patterns (a) CC & ACC (b) unannealed Fe<sub>2</sub>O<sub>3</sub> and annealed  $\alpha$ -Fe<sub>2</sub>O<sub>3</sub> powder (c) 0.1 g and 0.2g  $\alpha$ -Fe<sub>2</sub>O<sub>3</sub> on CC, 0.1 g and 0.2 g  $\alpha$ -Fe<sub>2</sub>O<sub>3</sub> on ACC.

Further confirmation of the growth of  $\alpha$ -Fe<sub>2</sub>O<sub>3</sub> nanoparticles on CC and ACC was provided by the Raman spectra shown in Fig. 3.3. The Raman spectra obtained from the structures grown on CC and ACC had vibrational modes at 1347 cm<sup>-1</sup> and 1588 cm<sup>-1</sup>. These correspond respectively to the “D-band” and the “G-band” in-plane vibrations of graphite [45]. The intensity of the D and G band is higher in the CC than in the ACC this is because these are susceptible and sensitive to any form of doping. Thus, the acid treatment led to a decrease in the intensity of the ACC. The

Raman spectra of the  $\alpha$ -Fe<sub>2</sub>O<sub>3</sub>-CC and  $\alpha$ -Fe<sub>2</sub>O<sub>3</sub>-ACC had vibrational modes at 222 cm<sup>-1</sup>, 286 cm<sup>-1</sup>, 393 cm<sup>-1</sup>, 492 cm<sup>-1</sup>, 661 cm<sup>-1</sup>, 1347 cm<sup>-1</sup>, 1588cm<sup>-1</sup> and 225 cm<sup>-1</sup>, 290 cm<sup>-1</sup>, 398 cm<sup>-1</sup>, 496 cm<sup>-1</sup>, 609 cm<sup>-1</sup>, 659 cm<sup>-1</sup>, 1347 cm<sup>-1</sup>, 1588cm<sup>-1</sup> respectively. For the CC, the  $\alpha$ -Fe<sub>2</sub>O<sub>3</sub> A1g mode can be seen in 222 cm<sup>-1</sup> and 492 cm<sup>-1</sup> while the Eg mode can be located at 241 cm<sup>-1</sup>, 286 cm<sup>-1</sup> and 661 cm<sup>-1</sup>. For the ACC, the  $\alpha$ -Fe<sub>2</sub>O<sub>3</sub> A1g mode can be seen in 225 cm<sup>-1</sup>, 496 cm<sup>-1</sup>, while the Eg mode can be located at 244 cm<sup>-1</sup>, 290 cm<sup>-1</sup>, 609 cm<sup>-1</sup> and 659 cm<sup>-1</sup> respectively. The slight shift in the position of the A1g and Eg is due to the acid treatment. From the results, the Raman spectra of ACC coated with  $\alpha$ -Fe<sub>2</sub>O<sub>3</sub> had lower intensities than those of the  $\alpha$ -Fe<sub>2</sub>O<sub>3</sub>- CC structures deposited on ACC. The complete nature of the Raman spectra and the XRD results confirm that the  $\alpha$ -Fe<sub>2</sub>O<sub>3</sub> phase was fully formed.

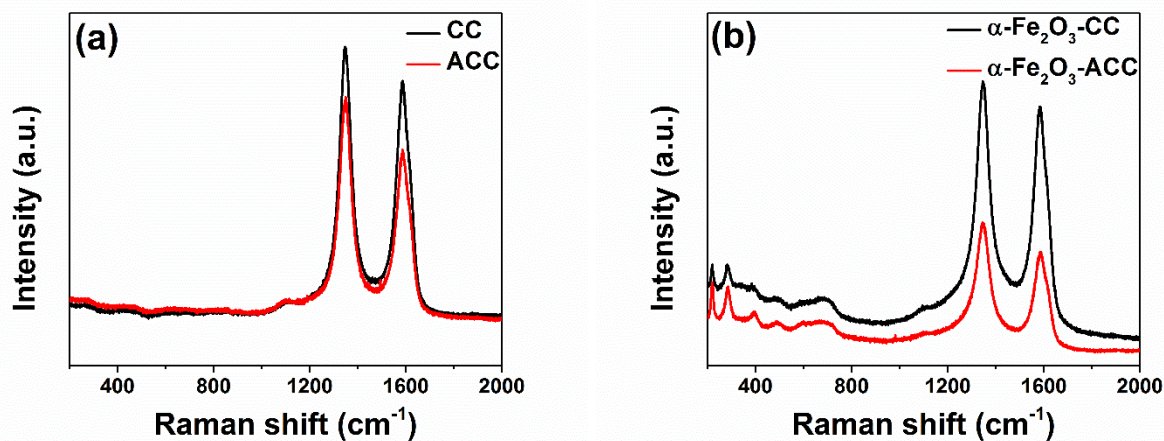
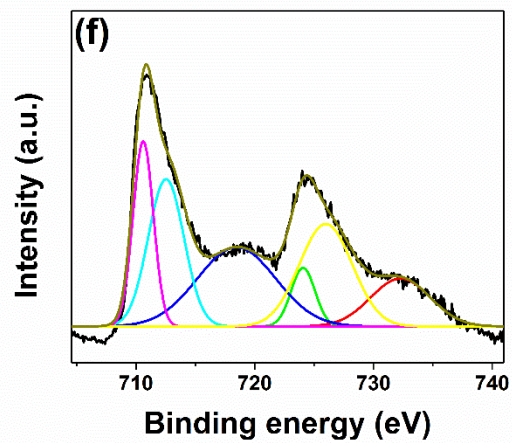
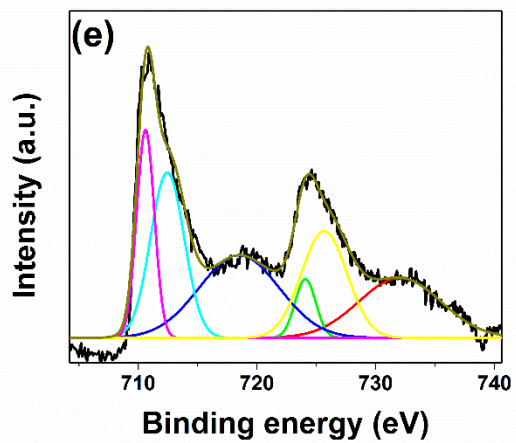
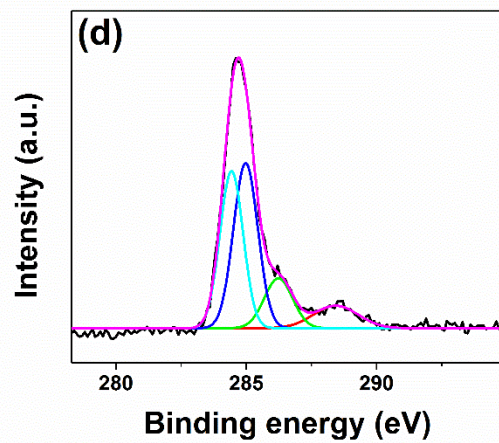
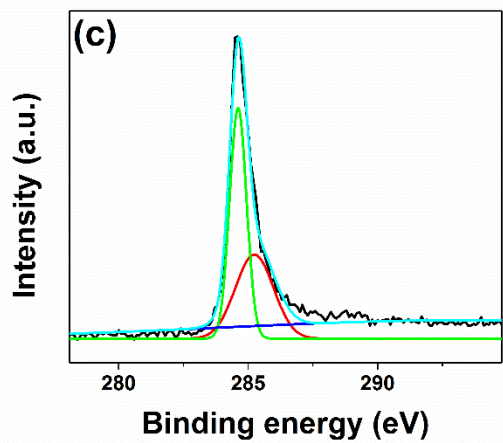
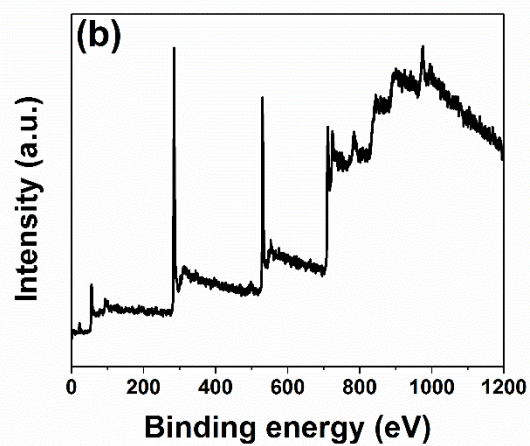
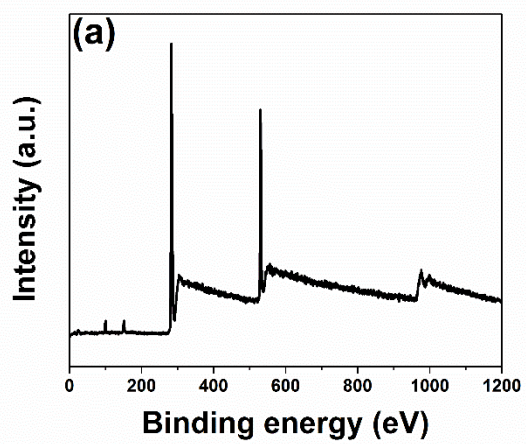


Figure 3.3. Raman spectra (a) ACC & CC (b)  $\alpha$ -Fe<sub>2</sub>O<sub>3</sub>-ACC &  $\alpha$ -Fe<sub>2</sub>O<sub>3</sub>-CC

The chemical composition and functional groups of the  $\alpha$ -Fe<sub>2</sub>O<sub>3</sub>-CC and  $\alpha$ -Fe<sub>2</sub>O<sub>3</sub>-ACC were characterized using X-ray photoelectron spectroscopy (XPS). Typical XPS spectra are presented in Fig. 3.4 (a and b) long scan revealing the presence of Carbon (C), Iron (Fe) and Oxygen (O) in

both samples. However, in the  $\alpha$ -Fe<sub>2</sub>O<sub>3</sub>-ACC samples the iron deposition is 24% higher in magnitude compared with the  $\alpha$ -Fe<sub>2</sub>O<sub>3</sub>-CC as shown in the table 3.1. This is due to the functionalization (activation) of the carbon cloth that increase the oxygen functional group and allow for bonding with the Fe during the hydrothermal process. The results of the peak fitting for the C1s region at 285.1eV Fig. 4 (c and d) was Fitted by four components corresponding to graphitic carbon from the CC as, hydrocarbons (CH<sub>x</sub>), alcoholic (C-O-) and/or carbon structures and carboxyl or ester (COO). The graphitic carbon takes the largest percentage of 54.8%. The Fe2p region at 716.4eV and 730.7 eV correspond to Fe 2p<sub>3/2</sub> and Fe 2p<sub>1/2</sub>, respectively, could be assigned to Fe<sub>2</sub>O<sub>3</sub> which is as a result from spin-orbit (j-j) coupling and is in accordance with literature values [46–48]. The Fe peak was fitted with six peaks in both cases as shown in table 3.1. The distributions of these peaks show a characteristic peak at 710.6 eV, trailed by various splitting of the four peaks as shown in fig. 3.4 (e and f). This is consistent with literature for the Fe<sup>3+</sup> ion oxidation state and also affirms that the peaks presented are typical of Fe<sub>2</sub>O<sub>3</sub> [46]. The O1s region (Fig. 3.5d) was fitted by two components corresponding to C-OH, C=O and C(O)O, respectively [45, 48] as presented in table 3.1. The presence of all these functional groups on the surface of this activated carbon cloth could prevent oxygen and hydrogen over potential in aqueous electrolytes as mentioned by Bichat et al. [49].



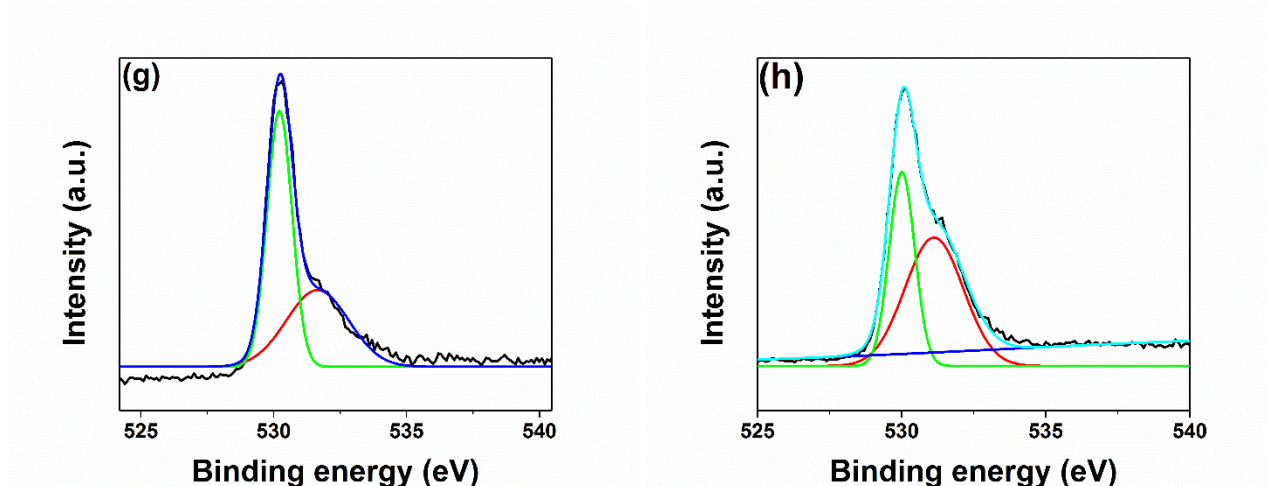


Figure 3.4. XPS spectra (a, b) Long scan, (c, d) C1s, (e, f) Fe2p and (g, h) O1 peaks of the  $\alpha$ -Fe<sub>2</sub>O<sub>3</sub>-CC and  $\alpha$ -Fe<sub>2</sub>O<sub>3</sub>-ACC respectively.

Table 3.1. XPS peak fitting results for  $\alpha$ -Fe<sub>2</sub>O<sub>3</sub>-CC and  $\alpha$ -Fe<sub>2</sub>O<sub>3</sub>-ACC.

Region	BE [eV]		Mass. Conc. (%)		Assigned to	Reference
	$\alpha$ -Fe <sub>2</sub> O <sub>3</sub> -CC	$\alpha$ -Fe <sub>2</sub> O <sub>3</sub> -ACC	$\alpha$ -Fe <sub>2</sub> O <sub>3</sub> -CC	$\alpha$ -Fe <sub>2</sub> O <sub>3</sub> -ACC		
C 1s		288.4			C-C	[50]
	285.24				CH <sub>x</sub>	[51]
		284.43	74.76	54.79	C-O-	[50]
	284.61				COO	[50]
	284.6	284.97			oxide/hydroxi de	[52]
		286.3				

	732.2					
		732.4				
	725.73					
		725.96				
	724.1					
		724.11			Fe <sup>3+</sup>	
Fe 2p	718.6		1.09	26.68		[46][48]
		718.6			Fe <sup>2+</sup>	
	712.36					
		712.45				
	710.6					
		710.6				
						[53]
	530.18	531.1			C-O-	
O 1s			24.15	18.53		[50]
	531.8	530.0			COO	
						[50]

### 3.6.2. Electrochemical Performance of Binder-free Electrodes

The  $\alpha$ -Fe<sub>2</sub>O<sub>3</sub>-CC and  $\alpha$ -Fe<sub>2</sub>O<sub>3</sub>-ACC were used as the working electrodes in a two-electrode system in 3 M KOH electrolyte to measure the electrochemical performances. The equations below was used to deduce the total specific capacity at different scan rate and specific current.

$$C_d (\text{mAh g}^{-1}) = \frac{\int I dV}{3.6 \cdot S} \quad (3.1)$$

where  $C_d$  is device capacity,  $I$  is the current (A).  $V$  is voltage (V) and  $S$  ( $\text{Vs}^{-1}$ ) is the scan rate

The CV Specific Capacity ( $C_s$ ) is given by:

$$C_s (\text{mAh g}^{-1}) = 4 * \frac{\int I dV}{3.6. S} \quad (3.2)$$

where  $C_s$  is specific capacity,  $I$  is the specific current (A/g).  $V$  is voltage (V) and  $S$  ( $\text{Vs}^{-1}$ ) is the scan rate The GCD Device Capacity ( $Q_D$  or  $Q_C$ ) is calculated according to Laheear et al. [54], the capacity of a system (or electrode) exhibiting battery-like GC/GD curves can be described by the specific discharge capacity  $Q_D$  or the charge capacity  $Q_C$  in  $\text{mAh g}^{-1}$ . These are given by:

$$Q_D (\text{mAh g}^{-1}) = \frac{I t_D}{M_{el} 3.6} \quad (3.3a)$$

and

$$Q_C (\text{mAh g}^{-1}) = \frac{I t_C}{M_{el} 3.6} \quad (3.3b)$$

In electrochemical energy storage, the specific energy  $E_d$  and the specific power denoted  $P_d$  are given by:

$$E_S (\text{Wh Kg}^{-1}) = \frac{1*1000}{8*3600} Q_C V^2 \quad (3.4)$$

or

$$E_S (\text{Wh Kg}^{-1}) = \frac{1*1000}{2*3600} Q_D V^2 \quad (3.5)$$

Where  $E_S$  is the Specific Energy ( $\text{Whkg}^{-1}$ ),  $Q_C$  is the Specific Capacity ( $\text{mA h g}^{-1}$ ),  $Q_D$  is the Device Capacity ( $\text{mA h g}^{-1}$ ), and  $\Delta V$  is the potential window (V).

$$P_d (\text{W Kg}^{-1}) = \frac{E_S}{t} * 3600 \quad (3.6)$$

Where  $P_d$  is the specific power of the device ( $\text{W Kg}^{-1}$ ),  $t$  is the discharge time (s), and  $E_S$  is the specific energy ( $\text{Wh kg}^{-1}$ ).

The CV curves that compares the electrochemical performance of all the samples at a sweep rate of  $50 \text{ mV s}^{-1}$  is presented in fig 3.5 (a). All the curves revealed “battery behaviour,” with oxidation and reduction peaks showing that Faradaic reactions played major roles in the capacitance. From the figure, it is observed that the  $\alpha\text{-Fe}_2\text{O}_3\text{-ACC}$  displayed the highest current response corresponding to a better electrochemical performance. This is due to the existence of dopant groups on the surface of ACC, providing covalent chemical bonds that allows the iron oxide nanoparticles to firmly attach on the ACC, by improving the diffusion length and the electrolyte ions interaction between the  $\text{Fe}_2\text{O}_3$  and the ACC acting as the current collector with enhanced conductivity. Figure 3.5 (b) shows the comparative GCD result for the devices with the different concentration and confirms that the  $\alpha\text{-Fe}_2\text{O}_3\text{-ACC}$  displayed the best electrochemical performance and based on the result further analysis was carried out only on the  $\alpha\text{-Fe}_2\text{O}_3\text{-ACC}$ . Figure 3.5 c presents CV at different scan rate for the  $\alpha\text{-Fe}_2\text{O}_3\text{-ACC}$ , with capacity decreases as the scan rate increases. This suggests an increase in Faradaic reaction activities at lower scan rates, as well as longer durations for ionic motion at low scan rates. It is important to note that the scan rate is a measure of voltage change over time. Therefore, at lower scan rates, the rate of redox potential and electrochemical reaction is faster thereby given rise to higher specific capacity. In contrast, the movement of ions is more limited at higher scan rates. It was also observed that the average area under CV curve was greater at higher scan rates of  $200 \text{ mV s}^{-1}$  than at lower scan rates of  $2 \text{ mV s}^{-1}$ . Similar trend was observed for the GCD as the current increase as shown in fig. 3.5(d). The GCD curves are also non-linear in shape, demonstrating battery-like behaviour, which is in agreement with the CV curves in Fig. 3.5 (a). From the GCD a specific capacity of  $295.56 \text{ mAhg}^{-1}$ ; energy of  $36.94 \text{ WhKg}^{-1}$  and specific Power of  $0.50 \text{ kWKg}^{-1}$  was obtained. The device also demonstrated remarkable cyclic stability at  $1 \text{ Ag}^{-1}$  and a

capacitance retention of 96% after 10,000 cycles. Table 3.2 presents a summary of the electrochemical results obtained for the various material that were prepared in this work. These results are comparable to values available in the literature as presented in table 3.3.

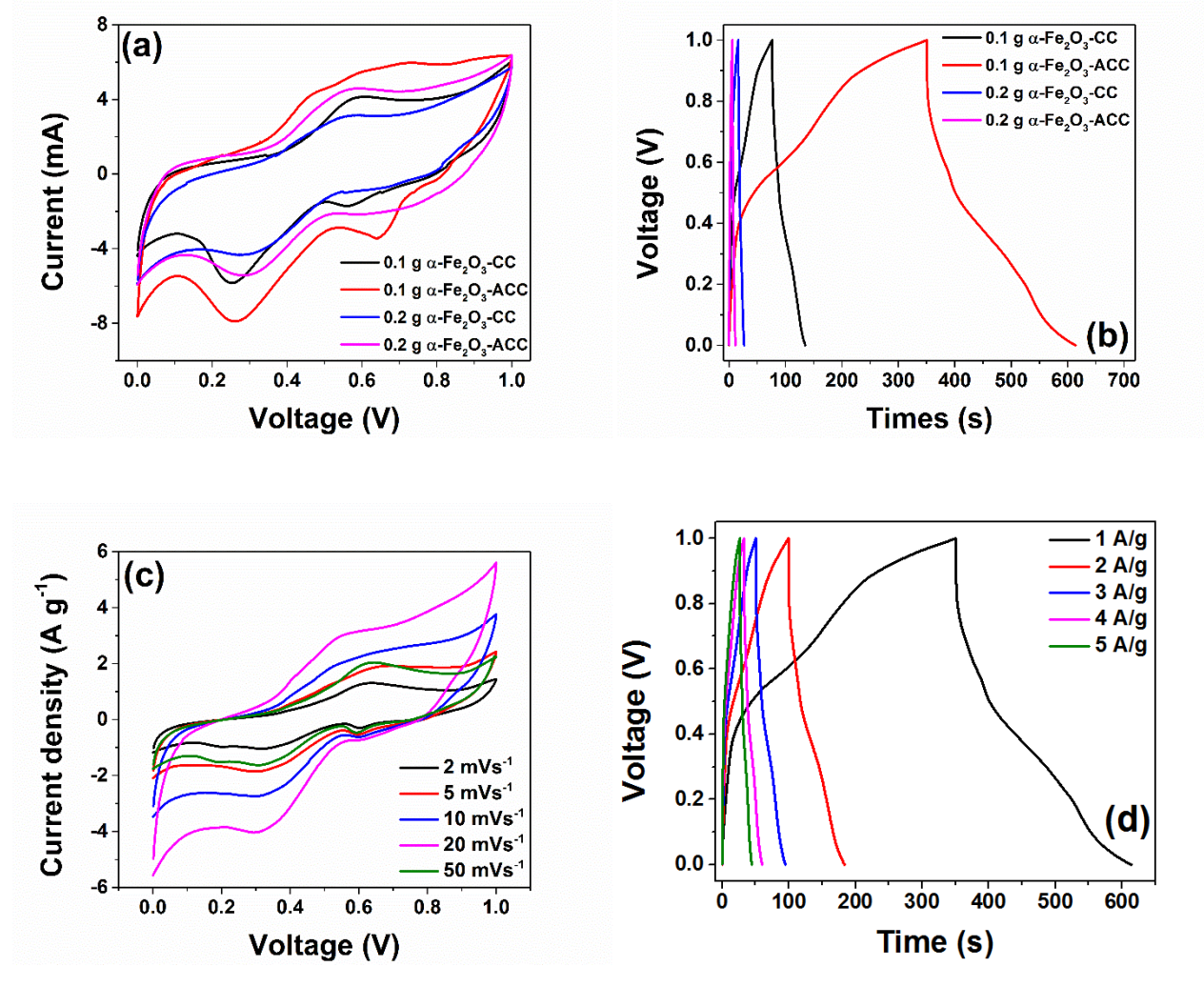


Figure 3.5. Comparison (a) CV and (b) GCD curves of 0.1g  $\alpha\text{-Fe}_2\text{O}_3\text{-CC}$ , 0.1 g  $\alpha\text{-Fe}_2\text{O}_3\text{-ACC}$ , 0.2g  $\alpha\text{-Fe}_2\text{O}_3\text{-CC}$  and 0.2g  $\alpha\text{-Fe}_2\text{O}_3\text{-ACC}$ , (c) CV and (d) at different scan rate and at different specific current for 0.1 g  $\alpha\text{-Fe}_2\text{O}_3\text{-ACC}$ .

Table 3.2. Electrochemical measurements obtained at different mass concentrations

<b>Performance Parameter</b>	<b><math>\alpha</math>-Fe<sub>2</sub>O<sub>3</sub>-CC</b>	<b><math>\alpha</math>-Fe<sub>2</sub>O<sub>3</sub>-CC</b>	<b><math>\alpha</math>-Fe<sub>2</sub>O<sub>3</sub>-CC</b>	<b><math>\alpha</math>-Fe<sub>2</sub>O<sub>3</sub>-CC</b>	<b><math>\alpha</math>-Fe<sub>2</sub>O<sub>3</sub>-CC</b>	<b><math>\alpha</math>-Fe<sub>2</sub>O<sub>3</sub>-ACC</b>	<b><math>\alpha</math>-Fe<sub>2</sub>O<sub>3</sub>-ACC</b>
Mass of FeCl <sub>3</sub> .6H <sub>2</sub> O (g)	0.05	0.1	0.2	0.4	0.8	0.1 g	0.2 g
CV (mAh g <sup>-1</sup> )	-	123.61	108.33	74	59.9	352.2	136.1
GCD (mAh g <sup>-1</sup> )	-	117.78	74.72			295.56	127.8
Areal capacity (mAh cm <sup>-2</sup> )	-	29.4	18.7	-	-	73.9	32
Resistance ( $\Omega$ )	-	0.096	0.124			0.089	0.094

We further carried out the EIS test to understand the behaviour of the various composite electrodes. Figure 3.6 shows the various Nyquist plots, with real and imaginary impedances, as a function of the frequency measured between 100 kHz and 10 mHz. The intercept on the positive axis of the Nyquist plot in the high-frequency region offer evidence about the total resistance of the electrolyte, the contact leads of the Swagelok, the carbon cloth and the Fe<sub>2</sub>O<sub>3</sub> known as the

equivalent series resistance (ESR). The Nyquist plot shows a deviation from the perpendicular line at the low-frequency regime, indicating almost-ideal capacitive behaviour. This represents the diffusion of ions to the interface between electrode and electrolyte [55]. The ESR values obtained from the Nyquist plot are presented in table 3.2 show that the 0.1g  $\alpha$ -Fe<sub>2</sub>O<sub>3</sub>-ACC exhibits the least ESR value of 0.089  $\Omega$  with a better vertical line when compared to the others, which is consistent and due to faster ion diffusion, which enhances charge storage in the electrode materials [55]. Furthermore, it has been reported that the accumulation of dissipated energy is as a result of ESR. Hence, at high values of ESR the energy and power efficiency are severely degraded due to the resistance to the flow of charge [56]. The fitting of the Nyquist data is represented in Fig. 3.6 (b) along with the experimental data for the  $\alpha$ -Fe<sub>2</sub>O<sub>3</sub>-ACC, showing that the Nyquist plot fits perfectly. In the equivalent circuit (inset to the figure), a solution resistance (R<sub>s</sub>) is connected in series with a constant phase element (QCT), and the QCT is connected in parallel with the charge transfer resistance (RCT). The mass capacitance (QL) is also connected in parallel with the leakage current resistance, R<sub>L</sub> are all in series with R<sub>s</sub>. The stability of the device from  $\alpha$ -Fe<sub>2</sub>O<sub>3</sub>-ACC that displayed the best electrochemical performance was carried out at 1 Ag<sub>-1</sub> and the result is presented in Fig. 3.6 (c) a Coulombic efficiency of 96.6% was observed after 10000 cycles revealing an excellent stability electrode material without notable degradation.

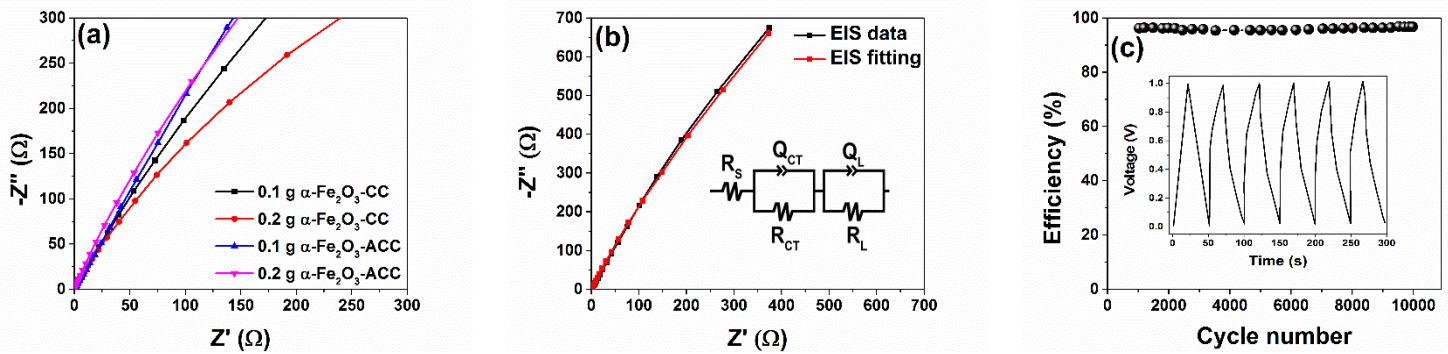


Figure 3.6. EIS plots (a) for all the devices, (b) fitting of the Nyquist data for the  $\alpha$ -Fe<sub>2</sub>O<sub>3</sub>-ACC and (c) Efficiency as a function of the cycle number.

Table 3.3 - Comparison of some Metal Oxide based composite electrodes adapted from [57]

Electrode materials	Specific Current	Capacity	Cycles	Refs. In referred paper [53]
Fe <sub>2</sub> O <sub>3</sub> /graphene/aerogel	100 mA g <sup>-1</sup>	745 mAh g <sup>-1</sup>	100	Meng et al. 2017
Fe <sub>2</sub> O <sub>3</sub> /carbon nanofibers	50 mA g <sup>-1</sup>	518 mAh g <sup>-1</sup>	100	Kobayashi et al. 2018
Co <sub>3</sub> O <sub>4</sub> /CC graphene	100 mA g <sup>-1</sup>	391 mAh g <sup>-1</sup>	300	Xie et al. 2017
FeS@C/CC	91 mA g <sup>-1</sup>	420 mAh g <sup>-1</sup>	100	Wei et al. 2015
TiO <sub>2</sub> /CC	500 mA g <sup>-1</sup>	150 mAh g <sup>-1</sup>	100	Tjandra et al. 2016
Fe <sub>2</sub> O <sub>3</sub> /3D graphene	200 mA g <sup>-1</sup>	864 mAh g <sup>-1</sup>	50	Cao et al. 2014
MoS <sub>2</sub> @ carbon fibers	0.5 mA cm <sup>-2</sup>	5.3 mAh cm <sup>-2</sup>	50	Shan et al. 2018
SnO <sub>2</sub> /CC	0.2 mA	1.85 mAh cm <sup>-2</sup>	100	Xu et al 2017
Fe <sub>2</sub> O <sub>3</sub> /ACC	1000 mA g <sup>-1</sup>	295.56 mAh g <sup>-1</sup>	10,000	This work

			cycles	
--	--	--	--------	--

### 3.6.3. Implications

The results obtained from this work suggests that  $\alpha\text{-Fe}_2\text{O}_3$  processed on activated carbon cloth has potential for applications in flexible supercapacitors with good cycle lives at comparable capacities and specific currents to those of unactivated carbon cloth. Further work is needed to determine the mechanical properties of the layers and nanoparticle structures in the model structures that were examined in this study. This will require multi-scale mechanical property measurements of the adhesion, contact (nanoindentation) and deformation (elastic and plastic) behaviour under different loading conditions (bending, twisting and axial). There is also the need to explore the possible failure (fatigue and fracture) phenomena that can occur in flexible supercapacitors that are deformed under monotonic or cyclic loading conditions. These are clearly some of the challenges for future work.

### 3.6.4. Summary and Concluding Remarks

The  $\alpha\text{-Fe}_2\text{O}_3$  nanoparticles were grown on carbon cloth and activated carbon cloth using a hydrothermal method. The resulting flexible cloths were integrated into binder-free symmetric supercapacitor electrodes for potential applications in electrochemical energy storage systems. The activation of the carbon cloths and ACC structures resulted in supercapacitors with attractive combinations of high Specific Capacity (up to  $295.56 \text{ mAhg}^{-1}$ ), Specific Energy (up to  $36.94 \text{ Whkg}^{-1}$ ), Specific Power (up to  $0.5 \text{ kWKg}^{-1}$ ), and excellent cyclic stability. The activation of the carbon cloth contributed to a more conductive interactions with the  $\alpha\text{-Fe}_2\text{O}_3$ , making it a more suitable electrode material. These combinations of energy storage characteristics suggest that  $\alpha\text{-Fe}_2\text{O}_3$  nanoparticle-activated carbon cloths are promising structures for future applications in the

electrodes of flexible supercapacitor structures. However, further work is needed to study the robustness of the  $\alpha$ -Fe<sub>2</sub>O<sub>3</sub> nanoparticle-coated ACC structures under flexural loading conditions that can induce damage under service conditions. These are clearly some of the challenges for future work.

## REFERENCES

- [1] M. Beidaghi, Y. Gogotsi, Capacitive energy storage in micro-scale devices: recent advances in design and fabrication of micro-supercapacitors, *Energy Environ. Sci.* 7 (2014) 867.
- [2] D. Ge, L. Yang, L. Fan, C. Zhang, X. Xiao, Foldable supercapacitors from triple networks of macroporous cellulose fibers, single-walled carbon nanotubes and polyaniline nanoribbons, *Nano Energy.* (2014).
- [3] Z.L. C.J. Zhang, S.-H. Park, O. Ronan, A. Harvey, A. Seral-Ascaso, Enabling Flexible Heterostructures for Li-Ion Battery Anodes Based on Nanotube and Liquid-Phase Exfoliated 2D Gallium Chalcogenide Nanosheet Colloidal Solutions, *Small.* 13 (2017) 1–11.
- [4] V.T. P. Huang, C. Lethien, S. Pinaud, K. Brousse, R. Laloo, On-chip and freestanding elastic carbon films for micro-supercapacitors, *Science* 80 (2016) 3717–3720.

- [5] Z. Liu, Z.-S. Wu, S. Yang, R. Dong, X. Feng, K. Müllen, Ultraflexible In-Plane Micro-Supercapacitors by Direct Printing of Solution-Processable Electrochemically Exfoliated Graphene, *Adv. Mater.* 28 (2016) 2217–2222.
- [6] P. Simon, Y. Gogotsi, Materials for electrochemical capacitors, *Nat. Mater.* 7 (2008) 845–854.
- [7] K.X. L. Suo, O. Borodin, T. Gao, M. Olguin, J. Ho, X. Fan, C. Luo, C. Wang, “ Water-in-salt ” electrolyte enables high-voltage aqueous lithium-ion chemistries, *Science* 80 (2015) 938-943.
- [8] L.-Q. Fan, Q.-M. Tu, C.-L. Geng, Y.-L. Wang, S.-J. Sun, Y.-F. Huang, et al., Improved redox-active ionic liquid-based ionogel electrolyte by introducing carbon nanotubes for application in all-solid-state supercapacitors, *Int. J. Hydrogen Energy.* 45 (2020) 17131-17139.
- [9] L.-Q. Fan, Q.-M. Tu, C.-L. Geng, J.-L. Huang, Y. Gu, J.-M. Lin, et al., High energy density and low self-discharge of a quasi-solid-state supercapacitor with carbon nanotubes incorporated redox-active ionic liquid-based gel polymer electrolyte, *Electrochim. Acta.* 331 (2020) 135425.
- [10] Z. Song, H. Duan, L. Miao, L. Ruhlmann, Y. Lv, W. Xiong, et al., Carbon hydrangeas with typical ionic liquid matched pores for advanced supercapacitors, *Carbon* 168 (2020) 499–507.
- [11] J. Yan, L. Miao, H. Duan, D. Zhu, Y. Lv, W. Xiong, et al., Core-shell hierarchical porous carbon spheres with N/O doping for efficient energy storage, *Electrochim. Acta.* (2020) 136899.

- [12] Z.-S. Wu, D.-W. Wang, W. Ren, J. Zhao, G. Zhou, F. Li, et al., Anchoring Hydrous RuO<sub>2</sub> on Graphene Sheets for High-Performance Electrochemical Capacitors, *Adv. Funct. Mater.* 20 (2010) 3595–3602.
- [13] W. Wei, X. Cui, W. Chen, D.G. Ivey, Manganese oxide-based materials as electrochemical supercapacitor electrodes., *Chem. Soc. Rev.* 40 (2011) 1697–721.
- [14] X.-C.C. Dong, H. Xu, X.-W.W. Wang, Y.-X.X. Huang, M.B. Chan-Park, H. Zhang, et al., 3D graphene-cobalt oxide electrode for high-performance supercapacitor and enzymeless glucose detection., *ACS Nano.* 6 (2012) 3206–13.
- [15] S.K. Meher, G.R. Rao, Effect of microwave on the nanowire morphology, optical, magnetic, and pseudocapacitance behavior of Co<sub>3</sub>O<sub>4</sub>, *J. Phys. Chem. C.* 115 (2011) 25543–25556.
- [16] A. Bello, K. Makgopa, M. Fabiane, D. Dodoo-Ahrin, K.I.I. Ozoemena, N. Manyala, Chemical adsorption of NiO nanostructures on nickel foam-graphene for supercapacitor applications, *J. Mater. Sci.* 48 (2013) 6706–6712.
- [17] D. Wang, W. Ni, H. Pang, Q. Lu, Z. Huang, J. Zhao, Preparation of mesoporous NiO with a bimodal pore size distribution and application in electrochemical capacitors, *Electrochim. Acta.* 55 (2010) 6830–6835.
- [18] N. Nagarajan, I. Zhitomirsky, Cathodic electrosynthesis of iron oxide films for electrochemical supercapacitors, *J. Appl. Electrochem.* 36 (2006) 1399–1405.
- [19] X. Lu, G. Wang, T. Zhai, M. Yu, J. Gan, Y. Tong, et al., Hydrogenated TiO<sub>2</sub> nanotube arrays for supercapacitors., *Nano Lett.* 12 (2012) 1690–6. doi:10.1021/nl300173j.

- [20] S.D. Perera, B. Patel, N. Nijem, K. Roodenko, O. Seitz, J.P. Ferraris, et al., Vanadium Oxide Nanowire-Carbon Nanotube Binder-Free Flexible Electrodes for Supercapacitors, *Adv. Energy Mater.* 1 (2011) 936–945.
- [21] J.W.L. M.B. Sassin, A.N. Mansour, K.A. Pettigrew, D.R. Rolison, Electroless Deposition of Conformal Nanoscale Iron Oxide on Carbon Charge Storage, *ACS Nano.* 4 (2010) 4505–4514.
- [22] B.L. F. Zhang, H. Yang, X. Xie, L. Li, L. Zhang, J. Yu, H. Zhao, Controlled synthesis and gas-sensing properties of hollow sea urchin-like  $\alpha$ -Fe<sub>2</sub>O<sub>3</sub> nanostructures and  $\alpha$ -Fe<sub>2</sub>O<sub>3</sub> nanocubes, *Sensors Actuators B Chem.* 141 (2009) 381–389.
- [23] K.J. A. Mirzaei, B. Hashemi,  $\alpha$ -Fe<sub>2</sub>O<sub>3</sub> based nanomaterials as gas sensors, *J. Mater. Sci. Mater. Electron.* 27 (2016) 3109–3144..
- [24] X.C. H. Shan, C. Liu, L. Liu, L. Wang, S. Li, X. Zhang, X. Bo, Synthesis and acetone gas sensing properties of  $\alpha$ -Fe<sub>2</sub>O<sub>3</sub> nanotubes, *Sci. China Chem.* 56 (2013) 1722–1726.
- [25] M. Sevilla, A.B. Fuertes, Direct Synthesis of Highly Porous Interconnected Carbon Nanosheets and Their Application as High-Performance Supercapacitors, *ACS Nano.* 8 (2014) 5069–5078.
- [26] M. Biswal, A. Banerjee, M. Deo, S. Ogale, From dead leaves to high energy density supercapacitors, *Energy Environ. Sci.* 6 (2013) 1249–1259.
- [27] L. Miao, Z. Song, D. Zhu, L. Li, L. Gan, M. Liu, Recent advances in carbon-based supercapacitors, *Mater. Adv.* (2020).

- [28] Y. Korenblit, M. Rose, E. Kockrick, L. Borchardt, A. Kvit, S. Kaskel, et al., High-rate electrochemical capacitors based on ordered mesoporous silicon carbide-derived carbon, *ACS Nano*. 4 (2010) 1337–1344.
- [29] V. Presser, M. Heon, Y. Gogotsi, Carbide-Derived Carbons-From Porous Networks to Nanotubes and Graphene, *Adv. Funct. Mater.* 21 (2011) 810–833.
- [30] B.G. Choi, M. Yang, W.H. Hong, J.W. Choi, Y.S. Huh, 3D macroporous graphene frameworks for supercapacitors with high energy and power densities, *ACS Nano*. 6 (2012) 4020–4028.
- [31] L.L. Zhang, R. Zhou, X.S. Zhao, Graphene-based materials as supercapacitor electrodes, *J. Mater. Chem.* 20 (2010) 5983–5992.
- [32] P. Simon, Y. Gogotsi, Capacitive energy storage in nanostructured carbon–electrolyte systems, *Acc. Chem. Res.* 46 (2012) 1094–1103.
- [33] Y. Gao, Y.S. Zhou, M. Qian, X.N. He, J. Redepenning, P. Goodman, et al., Chemical activation of carbon nano-onions for high-rate supercapacitor electrodes, *Carbon* 51 (2013) 52–58.
- [34] M. Kubota, A. Hata, H. Matsuda, Preparation of activated carbon from phenolic resin by KOH chemical activation under microwave heating, *Carbon* 47 (2009) 2805–2811.
- [35] S. Dörfler, I. Felhösi, T. Marek, S. Thieme, H. Althues, L. Nyikos, et al., High power supercap electrodes based on vertical aligned carbon nanotubes on aluminum, *J. Power Sources*. 227 (2013) 218–228.

- [36] E. Iyyamperumal, S. Wang, L. Dai, Vertically aligned BCN nanotubes with high capacitance, *ACS Nano*. 6 (2012) 5259–5265.
- [37] F.B. E. Frackowiak, E. Frackowiak, F. Beguin, F. Béguin, Carbon materials for the electrochemical storage of energy in capacitors, *Carbon* 39 (2001) 937–950.
- [38] Y. Ye, H. Zhang, Y. Chen, P. Deng, Z. Huang, L. Liu, Core – shell structure carbon coated ferric oxide (  $\text{Fe}_2\text{O}_3@C$  ) nanoparticles for supercapacitors with superior electrochemical performance, *J. Alloys Compd.* 639 (2015) 422–427.
- [39] M. Nasibi, M.A. Golozar, G. Rashed, Nano iron oxide ( $\text{Fe}_2\text{O}_3$ )/carbon black electrodes for electrochemical capacitors, *Mater. Lett.* 85 (2012) 40–43.
- [40] Y. Li, L. Kang, G. Bai, P. Li, J. Deng, X. Liu, et al., Solvothermal synthesis of  $\text{Fe}_2\text{O}_3$  loaded activated carbon as electrode materials for high-performance electrochemical capacitors, *Electrochim. Acta*. 134 (2014) 67–75.
- [41] P. Luo, J. Yu, Z. Shi, F. Wang, L. Liu, H. Huang, et al., Fabrication and supercapacitive properties of  $\text{Fe}_2\text{O}_3@C$  nanocomposites, *Mater. Lett.* 80 (2012) 121–123.
- [42] J. Li, Y. Wang, W. Xu, Y. Wang, B. Zhang, S. Luo, et al., Porous  $\text{Fe}_2\text{O}_3$  nanospheres anchored on activated carbon cloth for high-performance symmetric supercapacitors, *Nano Energy*. 57 (2019) 379–387.
- [43] Y.T. K.P.O. Mahesh, I. Shown, L. C. Chen, K. H. Chen, *Applied Surface Science* Flexible sensor for dopamine detection fabricated by the direct growth of  $\alpha\text{-Fe}_2\text{O}_3$  nanoparticles on carbon cloth, *Appl. Surf. Sci.* 427 (2018) 387–395.

- [44] X.W. Q. Xiong, J. Tu, X. Xia, X. Zhao, C. Gu, A three-dimensional hierarchical Fe<sub>2</sub>O<sub>3</sub>@NiO core/shell nanorod array on carbon cloth: a new class of anode for high-performance lithium-ion batteries, *Nanoscale*. 5 (2013) 7906–7912.
- [45] A. Bello, F. Barzegar, D. Momodu, J. Dangbegnon, F. Taghizadeh, N. Manyala, Symmetric supercapacitors based on porous 3D interconnected carbon framework, *Electrochim. Acta*. 151 (2015) 386–392.
- [46] T. Yamashita, P. Hayes, Analysis of XPS spectra of Fe<sup>2+</sup> and Fe<sup>3+</sup> ions in oxide materials, *Appl. Surf. Sci.* 254 (2008) 2441–2449.
- [47] S. Karamat, R.S. Rawat, P. Lee, T.L. Tan, R. V Ramanujan, Structural, elemental, optical and magnetic study of Fe doped ZnO and impurity phase formation, *Prog. Nat. Sci. Mater. Int.* 24 (2014) 142–149.
- [48] M. Mullet, V. Khare, C. Ruby, XPS study of Fe (II)□ Fe (III)(oxy) hydroxycarbonate green rust compounds, *Surf. Interface Anal. An Int. J. Devoted to Dev. Appl. Tech. Anal. Surfaces, Interfaces Thin Film*. 40 (2008) 323–328.
- [49] M.P. Bichat, E. Raymundo-Piñero, F. Béguin, High voltage supercapacitor built with seaweed carbons in neutral aqueous electrolyte, *Carbon* 48 (2010) 4351–4361.
- [50] M. Gazicki, W.J. James, H.K. Yasuda, Colloids and Surfaces A: Physicochemical and Engineering Aspects, *J. Polym. Sci. Lett. Polym. Ed.* 23 (1985) 639–645.
- [51] P.M. Jayaweera, E.L. Quah, H. Idriss, Photoreaction of ethanol on TiO<sub>2</sub> (110) single-crystal surface, *J. Phys. Chem. C*. 111 (2007) 1764–1769.

- [52] U. Gelius, P.F. Heden, J. Hedman, B.J. Lindberg, R. Manne, R. Nordberg, et al., Molecular spectroscopy by means of ESCA III. Carbon compounds, *Phys. Scr.* 2 (1970) 70.
- [53] B. Lamontagne, F. Semond, D. Roy, K overlayer oxidation studied by XPS: the effects of the adsorption and oxidation conditions, *Surf. Sci.* 327 (1995) 371–378.
- [54] A. Laheäär, P. Przygocki, Q. Abbas, F. Béguin, *Electrochemistry Communications* Appropriate methods for evaluating the efficiency and capacitive behavior of different types of supercapacitors, 60 (2015) 21–25.
- [55] F. Barzegar, A. Bello, O.O. Fashedemi, J.K. Dangbegnon, D.Y. Momodu, F. Taghizadeh, et al., Synthesis of 3D porous carbon based on cheap polymers and graphene foam for high-performance electrochemical capacitors, *Electrochim. Acta.* 180 (2015) 442–450.
- [56] A. Bello, D.M. Sanni, S.A. Adeniji, V. Anye, K. Orisekeh, M. Kigozi, et al., Combustion synthesis of battery-type positive electrodes for robust aqueous hybrid supercapacitor, *J. Energy Storage.* 27 (2020) 101160.
- [57] J. Shao, H. Zhou, M. Zhu, Carbon cloth – supported  $\text{Fe}_2\text{O}_3$  derived from Prussian blue as self-standing anodes for high-performance lithium-ion batteries, *J. Nanopart Res.* (2019) 1–11.

## CHAPTER FOUR

### **4.0. Mechanical Properties of Polyvinyl Pyrrolidone /Polyvinyl Alcohol-based Solid Electrolytes**

#### 4.1. Introduction

The worldwide trend in the continuous demand and efficient use of renewable technologies especially in portable electronic devices, the rapid development and expansion of the electric vehicle market in the last decade signals the importance of energy storage technologies, particularly lithium-ion batteries (LiBs). The conventional LiBs use liquid electrolytes and plays a major role in the market. However, there are significant fire and explosion risks that are associated with the chemical instability of liquid electrolytes e.g. due to the presence of carbonates that are highly volatile and flammable [1], [2].

Solid electrolytes (SEs) offer promising and viable alternatives that reduce the safety risks associated with the use of liquid electrolytes. Amongst all SEs, polymer based SEs are preferred

because of their low flammability, good flexibility, excellent thermal stability, and high safety. According to Baranowski et al. [1], the SE phase support Li metal anode utilization, and results in high specific capacity (3860 mA h/g), low density (0.59 g/cm<sup>3</sup>), with negative voltaic cell (−3.040 V vs the standard hydrogen electrode), ultimately leading to lighter weight and the increased range of electrical vehicles.

Although prior research efforts [3], [4] have shown that solid polymer-based electrolytes enhance electrochemical performance, the relatively low ionic conductivities and poor mechanical properties of SEs still remain a major challenge that must be overcome. In order to address these challenges and enhance the performance of SEs, several composites (reinforced with particles) have been explored as electrolytes in polymer-based blends [5][6]. Nevertheless, there have been only limited studies of the mechanical properties of polymer-based solid electrolytes. Hence, in this work, we will focus on the mechanical properties of a PVA/PVP/LiClO<sub>4</sub> solid polymer blend, with the aim of addressing this knowledge gap. It is important to study the mechanical properties of solid state electrolyte to give an understanding of the behavior of the blends to applied load.

The quest for novel solid polymer electrolytes (SPEs) has evolved into the use of polymers such as polyvinyl alcohol (PVA), polyvinylpyrrolidone (PVP), polyethylene glycol (PEG), polyacrylonitrile (PAN), polyethylene oxide (PEO) and polyvinylidene fluoride (PVdF) in energy storage. [7]. For example, a bio-component polymer membrane based on PAN-co-PVAc/PVA for immobilization of enzymes was reported by Sandu et al. [8]. Ebrasu et al. [9], motivated by fuel cell applications, reported a conducting polymer PAN doped with nanoparticles of SiO<sub>2</sub>. Yahya et al. [10] reported a lithium ion conductivity of  $\sim 10^{-5}$  S cm<sup>-1</sup> using plasticizer based on chitosan lithium acetate electrolyte. Ismail et al [11] reported that

lithium acetate salt mixed with PEO polymer matrix improves the conductivity of the polymer electrolyte to  $\sim 10^{-6} \text{ S cm}^{-1}$ . Sundaramahalingam et al. [7] noted that “most of the industries uses poly (vinyl alcohol) (PVA) as an effective polymer matrix to achieve the desired properties” while Abdelrazek et al. [12] doped PVA with phosphoric acid and applied it as electrolyte in solid-state photocells and solid-state electrochromic displays.

In this work, we explore the development of SE using a mixture of host polymers of PVP, PVA and lithium perchlorate ( $\text{LiClO}_4$ ) integrated into flexible and light-weight transparent films. The mechanical properties of the films are studied using nanoindentation techniques and statistical deconvolution mapping, tensile tests and fracture toughness measurements. PVP was chosen due to its attractive combination of mechanical properties and its potential role as a hydrophobicizer [13], [14]. Furthermore, PVP can be easily processed to have high thermal conductivity, good water absorption, and environmental stability, it is also known for its ability to form a good matrix [15]–[19]. Reddy et al. [6], [20] reported the development of a SE by using PVP +  $\text{AgNO}_3$  and PVP +  $\text{NaNO}_3$  for the fabrication of thin-film electrochemical cell. Zidan et al. [21] reported that increasing the level of PVP can help to decrease the crystallinity of PVA, such that the matrix of PVP and PVA could be suited for film formation leading to extra disorder at different ratios because of the presence of hydroxyl group of PVA and carbonyl group of PVP.

Similarly, PVA is a semi-crystalline polymer with unique physical characteristics due to their crystal-amorphous interfacial effects [22], [23]. PVA polymer is nontoxic and biodegradable with the presence of OH- bonding groups between carbon chain backbone molecules. [13], [24], [25]. These polymers (PVP/PVA) can be mixed together so that the mechanical properties of the polymer matrix can be improved. The ratio of polymer blend and cation in solution is very key to obtaining the good mechanical properties, stability and high conductivity of the solid electrolyte.

Sundaramahalingam et al.,[7] reported a composition of 50 % PVA/50 % PVP as having high stability as well as high conductivity. Likewise, Rajeswari et al. [26] also investigate the same materials compositions and report similar findings.

Lithium perchlorate ( $\text{LiClO}_4$ ), is a low-cost lithium salt and is found to be soluble in most of the solvents [14] so that the blend of polymer electrolytes based on PVP and  $\text{LiClO}_4$  were prepared to improve the ionic conductivity resulting in increased basicity of the C=O group as a result of the donation of the lone pair electrons of the N-atom from the PVP polymer. This interaction results in a complex bond of  $\text{Li}^+\dots\text{C}=\text{O}$  which comprises the primary complex bond of  $\text{Li}^+\dots\text{C}=\text{O}$  and the secondary where  $\text{Li}^+$  loosely complexes with many C=O groups concurrently. If the ratio of Li:O is higher than 0.281 and the  $\text{ClO}_4^-$  anion is free in the diluted PVP/ $\text{LiClO}_4$  electrolyte then we have dominance of the secondary complex. [14]

According to Baranowski et al. [1], using a technique known as bulk and microscale to investigate the mechanical response of  $\beta\text{-Li}_3\text{PS}_4$ . This led to the development of a strong testing protocol for this porous ceramic material and ultimately resulted in bulk modulus of 80 % dense  $\beta\text{-Li}_3\text{PS}_4$  to be 10–12 GPa, and predicted a value of 16 GPa for the 100 % dense material. After investigating the mechanical properties of solid Li-conducting electrolytes, they stated that the most principal property in the evaluation of dendrite growth is not shear modulus, but suggested fracture toughness and fatigue response could be investigated to relate the battery performance to the mechanical properties of the electrolyte.

Yu et al. [27] studied the elastic behaviour of the solid electrolyte  $\text{Li}_7\text{La}_3\text{Zr}_2\text{O}_{12}$  (LLZO) using a mixture of first-principles calculations, acoustic impulse excitation measurements, and nanoindentation experiments to ascertain the elastic constants and moduli for high-conductivity

LLZO constituents based on Al and Ta-doping. According to their report, there is good agreement between the calculated isotropic shear moduli values of 56 to 61 GPa. Insun Yoon et al. [28] also carried out mechanical tests to measure the fracture properties of the solid electrolyte interphase (SEI) on lithium metal anodes in lithium ion batteries. These are made up of electrolyte additives, such as ethylene carbonate (EC) and fluoroethylene carbonate (FEC). Atomic force microscopy (AFM) and membrane-bulge configurations were then combined to determine the stress-strain behaviour of SEI, as well as the onset of inelastic response and the initiation of fracture in the two different electrolytes (1.2 M LiPF<sub>6</sub> in EC and 1.2 M LiPF<sub>6</sub> in EC/FEC (8:2). This was used to study the effects of the FEC additive). They reported ~240 MPa for the plane strain elastic modulus of SEIEC and that of SEIEC + FEC was measured to be ~ 430 MPa. Similarly, the residual stress and the elastic limit of SEIEC were determined to be ~ 4.5 MPa and 9 MPa, respectively, while the corresponding values for SEIEC + FEC were determined to be ~3.9 MPa and 9 MPa. The mechanical properties of solid-state electrolyte (SSE) have also been shown to have a major effect on the performance of energy storage systems. [28]–[34]

Yan et al. [35] have used depth-controlled indentation mapping tests to study the mechanical properties of the solid electrolyte material (Li<sub>1.3</sub>A<sub>10.3</sub>Ti<sub>1.7</sub>(PO<sub>4</sub>)<sub>3</sub>) {LATP} along different loading axes. The nanoindentation surface profiles were studied after the indentation of the ceramic electrolyte (with a rhombohedral crystal structure). The Young's moduli and hardness values (calculated using the Vlassak-Nix model [35]) were compared with experimentally determined Young's moduli and hardness values, which are functions of the rotation angle from the basal plane to the prismatic plane. The experimental results were in good agreement with the

predictions from the model. However, there were slight differences between the extreme value of 118–177 GPa (obtained for the model) and the experimental results of 114–160 GPa [35].

Fincher et al [36] have also studied the mechanical properties of metallic lithium. The scope of their work ranges from the nano- to the macro-scale, using nanoindentation measurements and bulk tensile testing. They reported that bulk Li has a yield strength between 0.57 and 1.26 MPa, for strain rates between  $5 \times 10^{-4} \text{ s}^{-1}$  and  $5 \times 10^{-1} \text{ s}^{-1}$ . They also reported a decrease in the hardness from 43 MPa to 7.5 MPa, as the indentation depth increases from 250 nm to 10  $\mu\text{m}$ , in the case of indentation tests with loading  $\dot{P}/P = 0.05 \text{ s}^{-1}$ . The plastic properties also have stress exponents of  $n = 6.55$  and  $6.9$ , respectively, for strain-rate dependencies measured using bulk and nanoindentation tests.

However, to the best of our knowledge, there has been no prior work on the mechanical properties of PVA/PVP/LiClO<sub>4</sub> polymer-based solid electrolytes that are being considered for potential applications in charge storage. Thus, the major objective of this work is to study the mechanical properties of PVA/PVP/LiClO<sub>4</sub> polymer-based SEs. This will be done using a combination of tensile, nanoindentation and fracture toughness measurements to determine the strength, Young's moduli, hardness, and fracture toughness values of solid blends of PVP/PVA and Lithium perchlorate salt. The Oliver and Pharr method [37], [38] will be used to study the spatial variations in the local mechanical properties. These will then be analyzed using statistical deconvolution techniques that will be used to extract the mechanical properties of the materials in the composite blends [32], [39]–[42]. Finally, the fracture mechanism and the crack/microstructure interactions associated with the fracture of the blends will be elucidated before discussing the implications of the current work for the design of mechanically robust PVA/PVP/LiClO<sub>4</sub> polymer-based solid electrolyte.

### 4.1.1. Theory

Mechanical properties of materials are often estimated using a nanoindentation technique. The process involves loading the materials under the tip of a nanoindenter before holding the load until plastic deformation occurs. Figure 1 [47-49] presents the schematics of the three stages (load, hold and unload) of the indentation process. Prior reports have shown the use of energy analysis of nanoindentation load-displacement data [28], [44]–[46]. However, we are not aware of prior efforts to use the nanoindentation technique to study the fracture toughness of polymer blends.

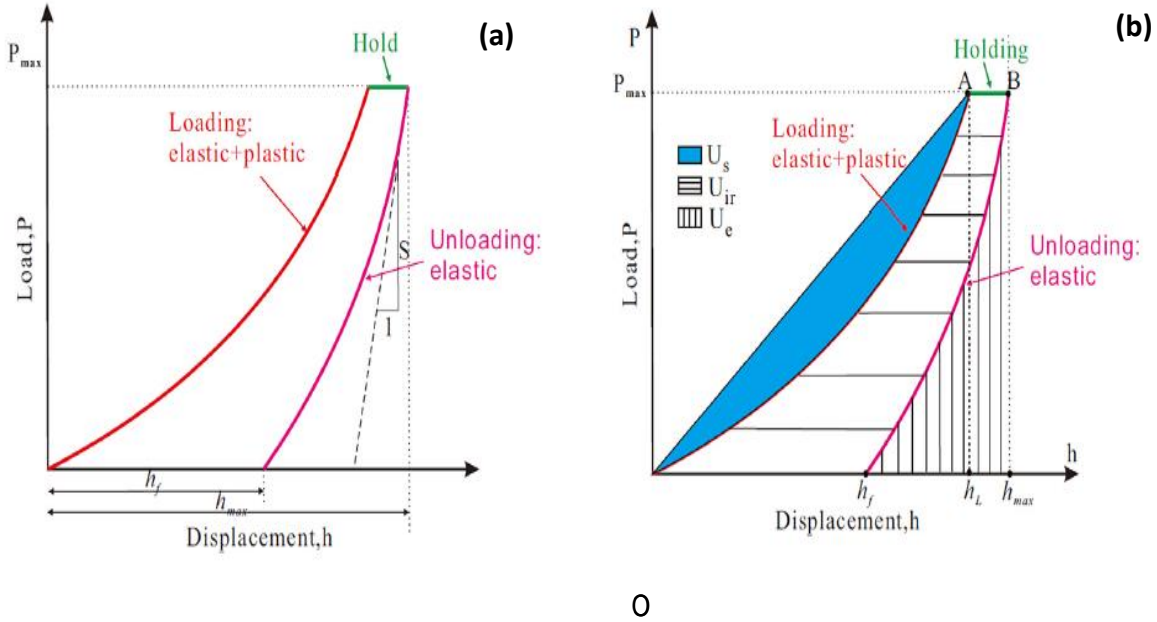


**Figure 4.1.** (a) Sketch of Indentation load-displacement curve. [47], [48] (b) Energy release rate sketch for ease of calculation. [48], [49]

From Figure 4.1a, we can define the contact stiffness by:

$$S = 0.75 * (2V_E - 1) \frac{P_{max}}{h_{max}} \quad (4.1)$$

Where,  $S$  is the contact stiffness,  $P_{max}$  is the maximum indentation load,  $V_E$  is the elastic energy ratio,  $h_{max}$  is the maximum displacement, which is the sum of the contact depth,  $h_c$  and the displacement of the vertical surface,  $h_s$

$$h_{max} = h_s + h_c \quad (4.2)$$

The displacement,  $h_s$ , is given by:

$$h_s = \varepsilon \frac{P_{max}}{S}, \varepsilon = 0.75 \quad (4.3)$$

Where  $P_{max}$  is the maximum indentation load,  $S$  is the contact stiffness,  $\varepsilon$  is a constant given as 0.75 and  $h_c$  is the contact depth, which is given by:

$$h_c = \frac{2(V_E - 1)}{(2V_E - 1)} h_{max} \quad (4.4)$$

The hardness is given by:

$$H = \frac{P_{max}}{A_c} \quad (4.5)$$

where  $P_{max}$  is the maximum indentation load and  $A_c$  is the contact area, which is given by:

$$A_c = 24.5h_c^2 \quad (4.6)$$

$$\frac{1}{E_r} = \frac{1 - \nu^2}{E} + \frac{1 - \nu_i^2}{E_i} \quad (4.7)$$

where,  $E_r$  is the reduced modulus (GPa),  $E_i$  is the elastic modulus of the Berkovich indenter (GPa),  $E$  is the Young's modulus (Pa),  $\nu$  is the Poisson's ratio of the polymer,  $\nu_i$  is the Poisson's ratio of the Berkovich indenter

Finally, the reduced Young's moduli is given by [38]:

$$E_r = \frac{\sqrt[5]{2}}{2\sqrt{A_c}} \quad (GPa) \quad (4.8)$$

According to Cheng et al. [50], the irreversible energy ( $U_{ir}$ ) is the difference between the elastic energy ( $U_e$ ) and the total energy ( $U_t$ ) which is illustrated in Figure 1b

Therefore, the fracture energy ( $U_{crack}$ ) is given by:

$$U_{crack} = U_{ir} - U_{pp} \quad (4.9)$$

where  $U_{pp}$  (J) is the plastic energy, which is given by:

$$\frac{U_{pp}}{U_t} = 1 - \left[ \frac{1 - 3\left(\frac{h_f}{h_{max}}\right)^2 + 2\left(\frac{h_f}{h_{max}}\right)^3}{1 - \left(\frac{h_f}{h_m}\right)^2} \right] \quad (4.10)$$

$U_s$  is the absolute work (Area OAh<sub>1</sub>O) and  $U_{ir}$  is the Irreversible energy work (Area OABh<sub>max</sub>O)

$$U_e = \frac{U_s}{V_E} \quad (\text{Area } h_f B h_{max} h_f) \quad (4.11)$$

where  $V_E$  is the elastic energy ratio and  $U_t$  is the total energy

The critical energy release rate ( $G_c$ ) is given by:

$$G_c = \frac{U_{crack}}{A_m} \quad (4.12)$$

$$A_m = 24.5h_{max}^2 \quad (\text{Which is the maximum crack area for Berkovich indenter}) \quad (4.13)$$

Therefore, the fracture toughness can be given by:

$$K_c = \sqrt{G_c \times E_r} \quad (4.14)$$

$$K_{IC} = \frac{P}{B\sqrt{w}} \left\{ \frac{\sqrt{2 \tan \left[ \frac{\pi a}{2w} \right]}}{\cos \left[ \frac{\pi a}{2w} \right]} \left[ 0.752 + 2.02 \left[ \frac{a}{w} \right] + 0.37 \left[ 1 - \sin \left[ \frac{\pi a}{2w} \right] \right]^3 \right] \right\} \quad (4.15)$$

where  $K_{IC}$  is the Fracture Toughness, P is the Force, a is the notch length, w is the width of the material while B is the Thickness of the material

## 4.2. Materials and Methods

### 4.2.1. Materials

The chemicals and reagents were of analytical grade and used as received without any further purification. The Poly {Vinyl alcohol} (PVA) with Mw 89,000 – 98,000 g/mol (99+ % hydrolyzed), Polyvinylpyrrolidone (PVP) with Mw 55,000 g/mol, and Lithium perchlorate ( $\text{LiClO}_4$ ) salt were all purchased from Sigma-Aldrich Company, St. Louis, Missouri, USA. Distilled water was used for the preparation of the samples.

### 4.2.2. Preparation of the Solid Polymer Blend

PVA, PVP and lithium perchlorate were prepared according to [7] with some modifications. 0.5 g of PVA and 0.5 g of PVP were dissolved in 25 g of distilled water separately which constitute 2wt.% of each solution. Afterwards, x g of lithium perchlorate ( $x = 0.1, 0.2, 0.3, 0.4$  and  $0.5$ ) dissolved in 10 g of distilled water which are made up of various compositions of 1wt%, 2wt%, 3wt%, 4wt% and 5wt% respectively. First, the PVA precursor was measured in a beaker and distilled water was added appropriately. Distilled water was used as a preferred choice of solvent

for the polymers dissolution to avoid introducing counter ion effect in using other solvents like dimethyl sulfoxide (DMSO) and Dimethylformamide (DMF).

The mixture was heated at 90 °C with stirring at 350 rpm for 1 h and continued stirring without heat at 350 rpm for 4 h to obtain a homogeneous transparent solution. Similarly, PVP and lithium acetate solutions were prepared separately following the same procedure for the PVA without heating. Each of the solutions prepared were mixed and stirred for 24 h to obtain a homogeneous solution. Finally, the solution was then poured into a polypropylene dish and dried at ambient. The flexible uniform and transparent films obtained was kept in a desiccator after drying for further characterization. Figure 1 (a) shows a picture of one of the obtained transparent and uniform films while Figure 1 (b) shows the 3-D design with Solid works software (LULZBOT TAZ 6, Fargo, North Dakota USA).

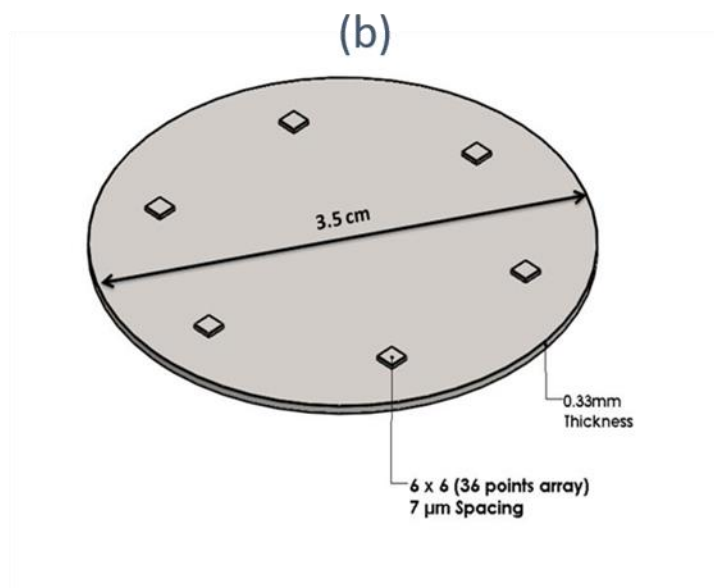
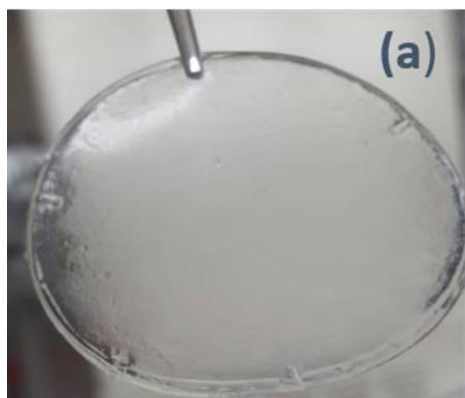


Figure 4.2.. (a) Flexible transparent film and (b) 3-D design of flexible film with Solid works software

#### 4.3. Tensile Tests

Tensile tests were carried out on both the bare PVA-PVP and doped films using Servohydraulic Instron machine (Instron 8872, Instron, Norwood, MA, USA) which was instrumented with a 10 N load cell. The tensile tests were carried out on dog-bone specimens (Figure 4.2a) that were deformed at a crosshead speed that corresponds to a strain rate of  $4 \times 10^{-2} \text{ s}^{-1}$ .

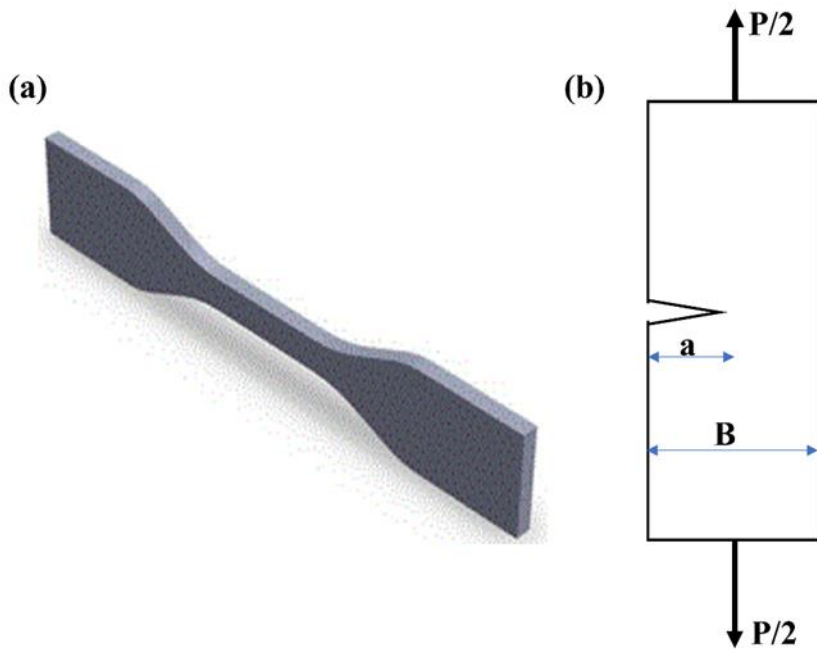


Figure 4.3. (a) Dog-Bone specimen (b) Schematics diagram of single edge notched specimen under tension

##### 4.3.1. Fracture Tests

To estimate the fracture toughness of the flexible polymer blend, we carried out fracture tests on a single edge notched specimen under tension using Instron testing machine (Instron 68SC-1,

Norwood, MA, USA). Figure 3b presents the schematics of the single edge notched specimen used for the measurements. The crosshead of the instrument was operated at a speed of 2 mm/min to strain the samples using a very sensitive calibrated 10 Newton load cell. The test was performed for the polymer blends with different concentrations of the lithium perchlorate ( $\text{LiClO}_4$ ) salt.

#### **4.3.2. Nanoindentation Measurements**

The flexible uniform and transparent films were mounted on steel stage for indentation test. The indentation experiments were used to measure the Young's moduli and hardness values of the solid state electrolyte (PVA/PVP/  $\text{LiClO}_4$ ). The resulting films had an average thicknesses of ~ 0.33 mm, measured using a micrometer screw gauge. The indentation measurements were carried out on all the prepared films while maintaining a relative humidity of less than 5% to prevent the film from absorbing moisture within the environment using the TI950 Triboindenter (Hysitron Inc., Minneapolis, MN USA), coupled to a Dimension 3100 scanning probe microscope (Veeco Instruments Inc., Woodbury, NY), (A Berkovich indenter tip, a three-sided pyramidal-type tip, with an included angle of  $142.3^\circ$ ) was used for indentation testing. The choice of the Berkovich indenter was because of its large included angle which tends to increase the contact area with the samples. The indentation loading profile included the following three steps: loading to a peak load in 10 s; holding at the peak load for 5 s, and returning to zero load in 10 s. A peak load ranging from 500  $\mu\text{N}$  to 1000  $\mu\text{N}$  was applied. Grid indentation with multi-points using a 6 x 6 (36 points array) matrix mapping was carried out to determine the average

elastic modulus and average hardness of the sample. The same load function was set for each experiment in the grid. To minimize the possible interactions between adjacent indents, all the indents were separated by at least 7  $\mu\text{m}$ . A contact-based scanning probe method was used to capture the images of the surfaces before and after the indentation.

The indentation depths were generally much greater than the surface roughness levels. Commonly, for metallic materials, indentation depths should be at least 20 times greater than the average surface roughness to minimize the possible effects of rough surfaces [43]. Also, the indentation depths should be less than 10% of the film thickness to minimize substrate effects [38], especially for those films harder than the substrate. In this study, a range of peak loads was selected, which generated a range of contact depths during the indentation experiments, to study the possible effects of indentation depth. Finally, the peak loads were maintained for sufficient durations to minimize the possible effects of viscoelasticity on the measured elastic moduli. In addition to determining the elastic modulus and hardness, loads above the peak values were applied for possible inducement of cracks within the layers to study the fracture toughness of the samples. The images of the samples were viewed using a scanning probe microscope (SPM) attached to the Triboindenter. Furthermore, statistical deconvolution mapping was carried out to further determine the mechanical properties using its toolbox in Matlab software (MATHWORKS Inc. Natick, MA. USA).

#### **4.3.3. Materials Characterization**

The surface morphology of the samples was characterized using a scanning electron microscope (SEM, ZEISS EVO LS10 Massachusetts, USA). The crystallinity of the samples was carried out using a Malvern PANalytical X-ray diffractometer (XRD) (Malvern PANalytical, Westborough, MA, USA), equipped with a Cu  $K\alpha$  radiation source and a Beta Nickel filter that was operated at

40 kV and 40 mA in the  $2\theta$  range ( $2\theta = 10-90$ ). Fourier-Transform Infrared (FTIR) measurements were used to obtain the transmittance spectra of the films. These were obtained using a QATR-S single reflection integration type ATR accessory with a diamond crystal (QATR-S, Shimadzu, USA) with a wave number range of  $500-4000\text{ cm}^{-1}$ .

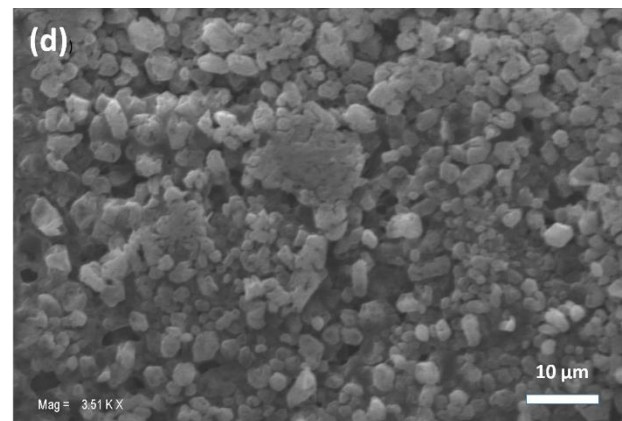
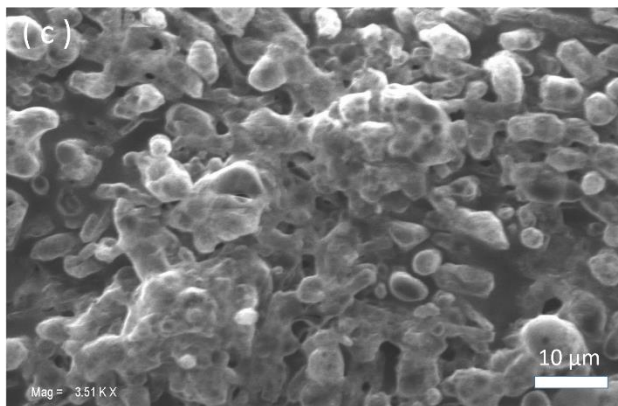
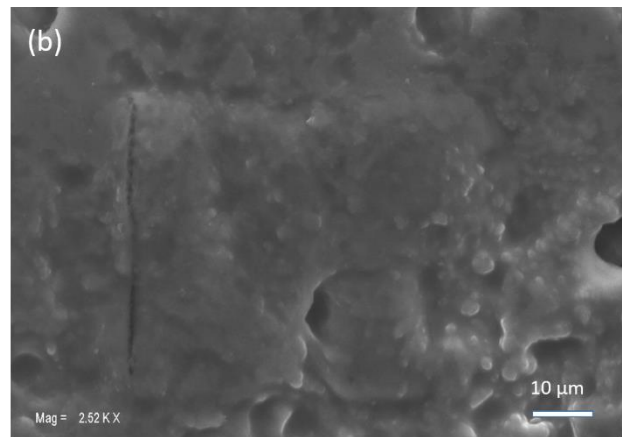
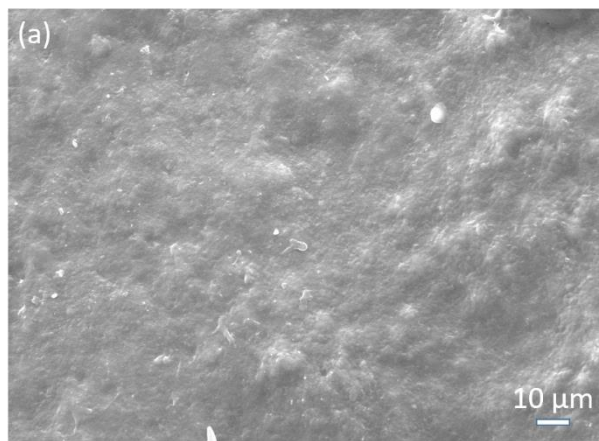
#### 4.4. Results and Discussions

##### 4.4.1. Microstructures

The surface morphologies of the uniform and flexible transparent films are presented in Fig. 4.4(a-f). Figure 4.4a shows a uniform rough surface for the blend of PVA/PVP. In Fig. 4.4(b – f), the uniform roughness of the film surfaces increases due to the dissolution of salt ( $\text{LiClO}_4$ ) in the blended polymer film. As the amount of salt increases, some crystallites are also observed in blend polymers. This is clear from the XRD results, which shows that the PVA/PVP is amorphous in nature. The differences in the surface morphologies are attributed to the oxidation and interactions of the functional groups that are present in the polymer blend (presence of hydroxyl group of PVA and carbonyl group of PVP) with different salt contents. The roughness and crystallinity can also be explained by the distribution of the salt in the blended polymer matrix.

X-ray diffraction (XRD) patterns of the flexible transparent films are presented in Figure 4.5a. PVA has been reported to be semi-crystalline in nature with peaks appearing at  $20^\circ$  and  $40^\circ$  [7], [51]. From Figure 5, the polymer blend of PVA/PVP has peaks at  $2\theta = 19.6^\circ$  and  $40.2^\circ$ . These are associated with the long chain carbon backbone and amorphous nature of the PVA in the

polymer blends with PVP. However, the amorphous nature of the polymer blend changes, as the concentration of lithium perchlorate increased in the matrices, this is as a result of the complex bond of  $\text{Li}^+ \dots \text{C}=\text{O}$  (short range of  $\text{LiClO}_4$  in the matrix of PVA/PVP blend. [14], [52]).



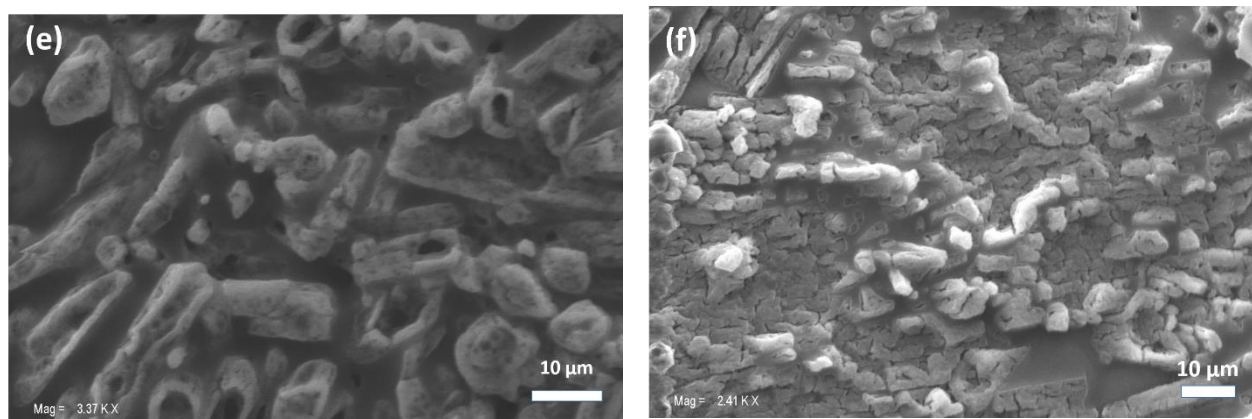


Figure 4.4. SEM micrographs (a) PVA + PVP (b) PVA + PVP + 1 wt % LiClO<sub>4</sub> (c) PVA + PVP + 2 wt % LiClO<sub>4</sub> (d) PVA + PVP + 3 wt % LiClO<sub>4</sub> (e) PVA + PVP + 4 wt % LiClO<sub>4</sub> (f) PVA + PVP + 5 wt % LiClO<sub>4</sub>

Hence, increasing the concentration of the LiClO<sub>4</sub> increases the crystallinity of the compositions.

It was also observed that the interactions of the functional groups present in PVA/PVP and the dopant ions from LiClO<sub>4</sub> (Li<sup>+</sup> and ClO<sub>4</sub><sup>-</sup>) leads to the displacement of the ions from their lattice sites which is responsible for the shifts in peaks and crystallinity of the composition [53].

The above interactions, as well as the bond formations of the polymer blends and the compositions of the matrices with the LiClO<sub>4</sub>, were investigated with the IR spectra. The IR spectra of the films with different concentrations of the LiClO<sub>4</sub> are presented in Figure 4.5b. The band observed at ~ 1564 cm<sup>-1</sup> originate from PVP and is attributed to the characteristics vibration of pyridine ring (C=N) while the transmission band at 844 cm<sup>-1</sup> is associated with the out-of-plane rings of C-H bending. The pure PVA has its transmission band at 3340 cm<sup>-1</sup> due to the O-H stretching vibration of hydroxyl group which is consistent with literature [7], [14], [54]. The respective IR bands of the polymer blend at 3340 cm<sup>-1</sup>, 2932 cm<sup>-1</sup>, 1646 cm<sup>-1</sup>, 1419 cm<sup>-1</sup>, 1020 cm<sup>-1</sup> and 928 cm<sup>-1</sup> are due to the O-H stretching, (C-H)<sub>n</sub> asymmetric stretching, C=O stretching, CH<sub>2</sub> bending, C-O stretching and C-O Symmetric stretching, respectively. [7], [12]. The shift of C=O bond signal is also due to the hydrogen bond between C=O and OH groups.

This is in agreement with the XRD results (Figure 5a). The shape and intensity of the bands also increases as the concentration of  $\text{LiClO}_4$  increases, this is responsible for the transition from the semi-crystalline of the polymer blend to the crystalline nature of the electrolyte. At  $\sim 1647\text{ cm}^{-1}$ , the presence of the vibrational band corresponds to the C–O symmetric bending of PVA and PVP [7], [14], [55]. Peaks from  $1640\text{ cm}^{-1}$  to  $1649\text{ cm}^{-1}$  regions are attributed to shift in stretching modes of the carbonyl bonds, as a result of the pyrrolidone rings. In summary, it can be inferred that the shifts and variations in the intensities of the FTIR spectra (of the electrolyte compositions) describe the complexities of the salt and polymer blends [7], [12].

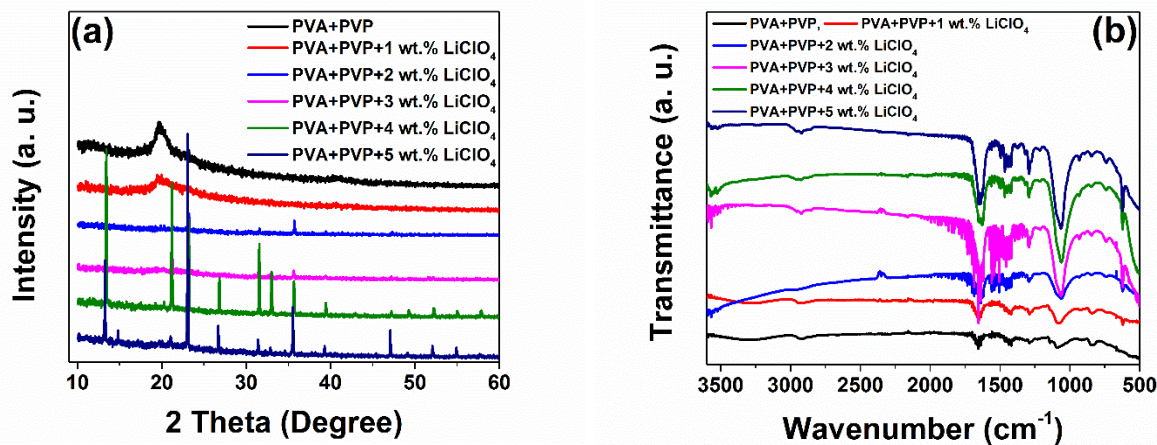


Figure 4.5: (a) XRD patterns of 2 wt% PVA: 2 wt% PVP with blends of various concentrations of Lithium perchlorate. (b) FTIR spectra of 2 wt% PVA: 2 wt% PVP with blends of various concentrations of Lithium perchlorate.

#### 4.4.2. Indentation Measurements and Fracture Toughness

A summary of the Young's moduli (E), hardness (H) values and fracture toughness values obtained from this study is presented in table 4.1, which also includes the ratio E/H. It is interesting to note here that the concentration of the salt ( $\text{LiClO}_4$ ) in the blends of the polymer matrix (PVA/PVP) increased until an optimal value was reached. It then decreased with increasing salt concentration. This can be attributed to the formation of stronger bonds between

the polymer matrix and the salt as the salt concentration increases. However, beyond the optimal value of salt concentration, the drop in the values of E and H indicates that the composite material becomes brittle. On the other hand, as seen in Figure 4.6a, the contact depth decreases as the concentration of the salt (LiClO<sub>4</sub>) in the blend of the polymer matrix (PVA/PVP) increases until an optimal value and then increases. The reason for a decrease in contact depth implies that the material has a high strength and high resistance to deformation, a characteristic needed to suppress any dendrite growth of Li metals and boost large-scale device production [27], [56], [57].

Table 4.1. Indentation measurements and tensile tests of the PVA/PVP/LiClO<sub>4</sub> blend at different salt concentration.

<b>Sample</b>	<b>Young's Modulus (GPa)</b>	<b>Hardness (GPa)</b>	<b>Fracture Toughness (MPa.m<sup>0.5</sup>)</b>	<b>E/H</b>	<b>Tensile Strength (MPa)</b>
<b>PVA/PVP (50/50)</b>	1.72	0.53	0.32	3.25	7.85
<b>PVA/PVP + 1 wt.% LiClO<sub>4</sub></b>	2.40	0.57	0.45	4.22	1.44
<b>PVA/PVP + 2 wt.% LiClO<sub>4</sub></b>	2.70	0.63	0.5	4.29	1.34
<b>PVA/PVP + 3 wt.% LiClO<sub>4</sub></b>	4.11	0.92	0.76	4.47	3.00
<b>PVA/PVP + 4 wt.% LiClO<sub>4</sub></b>	6.87	1.3	0.81	5.29	4.30
<b>PVA/PVP + 5 wt.% LiClO<sub>4</sub></b>	4.14	0.91	0.78	4.55	1.51

Figure 4.6a shows the plot of hardness (GPa) as a function of the displacement (nm). It is observed that the hardness decreased as the displacement increased. This is due to decrease in contact depth and roughness of the material. Similarly, in Figure 4.6b, the plot of reduced modulus (GPa) against displacement (nm) shows that the modulus decreases as the displacement increases. Fig. 4.6c and Fig. 4.6d presents a plot of the Force ( $\mu\text{N}$ ) as a function of the displacement (nm). These show the loading, hold and unloading times of each concentration of the film, all emanating from the origin. Figure 6e presents plots of reduced modulus (GPa) against Hardness (GPa). It was observed that both properties increased with increasing concentration of the salt ( $\text{LiClO}_4$ ) in the blends up to an optimal value at PVA/PVP/4 wt. %  $\text{LiClO}_4$ , beyond which the properties decreased. Fig. 4.6f and 4.6g presents respective 3-D images of the solid electrolyte before and after indentation. A peak load of 5000  $\mu\text{N}$  (as against the initial 1000  $\mu\text{N}$  load used) was applied. However, no visible crack was observed after the application of this load.

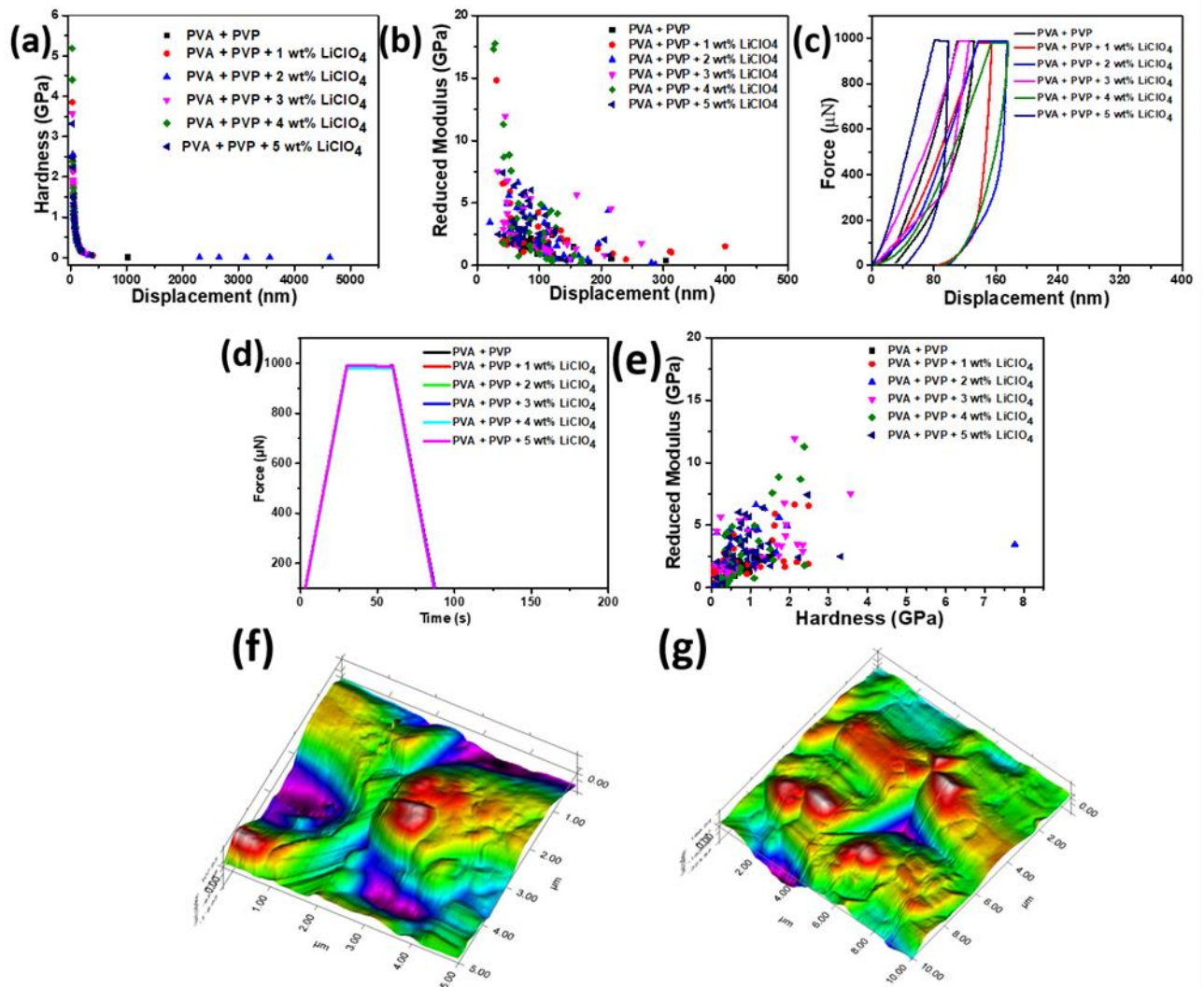


Figure 4.6. Indentation Plots (a) Hardness Vs Displacement (b) Elastic Modulus Vs Displacement (c) Force Vs Displacement (d) Force Vs Time (e) Elastic Modulus Vs Hardness (f) 3-D image of polymer blend before indentation (g) 3-D image of polymer blend after indentation.

To further elucidate the fracture behaviour of the flexible polymer blend, the fracture toughness was measured using a single edge notched specimen. Figure 4.7a presents the force-displacement curves for the control (PVA+PVP) and polymers with different proportions of  $\text{LiClO}_4$ . The results show that the blends with incorporation of 1 - 2% of  $\text{LiClO}_4$  salt have similar ductile behaviour as the control specimen with evident of low strength. The force-displacement curves are very close (Figure 4.7a). However, the strength increased with increasing proportion of the

salt from 2% to 4%. The ductility of the polymer blend also decreases with increasing concentration of the salt. At higher concentration (up to 5%), the strength of the flexible polymer blend is reduced (Fig. 4.7a). The decrease in the strength at 5 wt. % can be associated with inhomogeneity of the excessive powder in the blend which can create pathways for crack initiation and propagation. It is important to note that a balance is needed between the strength and ductility of the reinforced LiClO<sub>4</sub> salt - flexible polymer blend for a desired functionality.

The fracture toughness of the polymers were estimated using Equation 4.15. Fig. 4.7b presents the results of the fracture toughness values for control and LiClO<sub>4</sub> incorporated flexible polymer blends. The results is also summarized in Table 4.2. The results show that the fracture toughness of the polymer blends increased as the concentration of the salt increases from 0% to 4%. The increase in the toughness is attributed to the formation of stronger bonds between the polymer matrix and the salt. The optimal value of the toughness was recorded for polymer with 4 wt.% concentration of the salt. We observed a drop in fracture toughness value for flexible polymer with 5 wt.% concentration. The trend in the fracture toughness results obtained from the single notched samples is in agreement with the result obtained from the fracture toughness obtained from the nanoindentation technique (Table 4.1). The optical images of the failure mechanisms of the fractured flexible polymer blends are presented in Fig. 4.7c (I, II, III, IV, and V). As the notch opens, we see evidence of tip blunting before crack initiation. There is also evidence of voids formation that coalesced to form big cracks. The implication of the result is that this polymer blends has a good fracture toughness that can be recommended as solid state electrolyte material for application in energy storage.

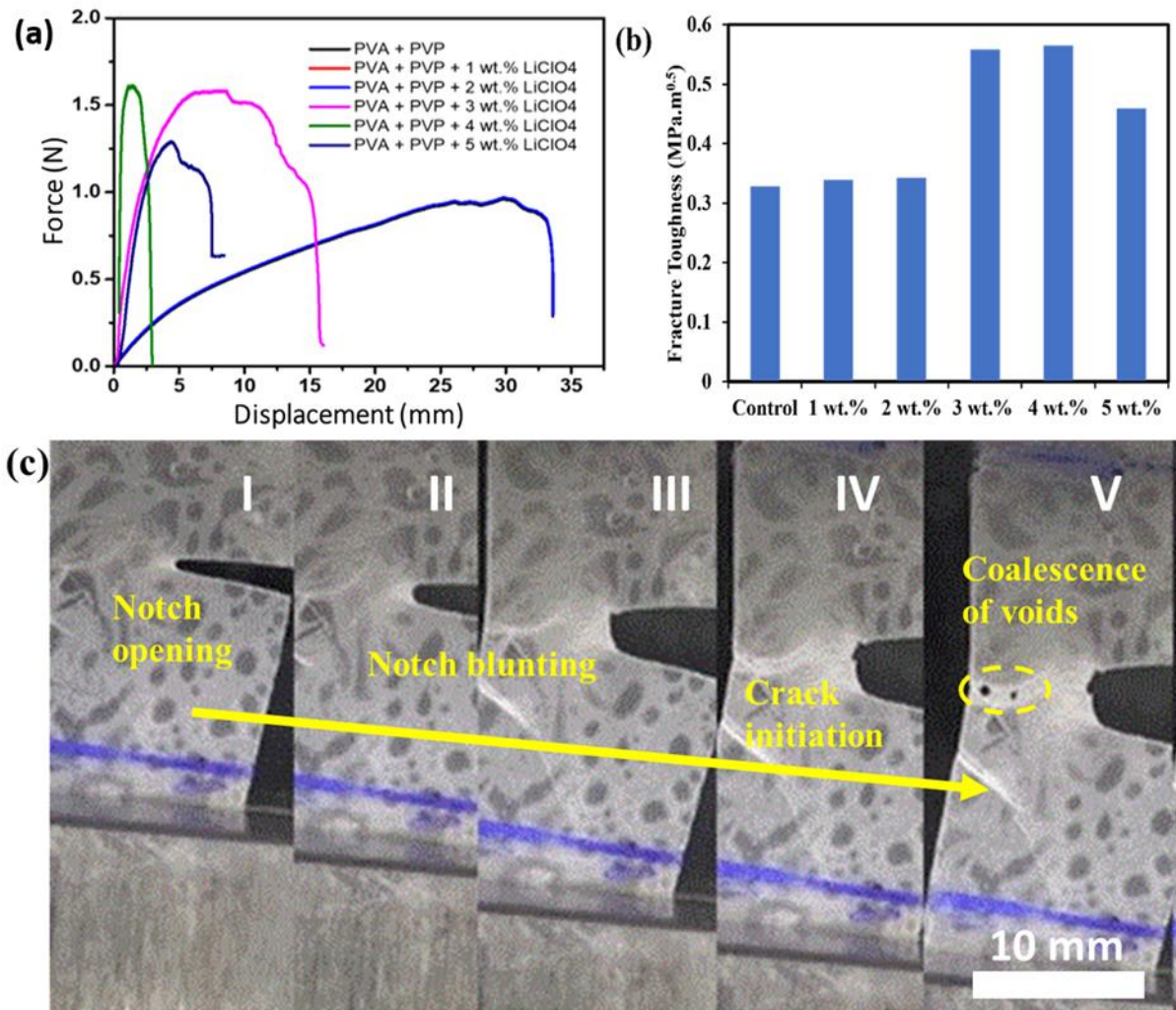


Figure 4.7. (a) Plots of force-displacement curves, (b) fracture toughness values and (c) Optical images of failure mechanisms during fracture of the flexible polymer blends

Table 4.2. Summary of the fracture toughness values using single edge notched specimen under tension result.

Sample	Toughness (MPa.m <sup>0.5</sup> )
PVA + PVP	0.3286

PVA + PVP + 1 wt.% LiClO <sub>4</sub>	0.3392
PVA + PVP + 2 wt.% LiClO <sub>4</sub>	0.3424
PVA + PVP + 3 wt.% LiClO <sub>4</sub>	0.5588
PVA + PVP + 4 wt.% LiClO <sub>4</sub>	0.5649
PVA + PVP + 5 wt.% LiClO <sub>4</sub>	0.4590

---

#### 4.4.3. Result of Tensile Tests

The tensile test was performed for the polymer blends with different concentrations of the lithium perchlorate (LiClO<sub>4</sub>) salt and the results of the tensile strength is presented in Table 4.1 and Fig. 4.8. From Table 4.1, the tensile strength for the PVA + PVP blend is higher than what was obtained after the addition of the different concentrations of the LiClO<sub>4</sub> salts; this is due to less impact of elastic deformation and elongation of the polymer chains. It also demonstrates better comparative ductility and toughness as seen from the area under the curve in Figure 4.8 as well as good linear relationship between the stress and strain.

The addition of 1 wt.% LiClO<sub>4</sub> salt to the polymers blend results to significant reduction in the tensile strength due to weak intermolecular interaction as well as poor adhesion at the interface of the blends [58]. It was also observed that this increased the ductility of the material due to further elongation of the polymer chains. There was an irregularity of tensile strength behaviour at 2 wt.% LiClO<sub>4</sub> which could be attributed to the presence of defects as reported by Sallal et al. [4]. The tensile strength value increased with the highest value recorded at the concentration of 4 wt.% LiClO<sub>4</sub> and then reduced at the addition of 5 wt.% LiClO<sub>4</sub> due to reduction in the crystallinity as seen in the XRD pattern of Figure 4.5a.

The above trend shows that the complex formed at the addition of 4 wt% LiClO<sub>4</sub> gave an optimal tensile strength of the polymer blends with the salt (which is in agreement with the results of the hardness, Young's modulus and fracture toughness performed with the Nano indentation tests in

Table 4.1). This is due to stronger bonds formed from the interactions of the various functional groups present as seen in the FTIR analysis (Fig. 4.5b). Also, the XRD analysis (Fig. 4.5a) reveals that increasing the particle loading of the polymer blends increases the crystallinity of the resultant composite which further explains the increase in the tensile strength as the salt concentration is increased from 1wt % to 4 wt %.

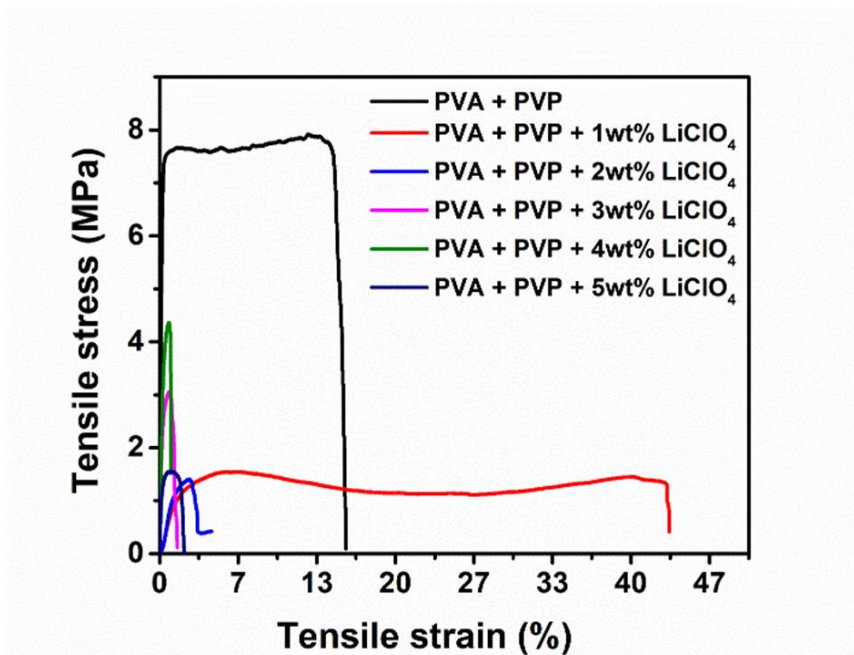


Figure 4.8. Plot of Tensile stress (MPa) against Tensile strain (%)

#### 4.5. Deconvolution and mapping Results using Statistical Deconvolution Toolbox.

The mapping from the indentation test to determine the tribological properties of the PVA/PVP/LiClO<sub>4</sub> blend of the polymer blend are presented in Figure 4.9 (a - d). The mapping was implemented using Matlab Software (MATHWORKS Inc. Natick, MA. USA) to extract the values of the Young's modulus and hardness values from the multiple grids in the indentation test.

Figure 4.9a shows the statistical deconvolution mapping of elastic modulus (GPa) in the x and y coordinates ( $\mu\text{m}$ ) respectively with 6 points of indents along x-axis as well 6 points of indents along y/z axis making a total of 36 points array. The distance between indents (along both axis) was  $7\ \mu\text{m}$ . Also, the Young's modulus (in GPa) differentiated with color bars having a mean property value of  $11.57\ \text{GPa}$ . ( $\pm 46.75$ ). Figure 4.9b presents the statistical mapping of hardness (GPa) in the x and y coordinates ( $\mu\text{m}$ ), respectively, with the distance between indents in both axis being  $7\ \mu\text{m}$ , while the hardness (GPa), differentiated with color bars, had a mean value of  $6.01\ \text{GPa}$ . ( $\pm 3.8$ ).

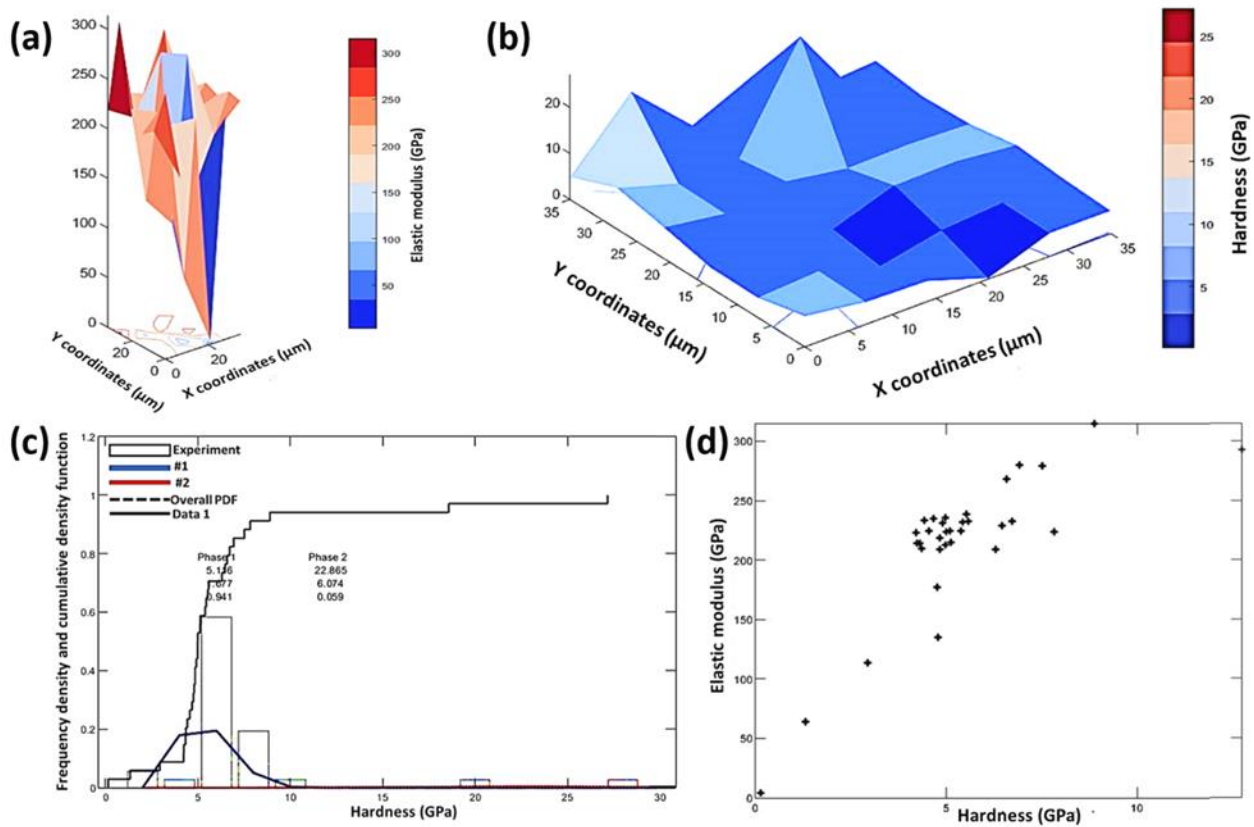


Figure 4.9. (a) Statistical deconvolution mapping of Elastic Modulus (b) Statistical deconvolution mapping of Hardness (c) Elastic Modulus Vs Hardness (d) Probability density function (PDF) and cumulative density function (CDF) against Hardness (GPa)

Figure 4 9c shows the statistical deconvolution mapping of the plots of elastic modulus (GPa) against hardness (GPa). The elastic modulus has a direct correlation with hardness. This result is in agreement with the nanoindentation calculated result which is attributed to the formation of stronger bonds between the polymer matrix and the salt. The variance in the nanoindentation calculated result and statistical deconvolution result could be as a result of the large size of the 36 points array.

Table 4.3. Results of the statistical deconvolution mapping of mechanical properties from indentation experiments.

<b>Mechanical Property</b>	<b>Mean Property Value (GPa)</b>	<b>Number of Points in Array</b>	<b>Spacing between Indents (<math>\mu\text{m}</math>)</b>
<b>Average Young's modulus (E)</b>	$11.57 \pm 46.75$	36	7
<b>Average Hardness (H)</b>	$6.01 \pm 3.8$	36	7

Figure 4.9d. The plot of probability density function (PDF) and cumulative density function (CDF) against hardness (GPa) showing the changes in phase in the histogram tabulated in Table 4.3. The results suggest the improvement in the mechanical properties from phase 1 to phase 2

Table 4.4 PDF and CDF against Hardness (GPa)

	<b>Phase 1 of PDF</b>	<b>Phase 2 of PDF</b>
	<b>(Hardness in GPa)</b>	<b>(Hardness in GPa)</b>
<b>Maximum Value</b>	5.116	22.865
<b>Mean Value</b>	1.677	6.074
<b>Minimum Value</b>	0.941	0.059

#### 4.6. Research Findings and Implications

The mechanical properties obtained from this work are comparable to those reported by Dibyendu Mondal et al [5] and Ali A. Sallal et al [4]. They suggest that PVA/PVP/ LiClO<sub>4</sub> blends are potential candidates for applications in solid state electrolytes for energy storage systems. The trends in the measured Young's moduli and hardness values also imply that the control of the blend mixtures can be used to engineer the design of robust films with attractive combinations of strength, Young's moduli and fracture toughness.

#### 4.7. Summary and Concluding Remarks

This work explores the structure and mechanical properties of PVA/PVP/ LiClO<sub>4</sub> blends that are being explored as solid electrolytes in energy storage systems. Optimal reduced modulus and hardness values (6.87 GPa and 1.30 GPa, respectively) and the fracture toughness estimates of 0.81 MPa.m<sup>0.5</sup> were obtained. The results shows that the moduli (E) and hardness (H) values of the materials, as well as the ratio, E/H, and the fracture toughness, increased as the concentration

of the salt ( $\text{LiClO}_4$ ) in the blend of the polymer matrix (50 PVA:50 PVP) increases. These increases continue until the minimum contact depth is reached. The contact depth then increased with increasing PVA/PVP proportions. Also, the combination of mechanical properties (Young's moduli, hardness values and fracture toughness) of the PVA/PVP blends compares favourably with those of emerging promising materials that are being developed for potential applications in solid state electrolytes.

Although, the focus of this work is on the Mechanical Properties of Polyvinyl Pyrrolidone /Polyvinyl Alcohol-based Solid Electrolytes. This work acknowledges that a detailed optimization of the conductivity is needed to develop electrolytes with optimum conductivity as a function of temperature which will be studied in future work.

## REFERENCES

- [1] L. L. Baranowski, C. M. Heveran, V. L. Ferguson, and C. R. Stoldt, "Multi-Scale Mechanical Behavior of the Li<sub>3</sub>PS<sub>4</sub> Solid-Phase Electrolyte," pp. 4–10, 2016.
- [2] K. Orisekeh et al., "Processing of  $\alpha$ -Fe<sub>2</sub>O<sub>3</sub> Nanoparticles on Activated Carbon Cloth as Binder-Free Electrode Material for Supercapacitor Energy Storage," *J. Energy Storage*, vol. 33, no. July, 2021.
- [3] J. Rodríguez, E. Navarrete, E. A. Dalchiele, L. Sánchez, J. R. Ramos-barrado, and F. Martín, "Polyvinylpyrrolidone e LiClO<sub>4</sub> solid polymer electrolyte and its application in transparent thin fi lm supercapacitors," vol. 237, pp. 270–276, 2013.
- [4] A. A. Sallal, S. A. Salman, and A. A. Habeeb, "Research Article Studying Of Some Dielectric And Mechanical Properties Of ( Pva : Pvp Pva : Pvp ) Polymer Blend," 2018.
- [5] D. Mondal et al., "Progress in Natural Science : Materials International Effect of poly ( vinyl pyrrolidone ) on the morphology and physical properties of poly ( vinyl alcohol )/ sodium montmorillonite nanocomposite fi lms," *Prog. Nat. Sci. Mater. Int.*, vol. 23, no. 6, pp. 579–587, 2013.
- [6] M. J. Reddy, S. S. Rao, E. Laxminarsaiah, and U. V. S. Rao, "Study of a thin film electrochemical cell based on (PVP+ AgNO<sub>3</sub>) electrolyte," *Solid State Ionics*, vol. 80, no. 1–2, pp. 93–98, 1995.

- [7] K. Sundaramahalingam, M. Muthuvinayagam, N. Nallamuthu, D. Vanitha, and M. Vahini, "Investigations on lithium acetate-doped PVA/PVP solid polymer blend electrolytes," *Polym. Bull.*, vol. 76, no. 11, pp. 5577–5602, 2019.
- [8] T. Sandu et al., "Functionalized bicomponent polymer membranes as supports for covalent immobilization of enzymes," *React. Funct. Polym.*, vol. 96, pp. 5–13, 2015.
- [9] D. Ebrasu, I. Stamatina, and A. Vaseashta, "Proton-conducting polymers as electrolyte for fuel cells," *Nano*, vol. 3, no. 05, pp. 381–386, 2008.
- [10] M. Z. A. Yahya and A. K. Arof, "Effect of oleic acid plasticizer on chitosan--lithium acetate solid polymer electrolytes," *Eur. Polym. J.*, vol. 39, no. 5, pp. 897–902, 2003.
- [11] L. Ismail, S. R. Majid, and A. K. Arof, "Conductivity study in PEO--LiOAc based polymer electrolyte," *Mater. Res. Innov.*, vol. 13, no. 3, pp. 282–284, 2009.
- [12] E. M. Abdelrazek, I. S. Elashmawi, A. El-khodary, and A. Yassin, "Structural, optical, thermal and electrical studies on PVA/PVP blends filled with lithium bromide," *Curr. Appl. Phys.*, vol. 10, no. 2, pp. 607–613, 2010.
- [13] J. Qiao, J. Fu, R. Lin, J. Ma, and J. Liu, "Alkaline solid polymer electrolyte membranes based on structurally modified PVA/PVP with improved alkali stability," *Polymer (Guildf.)*, vol. 51, no. 21, pp. 4850–4859, 2010.
- [14] H.-D. Wu, I.-D. Wu, and F.-C. Chang, "The interaction behavior of polymer electrolytes composed of poly (vinyl pyrrolidone) and lithium perchlorate (LiClO<sub>4</sub>)," *Polymer (Guildf.)*, vol. 42, no. 2, pp. 555–562, 2001.

- [15] M. Marzantowicz et al., "Star-branched poly (ethylene oxide) LiN (CF<sub>3</sub>SO<sub>2</sub>)<sub>2</sub>: A promising polymer electrolyte," *J. Power Sources*, vol. 194, no. 1, pp. 51–57, 2009.
- [16] R. F. Bhajantri, V. Ravindrachary, B. Poojary, A. Harisha, and V. Crasta, "Studies on fluorescent PVA+ PVP+ MPDMAPP composite films," *Polym. Eng. Sci.*, vol. 49, no. 5, pp. 903–909, 2009.
- [17] M. A.-F. Basha, "Magnetic and optical studies on polyvinylpyrrolidone thin films doped with rare earth metal salts," *Polym. J.*, vol. 42, no. 9, pp. 728–734, 2010.
- [18] R. Xue, S. Mei, J. Qing, H. Otsuka, and A. Takahara, "Preparation and characterization of cross-linked  $\beta$ -cyclodextrin polymer / Fe<sub>3</sub>O<sub>4</sub> composite nanoparticles with core-shell structures," vol. 22, pp. 217–220, 2011.
- [19] Z. Gadjourova, D. y Marero, K. H. Andersen, Y. G. Andreev, and P. G. Bruce, "Structures of the polymer electrolyte complexes PEO6: LiXF<sub>6</sub> (X= P, Sb), determined from neutron powder diffraction data," *Chem. Mater.*, vol. 13, no. 4, pp. 1282–1285, 2001.
- [20] M. J. Reddy, T. Srekanth, M. Chandrashekar, and U. V. S. Rao, "Ion transport and electrochemical cell characteristic studies of a new (PVP 1 NaNO<sub>3</sub>) polymer electrolyte system," *J. Mater. Sci.*, vol. 35, no. 11, pp. 2841–2845, 2000.
- [21] H. M. Zidan, A. Tawansi, and M. Abu-Elnader, "Miscibility, optical and dielectric properties of UV-irradiated poly (vinylacetate)/poly (methylmethacrylate) blends," *Phys. B Condens. Matter*, vol. 339, no. 2–3, pp. 78–86, 2003.

- [22] J. Su, Z. Y. Ma, J. I. Scheinbeim, and B. A. Newman, "Ferroelectric and piezoelectric properties of nylon 11/poly (vinylidene fluoride) bilaminate films," *J. Polym. Sci. Part B Polym. Phys.*, vol. 33, no. 1, pp. 85–91, 1995.
- [23] A. Tawansi and H. M. Zidan, "Magnetic effects of the interfacial solitons in polystyrene composites," *J. Phys. D. Appl. Phys.*, vol. 23, no. 10, p. 1320, 1990.
- [24] S. Jeong Kim, S. Jun Park, I. Young Kim, Y. Hee Lee, and S. I. Kim, "Thermal characteristics of poly (vinyl alcohol) and poly (vinylpyrrolidone) IPNs," *J. Appl. Polym. Sci.*, vol. 86, no. 8, pp. 1844–1847, 2002.
- [25] H. Yu, X. Xu, X. Chen, T. Lu, P. Zhang, and X. Jing, "Preparation and antibacterial effects of PVA-PVP hydrogels containing silver nanoparticles," *J. Appl. Polym. Sci.*, vol. 103, no. 1, pp. 125–133, 2007.
- [26] N. Rajeswari, S. Selvasekarapandian, S. Karthikeyan, C. Sanjeeviraja, Y. Iwai, and J. Kawamura, "Structural, vibrational, thermal, and electrical properties of PVA/PVP biodegradable polymer blend electrolyte with  $\text{CH}_3\text{COONH}_4$ ," *Ionics (Kiel)*, vol. 19, no. 8, pp. 1105–1113, 2013.
- [27] S. Yu et al., "Elastic properties of the solid electrolyte  $\text{Li}_7\text{La}_3\text{Zr}_2\text{O}_{12}$  (LLZO)," *Chem. Mater.*, vol. 28, no. 1, pp. 197–206, 2016.
- [28] I. Yoon, S. Jurng, D. P. Abraham, B. L. Lucht, and P. R. Guduru, "Measurement of mechanical and fracture properties of solid electrolyte interphase on lithium metal anodes in lithium ion batteries," *Energy Storage Mater.*, vol. 25, pp. 296–304, 2020.

- [29] E. Peled and S. Menkin, "SEI: past, present and future," *J. Electrochem. Soc.*, vol. 164, no. 7, p. A1703, 2017.
- [30] K. Xu, "Electrolytes and interphases in Li-ion batteries and beyond," *Chem. Rev.*, vol. 114, no. 23, pp. 11503–11618, 2014.
- [31] W.-J. Zhang, "A review of the electrochemical performance of alloy anodes for lithium-ion batteries," *J. Power Sources*, vol. 196, no. 1, pp. 13–24, 2011.
- [32] K. Xu, "Nonaqueous Liquid Electrolytes for Lithium-Based Rechargeable Batteries," *Chem. Rev.*, vol. 104, no. 10, pp. 4303–4418, 2004.
- [33] J. Xu, L. Wang, J. Guan, and S. Yin, "Coupled effect of strain rate and solvent on dynamic mechanical behaviors of separators in lithium ion batteries," *Mater. Des.*, vol. 95, pp. 319–328, 2016.
- [34] G. Yan, J. F. Nonemacher, H. Zheng, M. Finsterbusch, J. Malzbender, and M. Krüger, "An investigation on strength distribution, subcritical crack growth and lifetime of the lithium-ion conductor  $\text{Li}_7\text{La}_3\text{Zr}_2\text{O}_{12}$ ," *J. Mater. Sci.*, vol. 54, no. 7, pp. 5671–5681, 2019.
- [35] G. Yan et al., "Anisotropy of the mechanical properties of  $\text{Li}_{1.3}\text{Al}_{0.3}\text{Ti}_{1.7}(\text{PO}_4)_3$  solid electrolyte material," *J. Power Sources*, vol. 437, p. 226940, 2019.
- [36] C. D. Fincher, D. Ojeda, Y. Zhang, G. M. Pharr, and M. Pharr, "Mechanical properties of metallic lithium: from nano to bulk scales," *Acta Mater.*, vol. 186, pp. 215–222, 2020.
- [37] G. M. Pharr and W. C. Oliver, "Measurement of Thin Film Mechanical Properties Using Nanoindentation," *MRS Bull.*, vol. 17, no. 7, pp. 28–33, 1992.

- [38] W. C. Oliver and G. M. Pharr, "An improved technique for determining hardness and elastic modulus using load and displacement sensing indentation experiments," *J. Mater. Res.*, vol. 7, no. 6, pp. 1564–1583, 1992.
- [39] J. Malzbender and G. De With, "The use of the indentation loading curve to detect fracture of coatings," *Surf. Coatings Technol.*, vol. 137, no. 1, pp. 72–76, 2001.
- [40] J. Malzbender and G. De With, "The use of the loading curve to assess soft coatings," *Surf. Coatings Technol.*, vol. 127, no. 2–3, pp. 265–272, 2000.
- [41] A. N. Wang, J. F. Nonemacher, G. Yan, M. Finsterbusch, J. Malzbender, and M. Krüger, "Mechanical properties of the solid electrolyte Al-substituted  $\text{Li}_7\text{La}_3\text{Zr}_2\text{O}_{12}$  (LLZO) by utilizing micro-pillar indentation splitting test," *J. Eur. Ceram. Soc.*, vol. 38, no. 9, pp. 3201–3209, 2018.
- [42] J. F. Nonemacher et al., "Microstructure and properties investigation of garnet structured  $\text{Li}_7\text{La}_3\text{Zr}_2\text{O}_{12}$  as electrolyte for all-solid-state batteries," *Solid State Ionics*, vol. 321, no. April, pp. 126–134, 2018.
- [43] "International Organization for Standardization, ISO 14577-1:2002, Metallic Materials, Instrumented Indentation Test for Hardness and Materials Parameters - Part 1: Test Method.," <https://www.iso.org/standard/30104.html>. .
- [44] J. J. Kruzic, D. K. Kim, K. J. Koester, and R. O. Ritchie, "Opinion piece Indentation techniques for evaluating the fracture toughness of biomaterials and hard tissues," *J. Mech. Behav. Biomed. Mater.*, vol. 2, no. 4, pp. 384–395, 2009.
- [45] J. Chen and S. J. Bull, "Indentation fracture and toughness assessment for thin optical coatings on glass," vol. 40, no. 18, pp. 5401–5417, 2007.

- [46] X. Wang et al., “lithiated silicon,” no. May, pp. 1–7, 2015.
- [47] C. Hu and Z. Li, “A review on the mechanical properties of cement-based materials measured by nanoindentation,” vol. 90, pp. 80–90, 2015.
- [48] K. Liu, M. Ostadhassan, and B. Bubach, “Journal of Natural Gas Science and Engineering Applications of nano-indentation methods to estimate nanoscale mechanical properties of shale reservoir rocks,” *J. Nat. Gas Sci. Eng.*, vol. 35, pp. 1310–1319, 2016.
- [49] K. K. Jha, N. Suksawang, D. Lahiri, and A. Agarwal, “Energy-Based Analysis of Nanoindentation Curves for Cementitious Materials,” no. 109, pp. 81–90, 2012.
- [50] P. Taylor, Y. Cheng, and Z. Li, “Scaling relationships for indentation measurements,” no. October 2013, pp. 37–41.
- [51] S. B. Aziz, M. A. Rasheed, A. M. Hussein, and H. M. Ahmed, “Fabrication of polymer blend composites based on [PVA-PVP](1-x):(Ag<sub>2</sub>S)x (0.01 ≤ x ≤ 0.03) with small optical band gaps: Structural and optical properties,” *Mater. Sci. Semicond. Process.*, vol. 71, no. March, pp. 197–203, 2017.
- [52] S. B. Aziz and R. M. Abdullah, “Crystalline and amorphous phase identification from the tanδ relaxation peaks and impedance plots in polymer blend electrolytes based on [CS:AgNt]x:PEO(x-1) (10 ≤ x ≤ 50),” *Electrochim. Acta*, vol. 285, pp. 30–46, 2018.
- [53] R. M. Hodge, “Water absorption and states of water in sernicrystalline poly ( vinyl alcohol ) films,” vol. 37, no. 8, pp. 1371–1376, 1996.
- [54] W. Dong, J. S. Sakamoto, and B. Dunn, “Electrochemical properties of vanadium oxide aerogels,” *Sci. Technol. Adv. Mater.*, vol. 4, no. 1, pp. 3–11, 2003.

- [55] C. M. Laot, E. Marand, and H. T. Oyama, "Spectroscopic characterization of molecular interdiffusion at a poly(vinyl pyrrolidone)/vinyl ester interface," *Polymer (Guildf)*, vol. 40, no. 5, pp. 1095–1108, 1999.
- [56] L. S. de Vasconcelos, R. Xu, J. Li, and K. Zhao, "Grid indentation analysis of mechanical properties of composite electrodes in Li-ion batteries," *Extrem. Mech. Lett.*, vol. 9, pp. 495–502, 2016.
- [57] Y. Wang and W. H. Zhong, "Development of electrolytes towards achieving safe and high-performance energy-storage devices: A review," *ChemElectroChem*, vol. 2, no. 1, pp. 22–36, 2015.
- [58] C. Ravindra, M. Sarswati, G. Sukanya, P. Shivalila, and Y. Soumya, "Tensile and Thermal Properties of Poly ( vinyl pyrrolidone )/ Vanillin Incorporated Poly ( vinyl alcohol ) Films," vol. 3, no. 8, pp. 1–6, 2015.

## CHAPTER FIVE

### 5.0. Conclusion, Contributions to Knowledge, Challenges and Recommendations for Future work.

#### 5.1. Conclusion

The need for flexible energy storage devices has stimulated the interest in the development of nanostructures in supercapacitors for energy storage. Carbon materials has revolutionized the design and development of energy storage systems. Furthermore, the integration of heteroatoms into a network of carbon materials has engineered new materials with exceptional features in terms of composition, morphologies and microstructures that are suitable as electrode for electrochemical capacitors. Also, Transition metal oxides (RuO<sub>2</sub>, MnO<sub>2</sub>, Co<sub>2</sub>O<sub>3</sub>, Co<sub>3</sub>O<sub>4</sub>, NiO, Fe<sub>3</sub>O<sub>4</sub>, TiO<sub>2</sub>, V<sub>2</sub>O<sub>5</sub>. Etc) can be grown on carbon cloth or activated carbon which is integrated as binder-free, symmetric/asymmetric devices, which can then be assembled and tested for electrochemical capabilities. These fabricated devices has potential applications in supercapacitors for energy storage systems that address global energy needs.

Also, electrolyte is a viable parts of energy storage systems. We have liquid electrolyte as well as solid electrolyte. The conventional LiBs use liquid electrolytes and plays major role in the market. However, there are significant fire and explosion risks that are associated with the chemical instability of liquid electrolytes e.g. due to the presence of carbonates that are highly volatile and flammable. Solid electrolytes (SEs) offer promising and viable alternatives that reduce the safety risks associated with the use of liquid electrolytes. Amongst all SEs, polymer based SEs are preferred because of their low flammability, good flexibility, excellent thermal stability, and high safety.

It is important to study the mechanical properties of solid state electrolyte to give an

understanding of the behavior of the blends to applied load. This work, explored the development of SE using a mixture of host polymers of PVP, PVA and lithium perchlorate ( $\text{LiClO}_4$ ) integrated into flexible and light-weight transparent films. The mechanical properties of the films are studied using nanoindentation techniques and statistical deconvolution mapping, tensile tests and fracture toughness measurements resulting to Young's modulus of 6.87 GPa, Hardness of 1.3 GPa, Tensile strength of 4.3 MPa and Fracture toughness of  $0.81 \text{ MPa}\cdot\text{m}^{0.5}$  which has potential applications of robust solid polymer blends-based electrolytes.

## 5.2. Contributions to Knowledge

The following outstanding points have been highlighted as the major contributions of this work to the existing body of knowledge:

- i. This work demonstrated that activation (functionalization) of the carbon cloth (CC) introduced functional groups to the CC.
- ii. The effects of the functional groups resulted to an excellent uniform and dispersed  $\alpha\text{-Fe}_2\text{O}_3$  nanoparticles on the activated carbon cloth
- iii. The work established that the activation resulted in electrodes with Specific Capacity of  $295.56 \text{ mAhg}^{-1}$  and excellent cyclic stability. These combinations of energy storage characteristics suggest that  $\alpha\text{-Fe}_2\text{O}_3$  nanoparticle-activated carbon cloths are promising structures for future applications in the electrodes of flexible supercapacitor structures.
- iv. The second work demonstrated the development of solid electrolyte (SE) using a mixture of host polymers of PVP, PVA and lithium perchlorate ( $\text{LiClO}_4$ ) integrated into flexible and light-weight transparent films.
- v. To the best of knowledge, there has been no prior work on the mechanical properties of PVA/PVP/ $\text{LiClO}_4$  polymer-based solid electrolytes (SEs) that are being considered for

potential applications as solid electrolyte. Thus, this work studied the mechanical properties of PVA/PVP/LiClO<sub>4</sub> polymer-based SEs using a combination of tensile, nanoindentation and fracture toughness measurements to determine the strength, Young's moduli, hardness, and fracture toughness values.

### 5.3. Challenges and Recommendations for Future work.

The results obtained from chapter three suggests that  $\alpha$ -Fe<sub>2</sub>O<sub>3</sub> processed on activated carbon cloth has potential for applications in flexible supercapacitors with good cycle lives at comparable capacities and specific currents to those of unactivated carbon cloth. Further work is needed to determine the mechanical properties of the layers and nanoparticle structures in the model structures that were examined in this study. This will require multi-scale mechanical property measurements of the adhesion, contact (nanoindentation) and deformation (elastic and plastic) behaviour under different loading conditions (bending, twisting and axial). There is also the need to explore the possible failure (fatigue and fracture) phenomena that can occur in flexible supercapacitors that are deformed under monotonic or cyclic loading conditions. These are clearly some of the challenges for future work.

For chapter four, the mechanical properties obtained from the study on PVA/PVP/ LiClO<sub>4</sub> blends are potential candidates for applications in solid state electrolytes. The trends in the measured Young's moduli and hardness values also imply that the control of the blend mixtures can be used to engineer the design of robust films with attractive combinations of strength, Young's moduli and fracture toughness. However, further work is needed to study the fatigue behaviour and ionic conductivities of the blends.